Computational models of optogenetic neurostimulation

Ruben Schoeters

Supervisors: Prof. dr. ir. Emmeric Tanghe, Prof. dr. Robrecht Raedt
Counsellor: Thomas Tarnaud

Master's dissertation submitted in order to obtain the academic degree of
Master of Science in Biomedical Engineering

Department of Information Technology
Chair: Prof. dr. ir. Bart Dhoedt

Animalarium,Vakgroep Inwendige ziekten
Chair: Prof. dr. Guy Joos

Faculty of Engineering and Architecture
Academic year 2017-2018

GHENT
UNIVERSITY

Computational models of optogenetic neurostimulation

Ruben Schoeters

Supervisors: Prof. dr. ir. Emmeric Tanghe, Prof. dr. Robrecht Raedt
Counsellor: Thomas Tarnaud

Master's dissertation submitted in order to obtain the academic degree of
Master of Science in Biomedical Engineering

Department of Information Technology
Chair: Prof. dr. ir. Bart Dhoedt

Animalarium,Vakgroep Inwendige ziekten
Chair: Prof. dr. Guy Joos

Faculty of Engineering and Architecture
Academic year 2017-2018

GHENT
UNIVERSITY

Acknowledgments

First, I would like to thank my counsellor, Thomas Tarnaud, for guiding me through the process of this master dissertation. He always took the time to answer my questions and discuss my results, in person and even via Skype. He came up with some important key insights and pushed me to improve my thinking.

Furthermore, I would like to thank my supervisors prof. dr. ir. Emmeric Tanghe and prof. dr. Robrecht Raedt, for making this thesis possible, proposing interesting research questions and giving me a lot of freedom to investigate my own interests. A special thanks goes to Wouter Van Lysebettens for sharing his data recordings and teaching me how to work with the Spike2 software.

Last but not least, I would like to thank my whole revision committee: my parents, my sister and my girlfriend, for their support, keen eye for typos and pedantry.

Ruben Schoeters, June 2018

Copyright Statement

Abstract

In this master dissertation, computational models for optogenetic stimulation were investigated. This will be centered around the most well-known opsin channelrhodopsin-2 (ChR2) of the *Chlamydomonas reinhardtii* Nagel et al. (2003). Initially, a comparative literature study was performed, where the goal was to find out how the opsin's kinetics are optimally modeled. This led to the advanced four state ChR2(H134R) model, derived by Williams et al. (2013), which was implemented in MatlabR2017a. Subsequently, an *in silico*, comparative analysis between electrical and optical stimulation in the subthalamic nucleus (STN) was performed, where three topics where investigated: the effect of a continuous pulse on the firing rate, the strength-duration relationship for the firing of an action potential within ten milliseconds and the effect on the action potential morphology. Finally, the initial steps were taken for the creation of a network independent locus coeruleus (LC) model. This model was fitted and validated against *in vivo* measurements on rat brains performed by the Laboratory for Clinical and Experimental Neurophysiology at the university of Ghent.

Keywords

Optogenetics, computational models, subthalamic nucleus, locus coeruleus

Computational models of optogenetic neurostimulation

Ruben Schoeters

Supervisors: Prof. dr. ir. Emmeric Tanghe, Prof. dr. Robrecht Raedt
Counsellor: Thomas Tarnaud

Abstract—**In this study, computational models of optogenetic neurostimulation were investigated. An advanced model derived by Williams et al. (2013), was implemented and adapted in MatlabR2017a. This model was then used to construct an extensive comparison between electrical and optical stimulation in the subthalamic nucleus. Also, a network independent LC model was created, starting from the model derived by Carter et al. (2012). This was done by fitting and validating the model against *in vivo* measurements on rat brains performed by the Laboratory for Clinical and Experimental Neurophysiology at the university of Ghent.**

Keywords— **Optogenetics, computational models, locus coeruleus, subthalamic nucleus**

I. Introduction

WITH optogenetics, optical control of the functioning of cells is possible. This is achieved by genetically expressing opsins, light sensitive ion channels, in cells or cell subtypes. The merger of this genetic expression and optical stimulation result in superior spatial and temporal resolution. Consequently, it is an ideal investigative tool for behavioral studies and shows a lot of potential as modulation tool for medical disorders such as epilepsy, Parkinson's disease and beyond the brain conditions (Diester et al., 2011[1], Gerits and Vanduffel, 2013 [2], Husser, 2014 [3], Jazayeri et al., 2012[4], Williams and Denison, 2013 [5], Williams et al., 2013 [6]).

In this study, computational models for optogenetic stimulation were investigated. This will be centered around the most well-known opsin channelrhodopsin-2 (ChR2) of the *Chlamydomonas reinhardtii* (Nagel et al., 2013 [7]). Initially, a comparative literature study was performed, where the goal was to find out how the opsin's kinetics are optimally modeled. This led to the advanced four state ChR2(H134R) model, derived by Williams et al. (2013) [6], which was implemented in MatlabR2017a. Subsequently, an *in silico*, comparative analysis between electrical and optical stimulation in the subthalamic nucleus (STN) was performed, where three topics where investigated: the effect of a continuous pulse on the firing rate, the strength-duration relationship for the firing of an action potential within ten milliseconds and the effect on the action potential morphology. Finally, the initial steps were taken for the creation of a network independent locus coeruleus (LC) model. This model was fitted and validated against *in vivo* measurements on rat brains performed by the Laboratory for Clinical and Experimental Neurophysiology at the university of Ghent.

First the ChR2 photocycle and the four state model derived by Williams et al. (2013) [6], together with the validation in MatlabR2017a will be discussed in section II. Secondly, the results of the comparative analysis in the STN are presented in section III. Finally, the initial results of the derived LC model and future work will be denoted in section IV.

II. Channelrhodopsin-2 Modeling

In this section, the ChR2 photocurrent and underlying photocycle is denoted first. Subsequently, the implementation of the four state ChR2(H134R) in MatlabR2017a and validation are discussed.

A. ChR2 photocycle

Under voltage clamp conditions and during continuous light stimulation, ChR2 exhibits a typical biphasic current course. Upon illumination, first a fast transient peak is observed, followed by a steady-state plateau caused by desensitization of the channel. Post-illumination, the current diminishes with a bi-exponential decay back to baseline due to closing of the channel. The opening is initiated by 13 trans-cis isomerization of retinal, triggered by the absorption of photons, which results in a cascade of conformational change of the seven transmembrane helices that form the ChR2 channel.

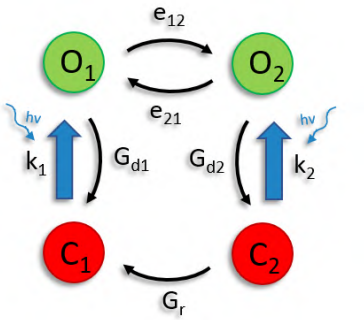

Fig. 1. Four state branching model of the ChR2 photocycle

To model the electrophysiological behavior, at least a three state model is required. Multiple models have been proposed. However, to account for both the fast off kinetics and multiple orders of magnitude higher recovery kinetics, a second light dependent step or a four state model, with two open and closed states, is needed. Due to the absence of prove for this second light dependent step, the bi-exponential post-illumination current decay and prove for an existing second photocycle, the four state branching model (depicted in figure 1) dominates the three state versions.

B. Four state ChR2(H134R) model

Williams et al. (2013) [6] derived an accurate four state model of the ChR2(H134R) mutant. Furthermore, their model incorporates both the light and voltage dependence of ChR2. The current-voltage relationship is strongly non-linear, with inward rectification. The specific transmembrane current (i_{ChR2}) is calculated as follows:

$$i_{ChR2} = g_{ChR2} G(V)(O_1 + \gamma O_2)(V - E_{ChR2}) \qquad (1)$$

with g_{ChR2} the maximal ChR2 conductance (S/m^2), G(V) the rectification function, γ the ratio of conductance and E_{ChR2} the reversal potential (mV).

To exploit this model for further analyses, the model was implemented in MatlabR2017a. As validation, the normalized error, with respect to the published results, were calculated. The current validation resulted in a negligible error of less than 3%. For the kinetics, however, high errors were obtained. To extract the time constants, mono-exponential curves were fitted to the individual current segments. This resulted in a less than 5% error in case of the inactivation time constant, 15.61±9.34% error for the off kinetics and a staggering 93.96±37.64% for the activation time constant. Although reported differently, by fitting a logistics curve instead of a mono-exponential to the rising current segment only a 10.9±7.34% error was obtained. The error for the recovery kinetics was only 2.2±1.5% by comparing the peak to peak ratios, while comparison of the time constant resulted in a 15.22±3.63% error. Giving, the negligible errors for the current validation and the questionable explanation of the used fitting methods, the model was assumed to be implemented correctly.

After this validation, the rectification function was changed to the one derived by Grossman et al. (2011) [8], as the current led to physically impossible conductances at the reversal potential and other alternatives, although not empirical, led to a significant increase of the model's complexity (Gradmann et al., 2011 [9]).

III. Electrical versus optical stimulation in the subthalamic nucleus

As part of the basal ganglia, the subthalamic nucleus plays a pivotal role in voluntary movement control. Therefore, it is the target for deep brain stimulation in case of Parkinson's disease, in order to alleviate the symptoms. However, there are some severe limitations acquainted with electrical stimulation, such as electrochemical reactions. Therefore, it is interesting to investigate the performance of optogenetics in comparison with electrical stimulation. This is executed for three topics: the effect of a continuous pulse on the firing rate, the strength-duration relationship for AP firing within ten milliseconds and the effect on the AP morphology. These are discussed in this section in chronological order.

A. Firing rate

The mean spike frequency (MSF), for both stimulation sources, calculated over the pulse duration is shown in figure 2. The dark blue area in the lower left corner indicates the absence of two subsequent spikes during the pulse. The maximum obtained frequencies are 95.47 Hz and 230.1 Hz, for a 10000 $\mathrm{W/m^2}$, 0.8 s optical and 1 $\mathrm{A/m^2}$, 10 ms electrical pulse, respectively. Furthermore, a MSF range match can be denoted between the complete optical stimulation set and electrical stimulations for amplitudes up to 0.1 $\mathrm{A/m^2}$.

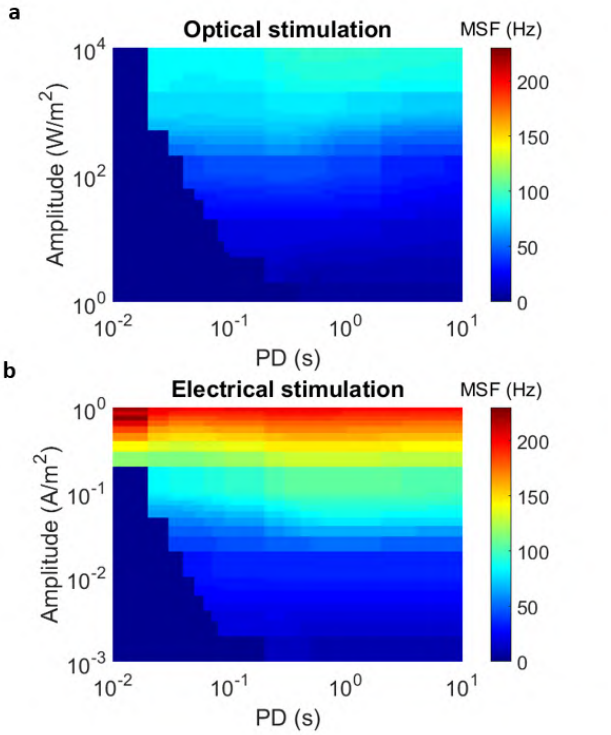

Fig. 2. Surface plot of the mean spike frequency. (a) optical stimulation. (b) electrical stimulation. Dark blue area in the lower left corner indicates the absence of two subsequent spikes during the pulse

Figure 4 depicts the mean instantaneous frequency with respect to the pulse amplitudes. For both sources, the firing rate rises first linearly with pulse amplitude (exponentially on logarithmic scale). However, in case of optical stimulation, the frequency saturates for pulses with amplitudes higher than 1000 $\mathrm{W/m^2}$. Overall, the standard deviation is rather low, indicative for regular spiking behavior. Furthermore, for increasing pulse duration, the frequency increases slightly and stays more or less constant for pulses higher than 300 ms in case of electrical stimulation, but decreases in case of optical stimulation. This can be seen in figure 3, where the instantaneous frequency is plotted.

The increase for pulses up to 300 ms, can be devoted to the strong increase of the depolarizing L-type calcium current. Hence, this due to the neuron physiology itself. The decrease can be explained by taking the ChR2 channel inactivation into account. For short pulse durations the transient peak dominates the steady-state current. Hence, a higher depolarizing current to pulse duration ratio is obtained for small pulses, which results in a higher relative firing rate. However, for longer pulses the steady-state current dominates the current to pulse duration ratio. Consequently, the frequency drops slightly. Furthermore, the inactivation is intensity dependent, with faster inactivation for higher intensities. This explains why the decrease

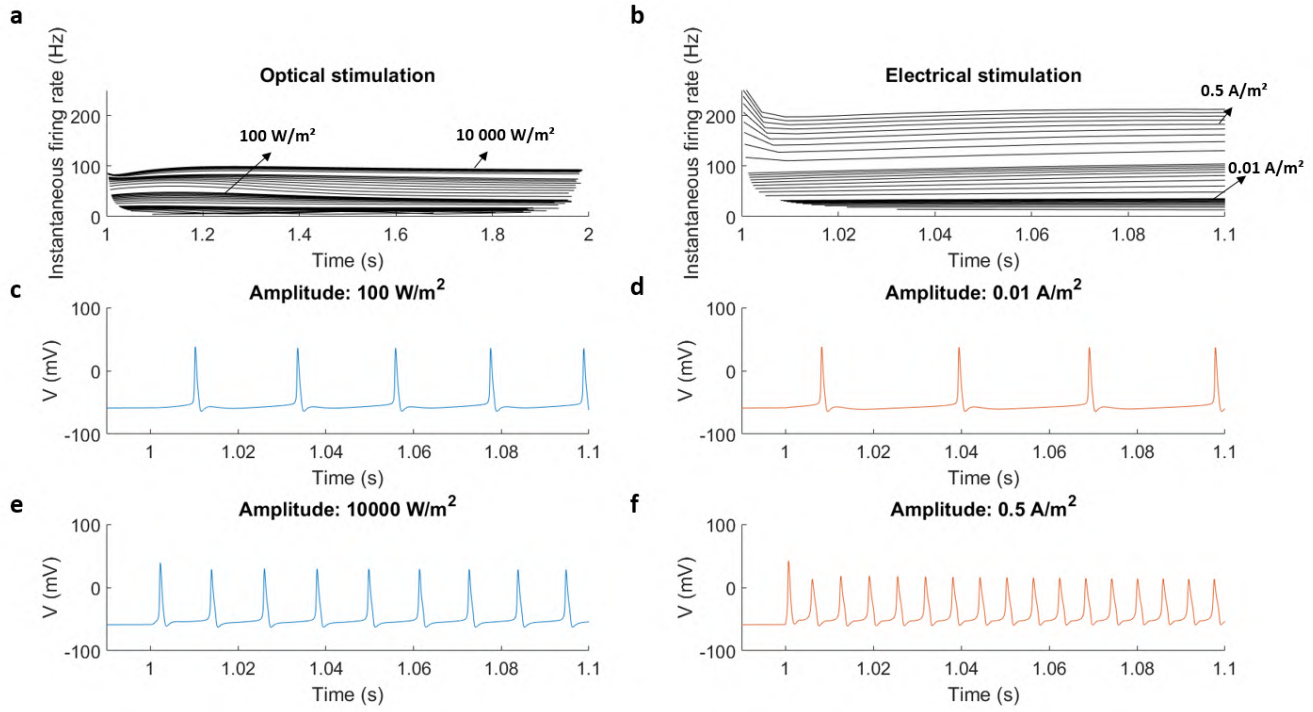

Fig. 3. The instantaneous firing rate during a 1 s pulse zoomed in on the first 100 ms. (a,b) the instantaneous firing rate for the whole amplitude set for optical and electrical stimulation, respectively. (c,e) the membrane potential for optical stimulation with amplitude 100 $\mathrm{W/m^2}$ and 10000 $\mathrm{W/m^2}$, respectively. (d,f) The membrane potential for electrical stimulation with amplitude 0.01 $\mathrm{A/m^2}$ and 0.5 $\mathrm{A/m^2}$, respectively

in frequency is more prominent for pulse amplitudes between 100 $\mathrm{W/m^2}$ and 1000 $\mathrm{W/m^2}$.

B. Strength-duration

An important feature is the delay between pulse onset and AP generation. As expected, the delay decreases with increasing pulse amplitude. Furthermore, for a fixed amplitude, the delay-PD curve levels off, when the pulse duration is longer than the latency of the action potential. Hence, no further improvement can be made by prolonging the pulse, as the AP already fired.

The strength-duration relationship was determined for a ten millisecond threshold. This gave rise to a visual rheobase of 103.48 $\mathrm{W/m^2}$ and 0.0073 $\mathrm{A/m^2}$ for optical and electrical stimulation respectively. Fitting of the Hill-Lapicque equation, for chronaxie extraction, led to an almost perfect fit ($R^2 = 0.9994$) for electrical stimulation, but poor fit in case of optical stimulation ($R^2 = 0.91$). The poor fit however, is inherent to the derivation of the Hill-Lapicque equation. By substituting the irradiance with the threshold, averaged stimulating current, i.e. the total transmembrane current prior and during the AP divided by the pulse duration, also an almost perfect fit ($R^2 = 0.9994$) was obtained (see figure 5). This enables the direct comparison of the charge needed to excite. The rheobase of optical stimulation is almost twice (175.21%) the electrical rheobase (0.0124 $\mathrm{A/m^2}$ vs. 0.0071 $\mathrm{A/m^2}$). Moreover, the chronaxie is higher as well (9.61%). Therefore, there exists no pulse duration for which both stimulation sources are equally efficient. Consequently, electrical stimulation turns out to be more efficient for all pulses. One of the underlying reasons of its inferiority, is the dynamic i_{ChR2} waveform. Whereas, the electrical rectangular pulse has an infinite rising rate, the light-triggered activation of ChR2 is a kinetic process with a time constant > 1 ms (in case of the H134R mutant) [10]. Consequently a greater optical pulse amplitude compared to electrical stimulation is required. The optical strength-duration curve, with the threshold, averaged stimulating current as strength, can be mapped back onto the original, with a three-term power series. Consequently, also an almost excellent fit ($R^2 = 0.9986$) was obtained. The resulting rheobase and chronaxie are 103.48 $\mathrm{W/m^2}$ and 3.164 ms, respectively.

C. Action potential morphology

Finally, the effect of the stimulation source on the AP waveform was studied. Here, an AP triggered by electrical and optical stimulation was compared. This was done by applying a non- and overlapping pulse for both stimulation sources. The compared AP morphologies were the ones triggered by a 1 ms pulse, with a 1177 $\mathrm{W/m^2}$ and 0.0402 $\mathrm{A/m^2}$ amplitude, and a 20 ms pulse, with both a 104 $\mathrm{W/m^2}$ and 1177 $\mathrm{W/m^2}$, and 0.0074 $\mathrm{A/m^2}$ and 0.0402 $\mathrm{A/m^2}$, amplitude, for optical and electrical stimulation, respectively. Unexpectedly, no significant differences were observed for the 1 ms pulse. Due to ChR2 slower of kinetics (∼20 ms), the channel remains open during the AP. However, the 1 ms pulse led only to a max depolarizing current of 1 $\mu\mathrm{A/cm^2}$, which is neglectable in comparison with the total transmembrane current of 400 $\mu\mathrm{A/cm^2}$. Furthermore, the voltage dependence of ChR2 decreases its modifying affect, as its current changes with the AP waveform. Only in case of

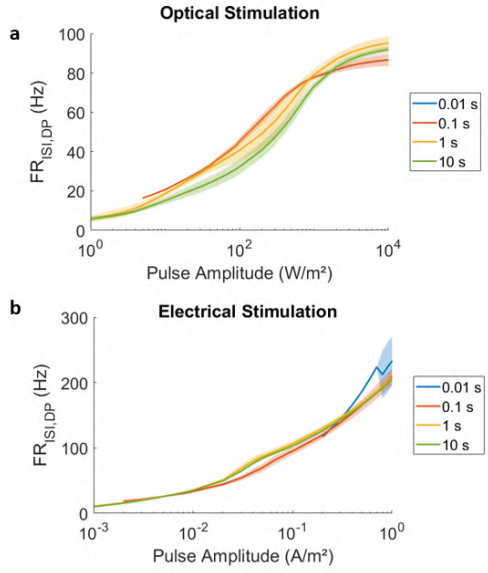

Fig. 4. Mean instantaneous frequency ± standard deviation (shaded area) with respect to pulse amplitudes, calculated over the pulse duration. (a) optical stimulation. (b) electrical stimulation

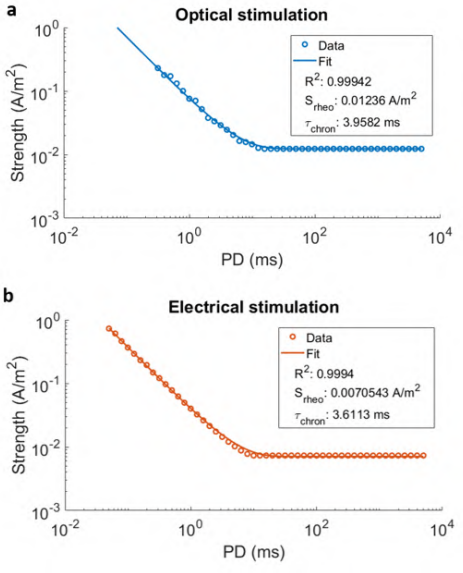

Fig. 5. The optical and electrical strength-duration curves for a threshold of 10 ms, with the threshold, average stimulating current as strength

the large amplitude 20 ms pulse, observable affects could be denoted, with a slightly less hyperpolarization in case of the optical source.

IV. Locus coeruleus

The locus coeruleus (LC), located in the pons, is one of the most dominant noradrenergic systems in the brain. Consequently, it has an important role in sleep to wake transition, attention and feeding behavior. Furthermore, studies have shown that the LC is correlated to the anticonvulsive action of vagus nerve stimulation. However, the underlying mechanism is not fully understood yet. Therefore, it would be interesting to develop an accurate model such that *in silico* investigations can be performed.

In this section the path, starting from the locus coeruleus model derived by Carter et al. (2012) [11], to a network independent model is denoted. First a two and single compartment model are fitted to the spontaneous firing rate of an LC. Secondly, the optical response is fitted and validated.

A. Comparison models

The LC models derived in this study, were adapted from the work of Carter et al. (2012) [11]. Their model consists of two electronically compact compartments, modeled according to the Rall-model, implemented in a network of multiple LC and hypocretin neurons. Starting from this model, an network independent model was derived, that accurately represents optogenetic responses. The network independence was achieved by replacing the inter neuron currents by a simple continuous depolarizing current.

The required constant depolarizing current was determined, such that the model's spontaneous firing rate matched the measured, *in vivo* 3.35±0.49 Hz. As it turned out, it was not possible to model this behavior with the original two compartment model and a simple depolarizing current. The maximum achievable MSF was only 0.75 Hz for a depolarizing current of $0.4\ \mathrm{A/m^2}$. For higher amplitudes, the model gave an initial small burst, followed by an infinite refractory period. However, by combining the two compartments into a single one, this was simply done by equalizing the potentials and summation of the two compartments, a tonic firing rate of 3.34 Hz could be achieved with an current amplitude of $0.39\ \mathrm{A/m^2}$

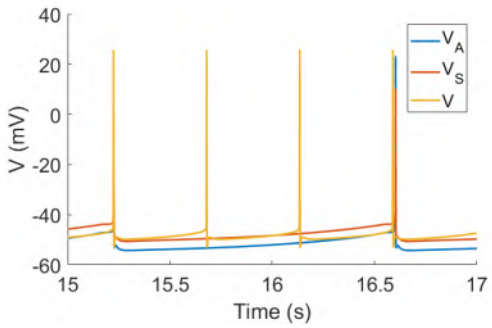

Fig. 6. Comparison of membrane potentials, with V_A, V_S and V the membrane potentials of the two compartment, axon and soma, and one compartment model, respectively, for a fixed depolarizing current of $0.3\ \mathrm{A/m^2}$. APs of the one compartment model are shifted to match the first AP generated by the two compartment model after 15 s

Figure 6 depicts the comparison of the action potentials generated by two models. Several interesting features could be extracted. First, there is a more or less constant difference between the soma and axon compartments, until the AP threshold is reached. Secondly, during and after an AP, the single compartment matches the soma compartment, while upon firing it matches the axon compartment. Furthermore, from the com-

parison of the transmembrane currents, no significant difference could be denoted that could explain the low firing rate achievable with the two compartment model. Hence, the behavior is solely due to the spatial filtering.

B. Pinch and optical response

To validate the fit, it was tested if the *in vivo* pinch response could be reproduced. This was possible with a $0.0314\ \mathrm{A/m^2}$, 0.90 s electrical pulse (the pulse duration is equal to the averaged pinch duration), which gave rise to a MSF and refractory period of 13.68 Hz and 1.09 s, respectively. With a t-test, these were found not to be significantly different (p = 0.98 and p = 0.54, respectively) form the measured values, i.e. 13.64±2.74 Hz and 1.19±0.23 s.

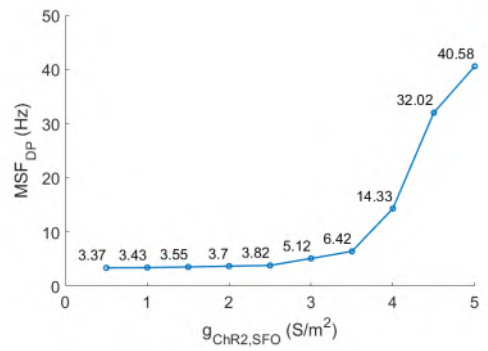

Fig. 7. The mean spike frequency with respect to the maximal conductances of ChR2 ($g_{ChR2,SFO}$)

For the *in vivo* measurements, the rats were transfected with a ChR2(L132C-T195C) mutant. The optical behavior was modeled with a, to the mutant's dynamics adjusted, two state ChR2(SFO) model. Next, the maximum ChR2 conductance was fitted. This fit was based on the measured response to a 1.49 s laser pulses. With a maximum conductance of $3\ \mathrm{S/m^2}$, a firing rate of 5.12 Hz can be modeled, which matches the measured value of 5.11±0.35 Hz. For validation, it was tested if the derived model could accurately represent the responses to a 0.5 s and 0.98 s pulse. The results are summarized in figure 8, with a not significantly different (p = 0.08) and significantly different MSF (p = 0.004) for the 0.5 s and 0.98 s pulse, respectively.

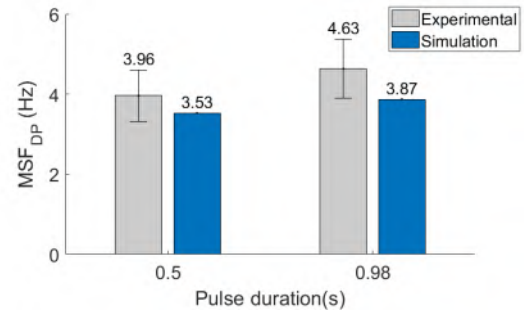

Fig. 8. Bar graph representing MSFs of measured and simulated optical responses, for a pulse duration of both 0.5 s and 0.98 s

C. Future work

In future work, the model will be further optimized. This will be done by fitting the model to a more extensive training data set consisting of multiple rat recordings, with as goal to decrease the current overfitting. Next a proper validation is required, where the model is tested versus unseen data. Furthermore, improved modeling of the fast transient inter neuron currents will be investigated. One of the possibilities is to couple the axons output back to its own soma, superimposed with a certain delay. Another solution exists in the modification of the models rate functions. Finally, the advanced four state ChR2 model will be modified to match the dynamics of the used *in vivo* mutant in order to assess the need for such a complex model.

V. Conclusion

Computational models of optogenetic neurostimulation were investigated. To accurately model the ChR2's dynamics, a branched four state transition model is required. An advanced model derived by Williams et al. (2013), was implemented and adapted in MatlabR2017a. This model was then used to construct an extensive comparison between electrical and optical stimulation in the subthalamic nucleus. From these *in silico* experiments, the electrical stimulation seems to be superior. Furthermore, the initial steps were taken in the creation of a network independent LC model, starting from the model derived by Carter et al. (2012). However, some fine tuning is still necessary.

References

[1] Ilka Diester, Matthew T Kaufmann, Murtaza Mogri, and Et al, "An optogenetic toolbox designed for primates," *Nature*, p. 22, 2011.

[2] Annelies Gerits and Wim Vanduffel, "Optogenetics in primates: A shining future?," *Trends in Genetics*, vol. 29, no. 7, pp. 403–411, 2013.

[3] Michael Häusser, "Optogenetics: The age of light," *Nature Methods*, vol. 11, no. 10, pp. 1012–1014, 2014.

[4] Mehrdad Jazayeri, Zachary Lindbloom-Brown, and Gregory D Horwitz, "Saccadic eye movements evoked by optogenetic activation of primate V1," p. 10, 2012.

[5] Justin C. Williams and Timothy Denison, "From optogenetic technologies to neuromodulation therapies," *Science Translational Medicine*, vol. 5, no. 177, pp. 1–5, 2013.

[6] John C. Williams, Jianjin Xu, Zhongju Lu, Aleksandra Klimas, Xuxin Chen, Christina M. Ambrosi, Ira S. Cohen, and Emilia Entcheva, "Computational Optogenetics: Empirically-Derived Voltage- and Light-Sensitive Channelrhodopsin-2 Model," *PLoS Computational Biology*, vol. 9, no. 9, pp. 17–19, 2013.

[7] G. Nagel, T. Szellas, W. Huhn, S. Kateriya, N. Adeishvili, P. Berthold, D. Ollig, P. Hegemann, and E. Bamberg, "Channelrhodopsin-2, a directly light-gated cation-selective membrane channel," *Proceedings of the National Academy of Sciences*, vol. 100, no. 24, pp. 13940–13945, 2003.

[8] Nir Grossman, Konstantin Nikolic, Christofer Toumazou, and Patrick Degenaar, "Modeling study of the light stimulation of a neuron cell with channelrhodopsin-2 mutants," *IEEE Transactions on Biomedical Engineering*, vol. 58, no. 6, pp. 1742–1751, 2011.

[9] Dietrich Gradmann, André Berndt, Franziska Schneider, and Peter Hegemann, "Rectification of the channelrhodopsin early conductance," *Biophysical Journal*, vol. 101, no. 5, pp. 1057–1068, 2011.

[10] John C. Williams and Emilia Entcheva, "Optogenetic versus electrical stimulation of human cardiomyocytes: Modeling insights," *Biophysical Journal*, vol. 108, no. 8, pp. 1934–1945, 2015.

[11] M. E. Carter, J. Brill, P. Bonnavion, J. R. Huguenard, R. Huerta, and L. de Lecea, "Mechanism for Hypocretin-mediated sleep-to-wake transitions," *Proceedings of the National Academy of Sciences*, vol. 109, no. 39, pp. E2635–E2644, 2012.

Table of Contents

List of Figures

Figure **Page**

List of Tables

List of Abbreviations

AAV	Adeno-associated virus
AED	Anti-epileptic drugs
AMPA	$\alpha - \text{amino} - 3 - \text{hydroxy} - 5 - \text{methyl} - 4 - \text{isoxazolepropionicacid}$
AP	Action potential
Arch	Archaerhodopsin of *Halorubrum sosomense*
C, C_1, C_2	Closed state
C1C2	Chimera channelrhodopsin-1 and channelrhodpsin-2 *Chlamydomonas reinhardtii*
C1V1	Chimera channelrhodopsin-1 *Chlamydomonas reinhardtii* and channelrhodpsin-1 *Volvox carteri*
Ca, Ca^{2+}	Calcium ion
ChEF, ChIEF	Chimeric ultrafast opsins
ChETA	Ultrafast opsins, where Ci glutamate residue is substituted for threonine or alanine
ChR, ChR1, ChR2	Channelrhodopsin of *Chlamydomonas reinhardtii*
Ci	Counter ion
Cl, Cl^-	Chloride ion
CnChR1	Channelrhodopsin of *Chlamydomonas noctigama*
COP	Chlamyopsin
D	Desensitized state
DBS	Deep brain stimulation
FR_{ISI}	Mean instantaneous frequency
GHK	Goldman-Hodgkin-Katz
H^+	Proton
Hcrt	hypocretin
ISI	Inter-spike interval
K, K^+	Potassium ion

LC	Locus coeruleus
LCEN3	Laboratory for Clinical and Experimental Neurophysiology at Ghent university
LED	Light emitting diode
L-DOPA	Levodopa
MChR	Channelrhodopsin of *Mesostigma viride*
MSF	Mean spike frequency
Na, Na^+	Sodium ion
NpHR	Halorhodopsin of the arcaon *Natronomonas pharaonis*
O, O_1, O_2	Open state
OptoXR	Chimeric G-protein-coupled receptors
PD	Pulse duration
R^2	The coefficient of determination
RSB	Retinal Schiff base
$RSBH^+$	Protonated retinal Schiff base
SD	Strength-duration
SFO	Step-function opsin
ShChR	Channelrhodopsin of *Stigeoclonium helveticum*
SNc	Substantia nigra pars compacta
STN	Subthalamic nucleus
UV	Ultra violet
VChR	Channelrhodopsin of *Volvox carteri*
Vis	Visible spectrum
VNS	Vagus nerve stimulation

List of Symbols

Greek letters

$\boldsymbol{\alpha_n, \alpha_w}$	Opening rate (1/s)
$\boldsymbol{\beta_n, \beta_w}$	Closing rate (1/s)
$\boldsymbol{\gamma}$	Ratio of high and low conductance states (O_2/O_1)
$\boldsymbol{\epsilon_1, \epsilon_2}$	Quantum efficiency for photon absorption
$\boldsymbol{\Theta}$	Optical stimulation protocol $\Theta = 100\,\mathrm{I}$
$\boldsymbol{\lambda}$	Length constant
$\boldsymbol{\lambda}$	Wavelength of maximal absorption for retinal (m)
$\boldsymbol{\mu^2}$	Inverse calcium decay time constant (1/s)
$\boldsymbol{\sigma_{ret}}$	Absorption cross-section for retinal (m^2)
$\boldsymbol{\tau}$	Time constant (s)
$\boldsymbol{\tau_{ChR2}}$	Time constant of ChR2 activation (s)
$\boldsymbol{\tau_{chron}}$	Chronaxie (s)
$\boldsymbol{\tau_{inact}}$	Inactivation time constant (s)
$\boldsymbol{\tau_{on}}$	Activation time constant (s)
$\boldsymbol{\tau_{off}}$	Deactivation time constant (s)
$\boldsymbol{\tau_r}$	Recovery time constant (s)
$\boldsymbol{\tau_w}$	Gating variable time constant (s)

Latin letters

$\mathbf{A}$	Surface area (m^2)
$[\mathbf{A_j^-}]$	Concentration anion (μM)
$\mathbf{C_m}$	Membrane capacitance (F)
$\mathbf{c_m, c_A, c_S}$	Specific capacitance (membrane, Axon, Soma in F/m^2)
$\mathbf{d}$	Specific depth (m)
$\mathbf{E_{ChR2}}$	ChR2 reversal potential (mV)
$\mathbf{E_{Na^+}, E_{K^+}, E_{Ca^{2+}}}$ $\mathbf{E_{Na}, E_K, E_{Ca}, ...}$	Ion specific Nernst potential (mV)

$\mathbf{E_m}, \mathbf{E_l}$	Membrane equilibrium potential (mV)
$\mathbf{e_1}, \mathbf{e_2}$	ChR2 light dependent equilibrium, transition rates (1/s)
$\mathbf{F}$	Faraday's constant (C/mol)
$\mathbf{G_{ion}}$	Ion conductance (S)
$\mathbf{G_{d1}}, \mathbf{G_{d2}}, \mathbf{G_r}$	ChR2 deactivation transition rates (1/s)
$\mathbf{G(V)}$	Rectification function
$\mathbf{g_A}, \mathbf{g_{Ca-K}}, \mathbf{g_h}$	Potassium type channel specific membrane conductance (S/m^2)
$\mathbf{g_{AS}}, \mathbf{g_{SA}}$	Axon and soma connecting specific conductance (S/m^2)
$\mathbf{g_{Ca}}, \mathbf{g_L}, \mathbf{g_T}$	Calcium type channel specific membrane conductance (S/m^2)
$\mathbf{g_{ChR2}}$ $\mathbf{g_{ChR2,SFO}}$	ChR2 specific membrane conductance (S/m^2)
$\mathbf{g_l}, \mathbf{g_{l,A}}, \mathbf{g_{l,S}}$	Leakage channel specific membrane conductance (S/m^2)
$\mathbf{g_m}$	Specific membrance conductance (S/m^2)
$\mathbf{g_{Na+}}, \mathbf{g_{K+}}, \mathbf{g_{Ca^{2+}}}$ $\mathbf{g_{Na}}, \mathbf{g_K}, \mathbf{g_{Ca}}, \mathbf{\cdots}$	Ion channel specific membrane conductance (S/m^2)
$\mathbf{hc}$	Product of Planck's constant and the speed of light ($kg\,m^3/s^2$)
$\mathbf{I}$	Light intensity (W/m^2)
$\mathbf{I_p}, \mathbf{I_{p1}}, \mathbf{I_{p2}}$	Peak current (pA/pF)
$\mathbf{I_{SS}}$	Steady-state current (pA/pF)
$\mathbf{I_{th,avg}}$	Threshold average stimulating current
$\mathbf{i_A}, \mathbf{i_{Ca-K}}, \mathbf{i_h}$	Potassium type channel specific current (A/m^2)
$\mathbf{i_{AS}}, \mathbf{i_{SA}}$	Axon and soma connecting specific current (A/m^2)
$\mathbf{i_{Ca}}, \mathbf{i_L}, \mathbf{i_T}$	Calcium type channel specific current (A/m^2)
$\mathbf{i_{ChR2}}$ $\mathbf{i_{ChR2,SFO}}$	ChR2 specific current (A/m^2)
$\mathbf{i_l}, \mathbf{i_{l,A}}, \mathbf{i_{l,S}}$	Leakage channel specific current (A/m^2)
$\mathbf{i_m}$	Specific transmembrane current (A/m^2)
$\mathbf{i_{Na+}}, \mathbf{i_{K+}}, \mathbf{i_{Ca^{2+}}}$ $\mathbf{i_{Na}}, \mathbf{i_K}, \mathbf{i_{Ca}}, \mathbf{\cdots}$	Ion channel specific current (A/m^2)
$\mathbf{k_1}, \mathbf{k_2}$	ChR2 light dependent activation, transition rates (1/s)
$[\mathbf{M_i^+}]$	Concentration anion (μM)
$\mathbf{R}$	The universal gas constant (J/(K mol))
$\mathbf{P_X}, \mathbf{P_{A_j^-}}, \mathbf{P_{M_j^-}}$	Permeability of ion
$\mathbf{R_{axial}}$	Axial resistance (Ω)
$\mathbf{R_m}$	Membrane resistance (Ω)
$\mathbf{S_{Rheo}}$	Rheobase strength
$\mathbf{S_{th}}$	Threshold strength

$\mathbf{T}$	Temperature (K)
$\mathbf{V, V_m, V_A, V_S}$	Membrane potential (mV)
$\mathbf{V_{m0}}$	Resting membrane potential (mV)
$\mathbf{w_{loss}}$	Scaling factor for losses of photons due to scattering or absorption
$\mathbf{w_\infty}$	Gate variable steady-state function
$\mathbf{[X]_i, [X]_{in}}$	Intracellular concentration ion X (μM)
$\mathbf{[X]_o, [X]_{out}}$	Extracellular concentration ion X (μM)
$\mathbf{z, z_X}$	Valence of ion

Introduction

Optogenetics is one of last decade's most revolutionizing techniques in the field of neuroscience. It has made optical control of the functioning of cells possible, by genetically expressing opsins in cells or cell subtypes. The merger of this genetic expression and optical stimulation has given it superior characteristics, concerning spatial and temporal resolution. Consequently, it is an ideal investigative tool for behavioral studies and shows a lot of potential as modulation tool for medical disorders such as epilepsy, Parkinson's disease and beyond the brain conditions (Diester et al., 2011, Gerits and Vanduffel, 2013, Häusser, 2014, Jazayeri et al., 2012, Williams and Denison, 2013, Williams et al., 2013).

In this master dissertation, computational models for optogenetic stimulation are investigated. This will be centered around the most well-known opsin channelrhodopsin-2 of the *Chlamydomonas reinhardtii* (Nagel et al., 2003). Initially, a comparative literature study is performed where the goal is to find out how the opsin's kinetics are optimally modeled. Next, the accurate four state ChR2(H134R) model, derived by Williams et al. (2013), is implemented in MatlabR2017a. This model is used to perform an *in silico*, comparative analysis between electrical and optical stimulation in the subthalamic nucleus. Finally, the initial steps are taken for the creation of an accurate locus coeruleus model.

In the first chapter, the exploration of an optogenetic toolbox's core components is performed. Currently, there exists already a platelet of opsin possibilities. There are the natural microbial and vertebrate opsins, and bioengineered opsins for improved characteristics. Examples are the red-shifted, step-function, ultrafast opsins and opsins with increased ion selectivity. Also, multiple delivery methods and illumination techniques exist and are continuously improving. The chapter is concluded with advancements in terms of clinical applications and the expected hurdles that need to be conquered.

Prior to the ChR2 modeling, the electrophysiology of a cell is studied. A cell is surrounded by a phospholipid bilayer, making it impermeable to ions. Movement of ions across the membrane is permitted by ion channels and transporters, resulting in transmembrane currents. Consequently, a cell can be modeled by an electric equivalent circuit. For the generation of action potentials, voltage gated ion channels are required. These are typically modeled with a particle

gating scheme, first developed by Hodgkin and Huxley (Hodgkin and Huxley, 1990). These cell modeling principles are summarized in chapter 2, which forms the foundation of the advanced models used throughout this thesis.

In chapter 3, the dynamics of ChR2 are unraveled. Here the actual comparative study of computational models for optogenetic stimulation is performed. Under continuous stimulation, the channelrhodopsin-2 photocurrent depicts a biphasic course, with first a transient peak, followed by a steady-state current. Consequently, at least a three state model is required. Currently, there are two variants, which accurately model the ChR2 dynamics, i.e. a three transition state model with a second light dependent step or a four state model with two open en closed states. A top notch model of the latter, derived by Williams et al. (2013), is implemented in MatlabR2017a, validated and discussed.

This model is then used to perform a comparative analysis between electrical and optical stimulation in the subthalamic nucleus. This is a region of interest for deep brain stimulation, to alleviate symptoms correlated with Parkinson's disease. However, there are some severe limitations acquainted with electrical stimulation. In chapter 4, the aforementioned comparative analysis is performed. Three topics are investigated: the effect of a continuous pulse on the firing rate, the strength-duration relationship for firing of an action potential within ten milliseconds and the effect on the action potential morphology.

In the final chapter, a proof of concept is shown for the development of an accurate locus coeruleus model. As start point, the model derived by Carter et al. (2012) is used. This is adapted to an accurate, network independent model, fitted on experimental data received from the Laboratory for Clinical and Experimental Neurophysiology at the university of Ghent.

Chapter 1

Optogenetics

Neuroscience has taken a giant leap forward over the last decades. Classical biochemical and electrophysiological techniques have given a lot of new insights into the neural circuitry. Clinical advancements were made, resulting in a better understanding of disease pathologies and development of new therapies. Well known examples are cochlear implants, visual prostheses and deep brain stimulation (DBS), which is used for treating Parkinson's disease, epilepsy, chronic pain etc. (Aravanis et al., 2007, Boinagrov et al., 2010). However, a lot of questions still remain unanswered. This is due to the low temporal resolution of biochemical techniques on the one hand and the lack of cell specificity of electrophysiological techniques on the other. Where those techniques fail, optogenetics, which combines the high temporal resolution of optical stimulation with a high cell specificity, via genetically cell modification, may bring the solution (Cavanaugh et al., 2012, Diester et al., 2011).

In the following chapter the optogenetic technology will be discussed. First denoted is the discovery followed by a summary of the three crucial components, i.e. gene expression, opsins and illumination, used in an optogenetic toolbox and their popular available options. This chapter is concluded with some applications and hurdles for clinical translation.

1.1 The optogenetic toolbox

Although optogenetics globally refers to the optical control of the functioning of genetically modified cells (Mohanty et al., 2015), it is typically associated with genetic expression of opsins, light sensitive ion channels or pumps, in (neuronal) cells or cell subtypes in order to control their functioning with light. The most well-known opsin is channelrhodopsin-2 (ChR2), which is important for phototaxis and photophobic responses in the green algae *Chlamydomonas reinhardtii* (Abilez et al., 2011, Hegemann et al., 1991, Nagel et al., 2003). The idea of using light as a neuromodulation tool (Francis Crick, 1979) as well as the discovery of the first opsins originates in the 70's. The first opsin was discovered by Oesterhelt and Stoeckenius (1971), i.e. bacteriorhodopsin: an excitatory proton pump. Followed by halorhodopsin, an inhibitory chloride pump, by Matsuno-Yagi and Mukohata (1977). It took 25 years before channelrhodopsin, the first light-gated ion channel, was reported (Nagel et al., 2002), but has since revolutionized neuroscience (Claudia Pama et al., 2013, Wong et al., 2012, Yizhar et al., 2011).

In order for the optogenetic toolbox to work properly, three ingredients are necessary. First the optimal opsin needs to be selected. Selection criteria are ion selectivity, kinetics, spectral band and conductance. Next, a delivery method is required. Typically viral vectors such adeno associated or lenti virus are adopted. Finally a light source, a LED or laser, is obligated to activate the genetically modified cells. (Claudia Pama et al., 2013)

1.1.1 Opsins

Since the discovery of ChR2, the amount of different possibilities has increased dramatically. This is due to the discovery of new natural opsins as well as, and mostly, due to genetically engineering of the existing ones. This offers a platelet of possibilities with high variety in conductances, kinetics, spectral bands and selectivities (Guru et al., 2015).

The available opsins can be divided into two large groups. There are the microbial opsins (type I), such as ChR and VChR, and the vertebrate opsins (type II), such as OptoXR. The latter are G-protein coupled receptors. Accordingly activation results in a cascade of neural activity with slower responses as a consequence. Therefore, these types are mainly used in optogenetics for biochemical control. Consequently, most effort is put into the use of type I opsins for neural control (Gerits and Vanduffel, 2013, Guru et al., 2015, Yizhar et al., 2011) and will thus be further revised in this dissertation.

Natural opsins

As already denoted, the first light sensitive ion channel was discovered in the green alga *Chlamydomonas reinhardtii*. However, ChR2 is only one of the seven opsin-related genes of the alga. Of

these genes, Chlamyopsins (COP) 3 and 4 encode light-gated ion channels, respectively ChR1 and ChR2 (Stehfest and Hegemann, 2010). Both these channels comprise seven transmembrane helices combined with all-trans retinal chromophore. Upon light illumination, retinal undergoes a 13 trans-to-cis isomerization, which activates a cascade of conformational changes resulting in the opening of the channel pore (Schneider et al., 2015). Although there exist a 65% sequence homology between ChR1 and ChR2, there are significant differences concerning kinetics, action spectra and conductance. Research has shown that ChR1 is highly selective for protons (H^+), while almost impermeable for other cations resulting in a lower conductance than its counterpart, ChR2, which is permeable for most cations. On the other hand ChR2 limits fast pacing due to its rapid inactivation, whereas this is reduced in ChR1. At last, the peak activation wavelength is more red shifted for ChR1 (500 nm) in comparison with ChR2 (460 nm). Due to the red shift and faster kinetics, ChR1 could be more interesting for certain clinical applications than ChR2, though its low conductance renders it insufficient for neuronal depolarization (Lin et al., 2009, Nagel et al., 2002, 2003).

Next to ChRs of the alga *Chlamydomonas reinhardtii*, homologous were found in other chlorophycean algea, such as *Volvox carteri* (VChR), *Mesostigma viride* (MChR), *Stigeoclonium helveticum* (ShChr), *Chlamydomonas noctigama* (CnChR1) and up to 60 more (Schneider et al., 2015). Combination of the final two, for the activation of two distinct neural populations with different colors of light, has been proven to be possible. Multiple trials have been conducted to achieve this feature. This by creating red shifted mutants of ChR2 and decreasing blue light sensitivity or increased sensitivity of the counterpart, with the intention that low intensity blue stimulation would drive spiking in neurons with the blue light version and subthreshold spiking in neurons with the red shifted mutant. However, altering the blue light sensitivity of ChR2 has led to a decrease of the opsin's temporal resolution. Nevertheless, the combination of these properties is exactly what enables multi-population stimulation with Chronos and Chrimson. Irradiance with red light (625 nm) causes only spike activity in cells containing Chrimson (spectral peak at 590 nm), up to 10 Hz, whereas irradiance with blue light (470 nm) and power between 0.05 mW/mm^2 and 0.5 mW/mm^2 causes spike activity up to 60 Hz in Chronos (spectral peak at 500 nm) containing cells (Klapoetke et al., 2014).

Bioengineered opsins

To optimize the properties of the opsins, a lot of work was already put into genetic engineering of the existing opsins. Different paths that have been followed were point mutations and codon optimization. There have been attempts as well to combine the complementary properties of ChR1 and ChR2 leading to chimeric structures (Gerits and Vanduffel, 2013). It was the crystal structure of the C1C2 chimera that led to a breakthrough in protein engineering of ChR2. Although it is the chimeric crystal structure and not the one of ChR2, a lot of parallels between C1C2 and ChR2 can be drawn (see figure 1.1)(Ardevol and Hummer, 2018).

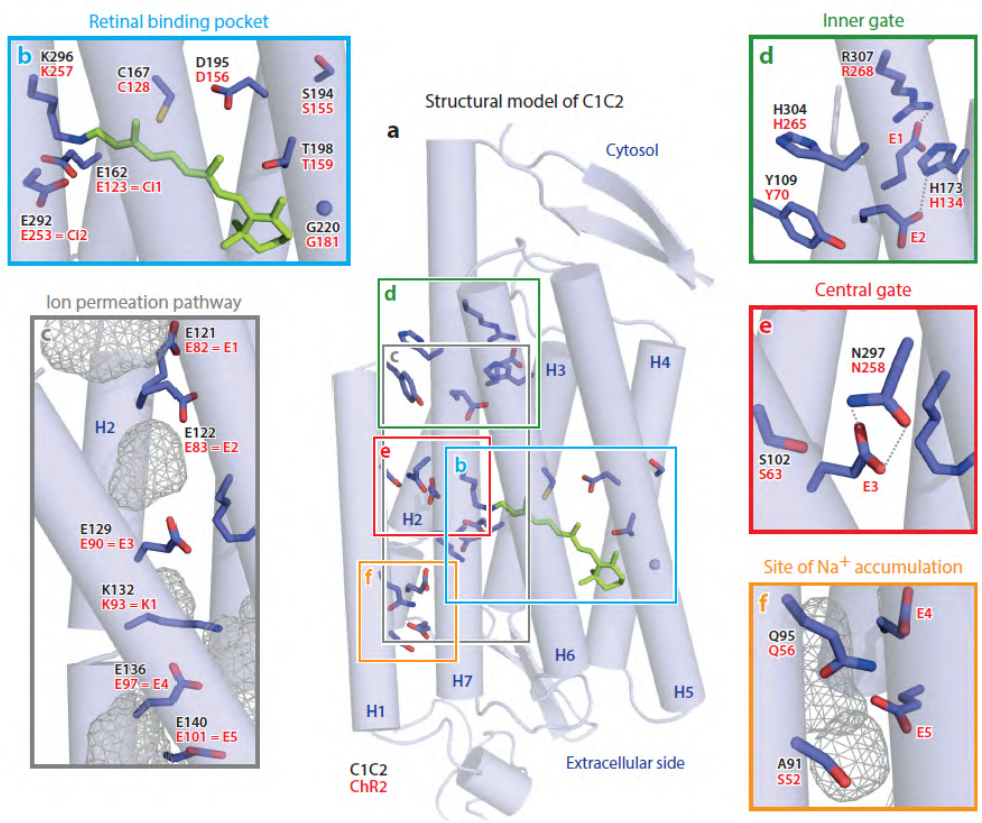

Figure 1.1: Structural model of C1C2 based on the crystal structure solved by Kato et al. (2012). The model reflects the closed dark adapted conformation. Helices H1-H5 originate from ChR1 while H6 and H7 originate from ChR2. (a) the overall protein structure with framed regions of interest. Retinal is the green structure enlarged in (b) which depicts the retinal binding pocket. (c) the ion permeation pathway. (d) the inner gate. (e) central gate and (f) site of Na^+ accumulations. The gray wireframes depict cavities within the protein in which water molecules and cations may reside. Adapted from Schneider et al. (2015)

Red-shifted opsins The need for red-shifted opsins emerged from the need to improve light penetration, necessary when translating the optogenetic toolbox from small animal models to non-human and human primates with larger brain volumes. Red light is subjected to less scattering and less absorption, hence resulting in deeper penetration and less heating. Besides, it creates the possibility to multi-population stimulation (Gerits and Vanduffel, 2013). Two driving factors are the retinal conformation and the interaction of the retinal Schiff base ($RSBH^+$), due to the covalent bonding between retinal and the K257 lysine residue (see Figure 1.1), and its counter ions (E123 or Ci1 and E253 or Ci2). Examples of mutations leading to bathochromic shift are E123Q and D253N for ChR2. Moreover, mutation of Ci1 in C1V1 (E162T) leads to a hypsochromic shift (Schneider et al., 2015).

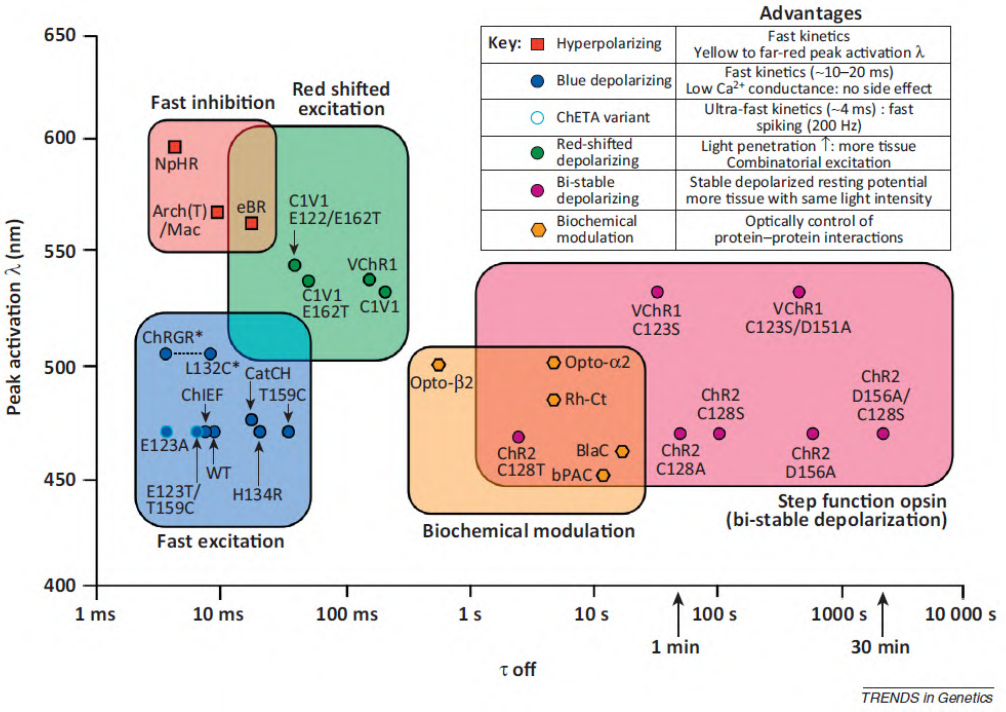

Figure 1.2: Overview of available opsins with their activation peak wavelength, decay kinetics and advantages. Adapted from Gerits and Vanduffel (2013)

Step-function opsins The advantage of step-function opsins (SFOs) is their bistable step-like control. These opsins are ideal for altering the spontaneous firing rate, but aren't suitable for single action potential (AP) control. The most popular SFO is the ChR2(C128S) mutant. The C128 residue forms together with D156 the DC-gate (see Figure 1.1). A mutation results in an extreme decrease of the kinetics and extends the lifetime of the channel open state. Moreover, a mutation of the whole DC-gate (C128S/D156A) results in a stabilized SFO with a deactivation time of almost thirty minutes (Guru et al., 2015, Schneider et al., 2015).

Ultrafast opsins Another class are the ultrafast opsins. These opsins contain faster kinetics, especially the off kinetics. This makes single spike control possible, whereas multiple spikes per stimulus are obtained for other opsins. Also, due to the fast recovery, higher stimulation frequencies for a prolonged stimulation can be used without loss of AP firing. A subclass of ultrafast opsins are termed ChETAs. Here the Ci1 glutamate (E) residue is substituted for a threonine (T) or alanine (A), resulting in an acceleration of the off kinetics from $\tau_{off} = 10\,ms$ to $\tau_{off} = 4\,ms$. However, the downside is the reduced light sensitivity (Gerits and Vanduffel, 2013, Guru et al., 2015, Pan et al., 2014, Prigge et al., 2012, Schneider et al., 2015). There exist chimeric ultrafast opsins as well. Examples are ChEF, a chimera with a crossover site at loop E-F (this is C1C2 in figure 1.1), and ChIEF, where isoleucine 170 in ChEF is mutated into valine. Whereas ChiEF contains faster kinetics the light sensitivity is reduced, however

still within the range of ($\sim 10\,\mathrm{mW/mm^2}$). With the latter high-fidelity stimulation of 25 Hz, up to 50 Hz, can be reached (depending of course on cell type and neural plasticity), while it is difficult to achieve a precise stimulation above 15 Hz with ChR2 (Lin et al., 2009).

Ion selectivity Another characteristic that has been modified is the ion selectivity. Almost all natural opsins have a superior selectivity for protons in comparison with ions. Even for ChR2 the relative proton conductance has been estimated to be $10^5 - 10^6$ times higher than for sodium ions. This brings the possibility of acidification of the host cell. The mutant ChR2(L132C-T159C) shows increased sodium conductance, calcium selectivity and enlarged magnesium conductance (Schneider et al., 2015). Furthermore, this mutation has an increased light sensitivity, at the cost of lower temporal kinetics, of 1.5 to 2 log units (Pan et al., 2014). Also a mutation of H134, which is part of the inner gate and sodium binding site, results in a Na^+ carried current. A well known and frequently used example is ChR2(H134R)(Schneider et al., 2015, Yizhar et al., 2011).

Inhibitory opsins

Next to the excitatory opsins, also inhibitory opsins exist. The yellow light activated chloride pump halorhodopsin (NpHR) of the arcaon *Natronomonas pharaonis*, is one of the most widely used and efficient opsins. Another inhibitory opsin is the archaerhodopsin-3 (Arch) from the *Halorubrum sodomense*, i.e. a proton pump that pumps protons out of the cell. As in case of the excitatory opsins, also for the inhibitory ones, trials have been conducted to genetically alter their properties, such as spectral shift, e.g., eNpHR3.0. Moreover, some effort is put into the creation of genetically engineered chloride channels. However, these maintain still some cation conductance. Nevertheless, recently two natural light gated anion channels have been discovered in the genome of *Guillardia theta*, i.e. GtACR1 and GtACR2 (Govorunova et al., 2015). A small summary of very popular opsins, both excitatory and inhibitory, is given in figure 1.2.

1.1.2 Gene expression

The second step is the introduction of the opsin's genetic material inside the target cells. The most popular method is the use of viral vectors. A viral vector construct contains four major building blocks (see figure 1.3). The first block is of course the viral expression system itself. The most common used systems are lentivirus and adeno-associated virus (AAV). The lentivirus has a larger packaging capacity (8 kb) with respect to AAV (4 kb), but incorporates into the host's genome. Although this causes permanent expression, it also increase the carcinogenic risk. The packaging capacity limits the promoter possibilities and thus reduces the diversity of specific targeted cells. However, AAV can be more effective due to its lower temperature sensitivity, further spreading, thanks to its smaller size and higher titers, and lower immunogenicity (Gerits and Vanduffel, 2013, Guru et al., 2015, Mohanty et al., 2015, Yizhar et al., 2011).

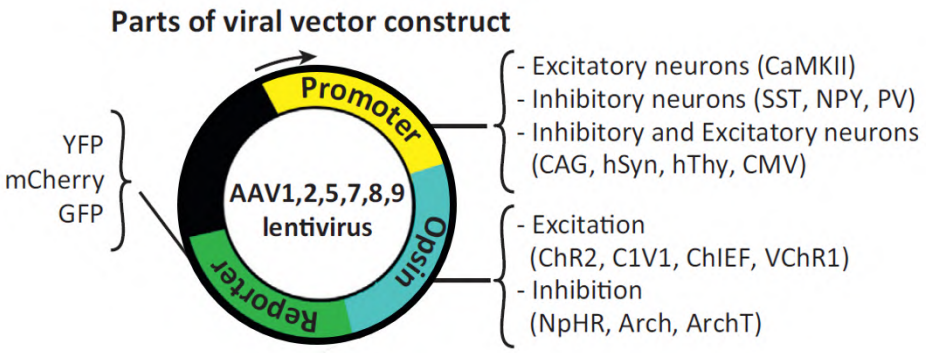

Figure 1.3: Example viral vector construct. Adapted from Gerits and Vanduffel (2013)

The cell type specificity is obtained by either the tropism of the vector itself, spatial targeting strategies or the choice of a specific promoter. The latter is the second building block of the vector construct. Some possibilities are denoted in figure 1.3. The third block is the genetic information of the opsin itself, which were already discussed in section 1.1.1. The final block is typical a reporter gene. These genes encode fluorescent proteins and are used to quantify opsin expression (Gerits and Vanduffel, 2013).

Other techniques can be used to circumvent the limitation of the packaging capacity. For instance, transgenic or knock-in animals can be used. Although this method gives a high specificity, it is only useful in studies as it cannot be extended to humans. Furthermore, it takes more effort and time to generate these transgenic lines. Also, if a new opsin is desired, a new mouse line needs to be generated. Finally, the specificity due to spatial localization is lost as well. A combination of transgenic mice, i.e. cre recombinase-based mouse lines, with viral vector system, combines the best of both worlds leading to an increased specificity (Guru et al., 2015). Some other techniques are electroporation, gene gun (Zhao et al., 2015), cell-to-myocyte electrical coupling with donor cells (Boyle et al., 2015), lipofection and optoporation (Mohanty et al., 2015). The latter should reduce the tissue damage and increase the site-specificity. This is obtained by using an ultra fast near infrared laser beam, that causes highly localized cell poration, in combination with micro-injection of the opsin-genes (Mohanty et al., 2015).

1.1.3 Illumination

Finally, only illumination of the genetically modified cells is left. Again there exist some possibilities to achieve this, with their flaws and improvements. The light can be generated by a mercury or xenon bulb, a light-emitting diode (LED), a continuous-wave laser or an ultrafast pulsed laser. The bulbs produce a wide spectrum of light, thus filtering is still needed. Furthermore, they create a lot of heat and degenerate more rapidly, hence they are used very rarely (Packer et al., 2013). When using optogenetics, it is recommended to use light with wavelengths near the peak wavelength of the opsin. In this case, lower intensities are needed, reducing the

chance of phototoxicity, photobleaching or spontaneous activation of the cells itself. Moreover, it creates the possibility for multicolored simultaneous activation. Also high temporal control is desired. These requirements make LEDs and laser more suitable candidates. The advantages of lasers are the production of coherent light, higher coupling efficiency and superior temporal resolution in ultrafast lasers, which can emit light pulses of tens to hundreds of femtoseconds long. The caveats are increased complexity and cost (Mohanty et al., 2015, Packer et al., 2013, Zhao et al., 2015).

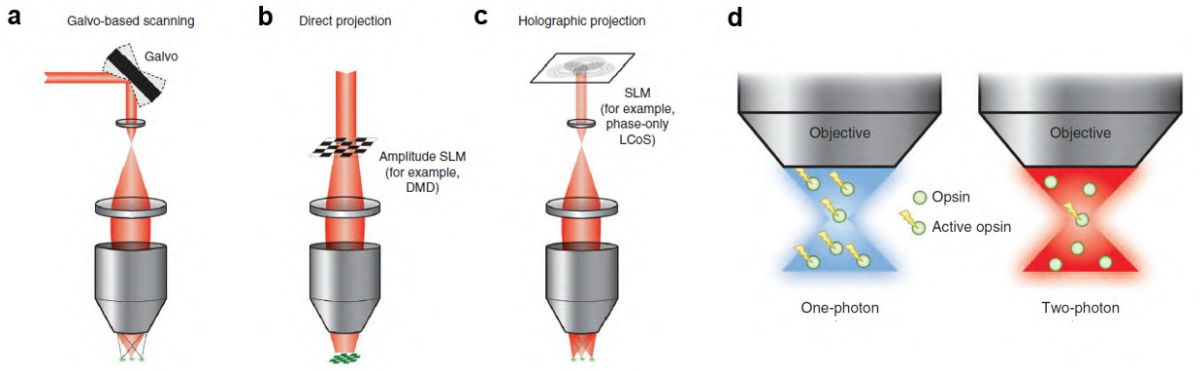

Figure 1.4: Illumination techniques for increased spatial specificity. (a) galvo-based scanning. (b) direct projection with digital micromirror. (c) holographic projection. (d) one vs two photon activation. Adapted from (Packer et al., 2013)

Figure 1.4 depicts some techniques to increase the spatial resolution. Simple focusing of the light beam increases the spatial resolution in the transverse plain dramatically. Although the light is out of focus axially, still it will be sufficient to stimulate other cells. This can be avoided by reducing the intensity of the source such that only at the focal point the intensity will be above the threshold. By using galvanometer mirrors, the light can then be directed onto the region of interest (see figure 1.4 (a)). However, better temporal control can be obtained by using spatial light modulators or digital micromirror devices (figure 1.4(b)). A third possibility is the use of holographic projection with an increased axial resolution but similar increased complexity (figure 1.4 (c)). The final technique is very promising. The use of visible light in one photon excitation gives a poor axial resolution and a lot of scattering resulting in a low penetration depth. Simulations have shown that after 1 mm, blue laser light gets attenuated for 90% (Mohanty et al., 2015). This is less of a problem for small rodents, but it creates a problem in primates when larger areas need to be stimulated. A solution is two photon activation. Here, an ultrafast pulsed NIR laser is used. The energy of NIR light is much lower than light of the visual spectrum and thus one photon is insufficient to activate the opsin. However, if two NIR photons arrive within femtoseconds of each other, the energy is combined and sufficient to activate. Due to this highly non-linear character, this happens only in the focal point of the laser. Consequently, this technique has a superior spatial resolution in both the transversal and axial plane. Moreover, because NIR-light is used, there is less scattering which makes non/minimal

invasive, *in vivo* stimulation possible (Mohanty et al., 2015, Packer et al., 2013, Petersen and Foustoukos, 2016).

1.2 Clinical translation

The discovery of optogenetics has revolutionized neurosciene. Due to its optimal temporal resolution, cell specificity and bidirectional control, the ability to activate or inhibit cells, it is an ideal investigative tool. The latter property has simplified behavioral studies, where causality needs to be investigated in terms of necessity and specificity. Consequently, optogenetics has proven to be very useful investigating disease mechanisms. Although there are still a lot of challenges along its path to be an effective clinical application, lots of studies have already shown its benefits and high potential.

1.2.1 Applications

Epilepsy

Epilepsy is a devastating disorder, which remains difficult to treat via pharmacological (only 50% effectively treated with AEDs) and electrophysiological means (Tønnesen and Kokaia, 2017), whereby more than 20% of the patients render with refractory epilepsy (Wykes et al., 2016). In case of partial epilepsies, seizures arise from focal areas. This makes it very perceptive for optogenetic neuromodulation. Studies have already shown its effectiveness in treating epileptic seizures in animal models. There are two strategies. First there is seizure control through optogenetic inhibition. Proof of principle, where successfully burst attenuation in pyramidal neurons with stimulation of NpHR was obtained, was provided by Tønnesen et al. (2009). Followed by *in vivo* successes by Krook-Magnuson et al. (2013) and Paz et al. (2013), where seizures were stopped or decreased in temporal lobe epilepsy with a hippocampal focus or thalamus inhibition (Tønnesen and Kokaia, 2017, Zhao et al., 2015). Alternatively, seizures can be controlled by exiting inhibitory interneurons. Again, *in vitro* and *in vivo* studies have proven optogenetic's potential, with ChR2 in PV-cre and SST-cre mouse brain slices by Kokaia et al. (2013) and ChR2 in PV-cre mice by Krook-Magnuson et al. (2013), Wykes et al. (2016).

Parkinson's disease

Parkinson's disease is one of the world's most common neurodegenerative diseases. The pathology concerns the degeneration of dopaminergic neurons in the substantia nigra pars compacta (SNc), giving birth to bradykinesia, tremor, walking problems and rigidity. The most popular treatment is administering L-DOPA. However, long-term use results in serious side effects such as dyskinesia and motor fluctuations (Chen et al., 2015, Petersen and Foustoukos, 2016, Yoon et al., 2016). High frequency deep brain stimulation (DBS) is a technology used to alleviate

these symptoms. However, the mechanism isn't completely clear and additionally it lacks cell specificity(Yoon et al., 2016). With optogenetics, multiple options arise. It is possible to directly activate the D1 receptor medium-sized spiny neurons, which results in activation of the direct pathway of the basal ganglia circuitry and thereby a decrease of the symptoms. This was shown *in vivo* by Kravitz et al. (2010). They also showed the expected increase in symptoms when the indirect pathway was activated with ChR2. Another strategy is to affect the subthalamic nucleus. Optogenetic inhibition results in an improvement of akinesia symptoms (Yoon et al., 2014) and L-DOPA induced dyskinesia(Yoon et al., 2016).

Beyond the brain

Optogenetics is not bounded to the central nervous system. Possible applications exist in the peripheral nervous system as well as other excitable tissues such as cardiac tissues and muscle cells. Already a lot of advancements have been made in the cardiovascular field. Again the advantage is the cell specificity. By using optical defibrillation, pain will be alleviated because surrounding skeletal muscles will not be stimulated (Boyle et al., 2015). Moreover, prolonged stimulation is possible due to the lack of electrochemical reactions, which occur with electrical stimulation. Bruegmann et al. (2010) provided already *in vivo* prove-of-concept by optogenetically altering the PQRS complex. Abilez et al. (2011) even successfully expressed ChR2 in human embryonic stem cells which where further differentiated into cardiomyocytes. Translating optogenetics to the spinal cord and peripheral nervous systems doesn't make it necessarily more accessible. They contain more complex and heterogeneous tissues, are very motile and the immune response is more prominent. However, it also creates the possibility for more diverse illumination techniques; from cuff implants to minimal and even non invasive techniques, such as transdermal illumination. The latter shows high potential for somatosensation and pain, however currently only with *in vitro* and *ex vivo* successes. Additionally, optogenetics shows potential in motor circuit control, where it may be able to therapeutically restore function to damaged spinal circuits (Alilain et al., 2008) and modulate lower motor neurons. Concerning the latter, optogenetics will be advantageous with respect to electrical stimulation, due to the physiological order of recruitment with less muscle fatigue as result(Llewellyn et al., 2010, Montgomery et al., 2016).

1.2.2 Hurdles

The aforementioned applications are only the top of the iceberg of all the possibilities with optogenetics. However, translation to clinical application awaits a difficult path. One of the hardest challenges is the translation from rodents to primates. The human brain is on average a 1000 times bigger than the brain of rodents (Tønnesen and Kokaia, 2017). Thus, while there are already many proof of concepts in rodents (e.g. by Aravanis et al. (2007) and see 1.2.1,), it's more difficult to obtain behavior control in primates. Diester et al. (2011) constructed an optogenetic toolbox for primates with stimulation of the motor cortex. Although there was clear

proof of optogenetic control of the neurons, no movements were evoked. A possible reason to explain this, is the small size of the stimulated region. Blue light gets already attenuated for 90% over a depth of 1 mm, such that approximately only 1 mm^3 around the tip is affected (Diester et al., 2011, Gerits and Vanduffel, 2013, Mohanty et al., 2015). Other possible explanations are the deep layer specificity, due combination of vector tropism and promoter; stimulation frequencies, which are typical lower (ChR2 reliable spiking up to 15 Hz) (Lin et al., 2009, Yizhar et al., 2011) in comparison with electrical stimulation (300-350 Hz); inactivation of wrong neuron population and triggering of compensation dynamics. There has already been put a lot of effort in circumventing these limitations, such as engineering red-shifted opsins for deeper penetration and opsins with increased kinetics such as ChETAs. The remaining hurdles and possible solutions are summarized in table 1.1. Nevertheless, there have also been successful studies with optogenetic techniques causing change in primate saccadic eye movement, where behavior is measured with greater precision (Cavanaugh et al., 2012, Jazayeri et al., 2012).

Table 1.1: Advantages and Hurdles for translation to clinical application with their possible solutions

Advantages	**Hurdles**	**Possible Solutions**
Cell specificity[all]	Toxicity of opsin expression[2,3,6,16]	Alter promoter vector combination[3]
High temporal resolution (ms)[all]	Heterogeneous light delivery and attenuation[2,3,6,7,14,16]	Branched fiber illumination[13], red-shifted opsins[2,5,6,13] or synthetic retinal analogues[1]
Rapid reversibility[5,6]	Heterogeneous opsin expression[2,3,6,7,14,16]	Multi site injection[10]
Co-expression and bidirectional control[3,5,6,15]	Small capacity of viral vectors limits co-expression[5,17]	
No electrochemical reactions[2,15]	No subset specificity[6,7]	INTERSECT[6], optoporation[9]
True electrical and fMRI recordings[14]	Reliable high frequency spiking[8,17]	ChETAs, ChEFs[5,6,8]
No extra need for cofactors (retinal) in mammals[17]	Non physiological behavior[6,7,16]	
Control studies are easy[17]	Antidromic activation[6,7]	
Silent in the dark (no effect on cell properties)[13]	Phototoxicity and bleaching[17]	High light sensitive opsins[17]
Applicable in Thalamus[11]	Invasivennes of optrodes[3,16,17]	Two photon stimulation[9,10], Nanoparticle upconversion[12]
Minimally invasive beyond the brain[2,14,15]	Synchronization of cells[6,7]	SFOs[6,7]
	Heating[17]	High light sensitive opsins[17], red-shifted opsins[2,5,6,13]
	Rapid evolution and discoveries delay clinical trials[14]	

1: Azimihashemi et al. (2014) 2: Boyle et al. (2015), 3: Diester et al. (2011), 4: Entcheva and Williams (2014), 5: Gerits and Vanduffel (2013), 6: Guru et al. (2015), 7: Häusser (2014), 8: Lin et al. (2009), 9: Mohanty et al. (2015) 10: Packer et al. (2013) 11: Paz et al. (2013) 12: Tao et al. (2018) 13: Tønnesen and Kokaia (2017), 14: Williams and Denison (2013), 15: Williams and Entcheva (2015), 16: Wykes et al. (2016) and 17: Yizhar et al. (2011)

Chapter 2

Neuronal Modeling

The brain contains two major classes of cells: the neurons and the glial cells. Approximately, there are 10^{11} neurons and even ten times as much glial cells. The latter are important for support, protection and homeostasis of the brain. Furthermore, each neuron has more than one thousand connections. This enormous amount of cells, together with the high variability between them, makes the brain extremely complex. However, it is thanks to the brain's activity that we are able to learn, behave and perceive the world. In order to understand its functioning, it is necessary to understand its fundamental component, i.e. the neuron.

In this chapter, the electrophysiology of a cell and the Hodgkin Huxley model will be discussed. The latter is the basis of all the neural models used in this thesis. This chapter is based on three sources: Petersen and Foustoukos (2016), Abbott and Dayan (2000) and Izhikevitch (2007), unless otherwise specified. Details are cited in the text.

2.1 Cell electrophysiology

Neurons are cells and like any cell, they are surrounded by a cell membrane. This consists of phospholipids, which create a bilayer of approximately 5 nm thick, making the cell permeable to lipophilic substances, limited permeable to water and impermeable to ions and other charged molecules. Consequently, it is possible to have a different intracellular ion concentration, with respect to the outside, causing the cell membrane to act like a capacitor.

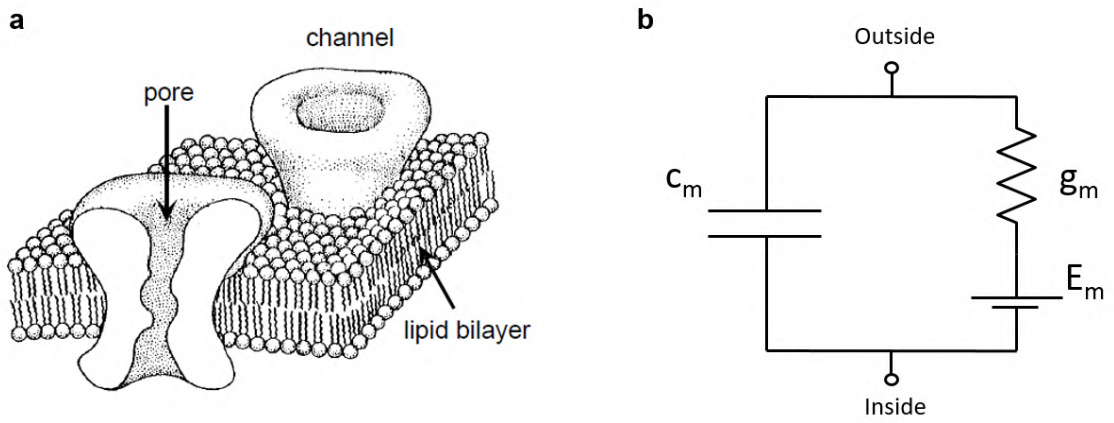

Figure 2.1: The cell membrane. (a) schematic diagram of a section of the cell membrane with two ion channels, adopted from (Abbott and Dayan, 2000). (b) simple equivalent circuit

Scattered across the membrane are numerous transmembrane proteins (see figure 2.1). These proteins enable movement of ions across the membrane. This is important for the signaling capabilities of the neuron and thus brain function. There are two types of transmembrane proteins: ion channels and transporters or pumps. Transporters use energy to pump ions against their electrochemical gradient, in order to maintain concentration gradients. Whereas, ion channels form an aqueous pore and allow high fluxes of ions down their electrochemical gradient. Many ion channels are highly selective for one ion. Typically they contain a charge filter, creating a cation or anion channel, superimposed with a size filter.

Globally, a cell contains mostly potassium (K^+) and anions, whereas extracellularly there is a more seawater like environment, i.e. sodium and chloride (Na^+ and Cl^-), with a high Ca^{2+} concentration (approximated values are given in table 2.1). In rest, there exist thus a negative potential across the membrane (by convention the outside is defined as zero). Hence, an ion is subjected to two forces. There is the force due to an electrical potential difference and due to the concentration gradient. At the equilibrium potential, these two forces cancel each other out such that there is no net current. In case of an ion channel that conducts for one ion, the

Table 2.1: Most important intracellular and extracellular ion concentrations with Nernst potentials. Numbers adapted from (Izhikevitch, 2007).

Ion	Intracellular	Extracellular	Equilibrium Potential
K^+	140 mM	5 mM	-90 mV
Na^+	15 mM	145 mM	61 mV
Cl^-	4 mM	110 mM	-89 mV
Ca^{2+}	100 nM	2.5 mM	136 mV

equilibrium potential of the ion channel can be computed with the Nernst equation:

$$E_x = \frac{RT}{zF} \ln \frac{[X]_{out}}{[X]_{in}} \tag{2.1}$$

where E_x denotes the equilibrium potential, R the universal gas constant, T the temperature, z the valence of the ion, F Faraday's constant, $[X]_{out}$ and $[X]_{in}$ respectively the extracellular and intracellular ion concentration. A cell is of course permeable to many ions. An ion channel, although highly specific, has some permeability for other ions as well. In case for monovalent ions the equilibrium or reversal potential can be calculated with the Goldman-Hodgkin-Katz (GHK) equation:

$$E_m = \frac{RT}{F} \ln \frac{\sum_i^n P_{M_i^+}[M_i^+]_{out} + \sum_j^m P_{A_j^-}[A_j^-]_{in}}{\sum_i^n P_{M_i^+}[M_i^+]_{in} + \sum_j^m P_{A_j^-}[A_j^-]_{out}} \tag{2.2}$$

where $[M_i^+]$ and $[A_j^-]$ are the concentrations of cation i and anion j respectively and P_{ion} the permeability for that ion. In case of multivalent ions, generalized forms of the GHK have been created (see Pickard (1976)).

2.1.1 The transmembrane current

As depicted in figure 2.1 (b), a cell can thus be modeled by the three components discussed above: a capacitor, a conductance/resistor and a voltage source being the cell membrane, the ion channels and equilibrium potential, respectively. A more detailed representation is given in figure 2.2. According to Kirchoff's law, the total current across the membrane is then calculated as follows:

$$i_m = c_m \frac{dV_m}{dt} + g_{K^+}(V_m - E_{K^+}) + g_{Na^+}(V_m - E_{Na^+}) + g_{Cl^-}(V_m - E_{Cl^-}) + g_{Ca^{2+}}(V_m - E_{Ca^{2+}}) \tag{2.3}$$

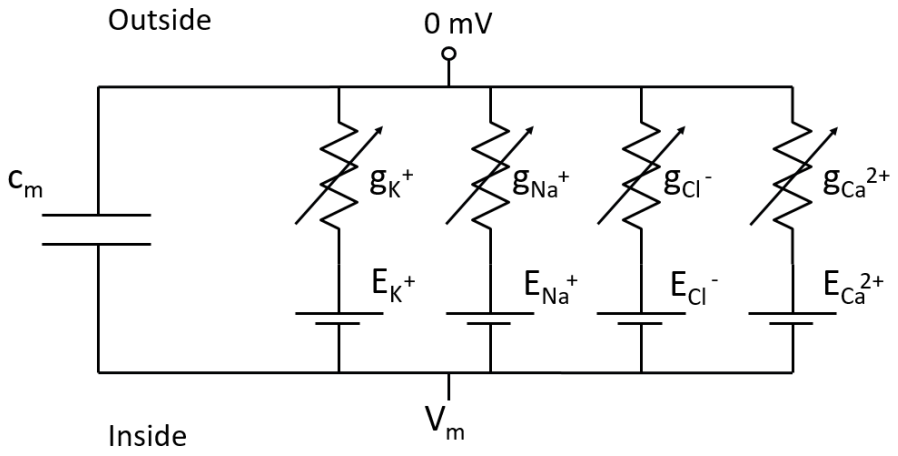

Figure 2.2: More detailed electric equivalent of a electrotonically compact cell. Varying conductances are indicated with arrows.

where E_{ion} and g_{ion} denote the reversal potential, calculated with the Nernst equation, and specific ion conductance, i.e. G_{ion}/A with A the membrane surface, of that ion channel, respectively; c_m is the specific membrane capacitance, i.e. again the membrane capacitance divided by the surface area: C_m/A; i_m is the total membrane current per unit area.

Approximated values of the reversal potentials are given in table 2.1. The driving factor of each current X is thus $(V_m - E_X)$. When V_m is higher (lower) than the reversal potential, there will be an outward (inward) current, driving V_m back to its reversal potential. At equilibrium the membrane voltage is thus defined by the reversal potentials and is closest to the one with the highest conductance. In steady-state conditions equation 2.3 turns into:

$$V_m = \frac{g_{K^+}}{g_{total}} E_{K^+} + \frac{g_{Na^+}}{g_{total}} E_{Na^+} + \frac{g_{Cl^-}}{g_{total}} E_{Cl^-} + \frac{g_{Ca^{2+}}}{g_{total}} E_{Ca^{2+}} \tag{2.4}$$

where $g_{total} = g_{K^+} + g_{Na^+} + g_{Cl^-} + g_{Ca^{2+}}$, which is called the specific total membrane or input conductance.

Although more detailed than figure 2.1 (b), figure 2.2 depicts still a basic equivalent of a cell. As will be shown later in this thesis, there are more and different types of currents, that need to be incorporated. Furthermore, sometimes equation 2.3 doesn't suffice and a more complex expression is required. This is typically in case of Ca^{2+} dependent channels where the Goldman-Hodkin-Katz formula is used to relate the membrane current to the corresponding conductance a potential:

$$i_X = P_X z_X^2 \frac{V_m F^2}{RT} \frac{[X]_{in} - [X]_{out} \exp(-z_X V_m F/RT)}{1 - \exp(-z_X V_m F/RT)} \tag{2.5}$$

where i_X is the specific membrane current for ion X; P_X is the permeability and z_X the valence of ion X. The other variables are the same as used in the functions above.

2.1.2 The axial current

In the previous section the cell is treated electrotonically compact, i.e. a cell with a uniform membrane potential across their surface. This suffices if a cell is modeled as one small, round compartment. However, in reality, a cell consists of different shaped compartments: dendrites, soma and axon (see figure 2.3). There exist thus a notable axial resistance (R_{Axial}), generating a spatial dependent membrane potential when the cells equilibrium is perturbed. This can be modeled by the cable equation:

$$\frac{R_m}{R_{Axial}} \frac{\partial V_m^2(x,t)}{\partial x^2} - R_m C_m \frac{\partial V_m(x,t)}{\partial t} - V(x,t) = 0 \tag{2.6}$$

Throughout this thesis, cells are mostly considered to be electrotonically compact. An exception is the two compartment LC-model in chapter 5, where the above equation is implemented according to the Rall-model (Feng, 2004).

2.2 The action potential

Although it is not valid for all neurons, they are very often defined as integrators. They receive inputs from other neurons at their dendrites. Here, post synaptic potentials are evoked. These travel down the dendritic tree towards the soma, the cell body of the neuron. At the axon hillock, these inputs are integrated over space and time. If the result is higher than the threshold, an action potential (see figure 2.5) is evoked, that travels down the axon towards the synapses. A schematic of two neurons is depicted in figure 2.3.

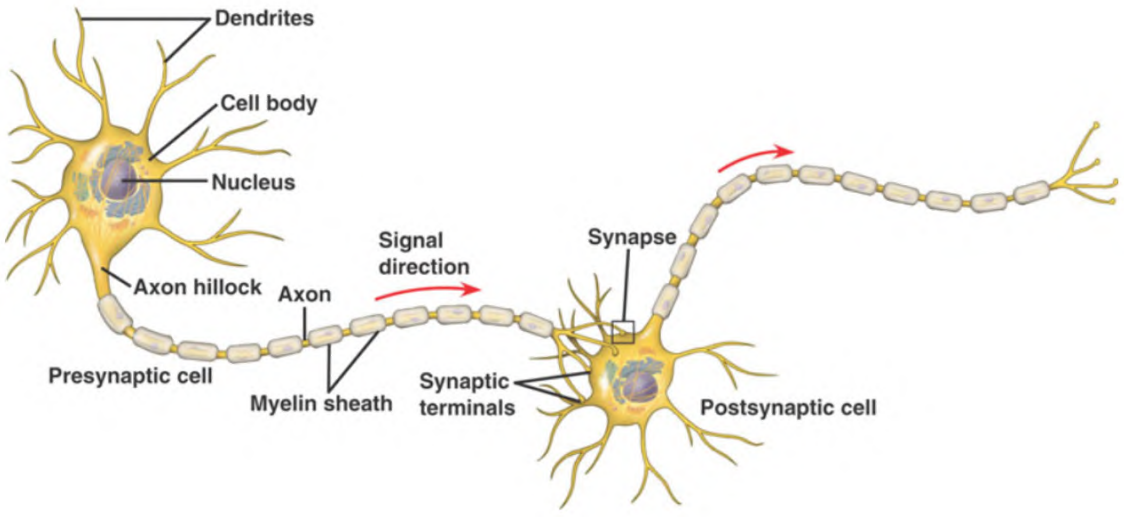

Figure 2.3: Schematic of two, through synapses, connected neurons. Adapted from (Marieb and Hoenn, 2015)

In the previous section only the passive behavior of a neuron is modeled. The capacitance and conductances are fixed over time. After perturbation of the neurons equilibrium potential, the membrane potential will converge back to its equilibrium. This happens both over time and space with $\lambda = \sqrt{\frac{R_m}{R_{axial}}}$ and $\tau = R_m C_m$ the length and time constant, respectively. The AP is an all-or-none signal. To model this, the active behavior of the cell needs to be incorporated. The conductance of many ion channels is variable and depend on multiple parameters: membrane potential, ion concentration, neurotransmitters, etc. This behavior is already depicted in figure 2.2, where the variability is indicated with arrows.

2.2.1 Voltage gated ion channels

During an AP, there is first depolarization, i.e. increase w.r.t. equilibrium potential, of the membrane potential followed by repolarization, i.e. decrease back to equilibrium potential and sometimes hyperpolarization, i.e. decrease w.r.t. equilibrium potential. Necessary for the generation of action potentials are voltage gated ion channels. These channels exhibit a non-linear I-V relationship (see figure 2.4 (a)).

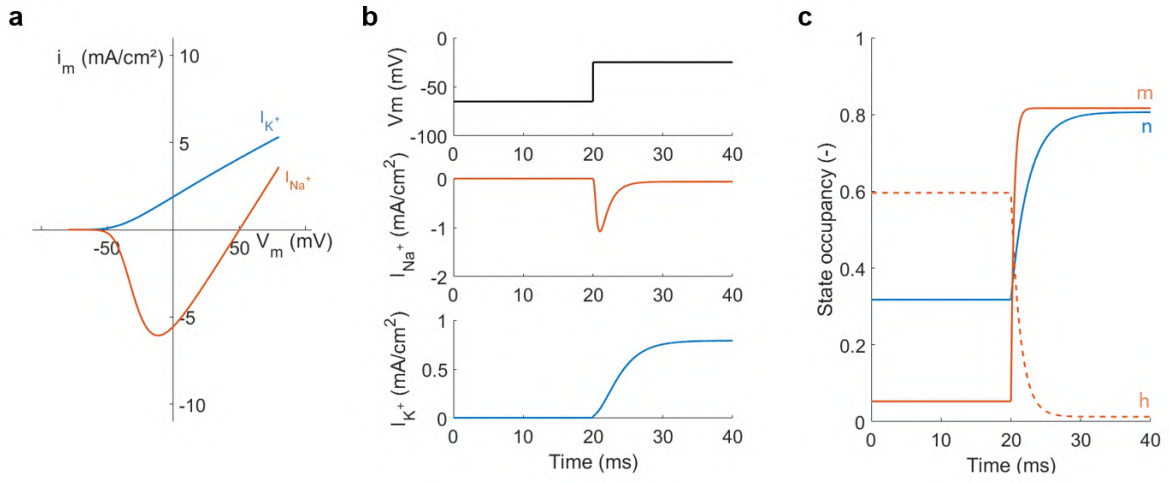

Figure 2.4: Voltage dependent ion channels. (a) the non-linear I-V relation of K^+ and Na^+ currents. (b) comparison transient and persistent current. (c) the gate probabilities of K^+ and Na^+ currents. Generated in MatlabR2017a with Hodgkin Huxley model (Abbott and Dayan, 2000)

2.3 Hodgkin Huxley

Hodgkin and Huxley were the first to measure an AP, this in a giant squid axon (Hodgkin and Huxley, 1990). They discovered that there are two currents on the basis of the AP. A fast transient sodium and slow persistent potassium current (see figure 2.4 (b)). Based on these measurements, they were also able to create an accurate model of the voltage gated channels and in turn the AP.

In the Hodgkin Huxley model, the currents are defined like in equation 2.3, i.e:

$$i_X = g_X(V_m - E_X) \tag{2.7}$$

The conductance, however, is variable and depends on the open probability of the channel. Therefore, this can be written as:

$$g_X = g_{X,max} \cdot P_X \tag{2.8}$$

where $g_{X,max}$ is the maximum conductance, i.e when the open probability $P_X = 1$. The latter is voltage dependent. This dependence is modeled by a particle gating scheme. According to Hodgkin and Huxley, there are two gating mechanism: activating and inactivating. The open probability can thus be calculated as follows:

$$P_X = m^a h^b \tag{2.9}$$

with a the number of activation gates, b the number of inactivation gates and m and h the activation and inactivation probabilities, respectively.

The slow persistent potassium current, also known as the delayed rectifier K^+ has no inactivation. Consequently, h can be set equal to one and thus be neglected. Furthermore, a is equal to four which is consistent with the fitted data of Hodgkin and Huxley and the four independent subunits that form the channel. The open probability is therefore equal to:

$$P_{K^+} = n^4 \tag{2.10}$$

here n is used as in the study of Hodgkin and Huxley and denotes the activation probability. The rate at which the open probability changes is given by:

$$\frac{dn}{dt} = \alpha_n(V) \cdot (1 - n) - \beta_n(V) \cdot n \tag{2.11}$$

where α_n depicts the rate from closed (1-n) to the open state (n) and β_n the reverse rate, as depicted below.

$$1 - n \underset{\beta_n}{\overset{\alpha_n}{\rightleftharpoons}} n$$

Very often the rate equation is expressed in another form:

$$\tau_n(V)\frac{dn}{dt} = n_\infty(V) - n \tag{2.12}$$

where

$$\tau_n(V) = \frac{1}{\alpha_n(V) + \beta_n(V)} \tag{2.13}$$

and

$$n_\infty(V) = \frac{\alpha_n(V)}{\alpha_n(V) + \beta_n(V)} \tag{2.14}$$

The advantage of this form is that, at a fixed V, n approaches the limiting value $n_\infty(V)$ exponentially with time constant $\tau_n(V)$.

The second current defining the AP is the fast transient sodium current. In contrast to the persistent current, this current does contain an inactivation gate. According to the fit of Hodgkin and Huxley, the Na^+ conductance contains three activation gates and one inactivation. The open probability can therefore be denoted as:

$$P_{Na^+} = m^3 h \tag{2.15}$$

with rate equations:

$$\frac{dm}{dt} = \alpha_m(V) \cdot (1 - m) - \beta_m(V) \cdot m \tag{2.16}$$

$$\frac{dh}{dt} = \alpha_h(V) \cdot (1 - h) - \beta_h(V) \cdot h \tag{2.17}$$

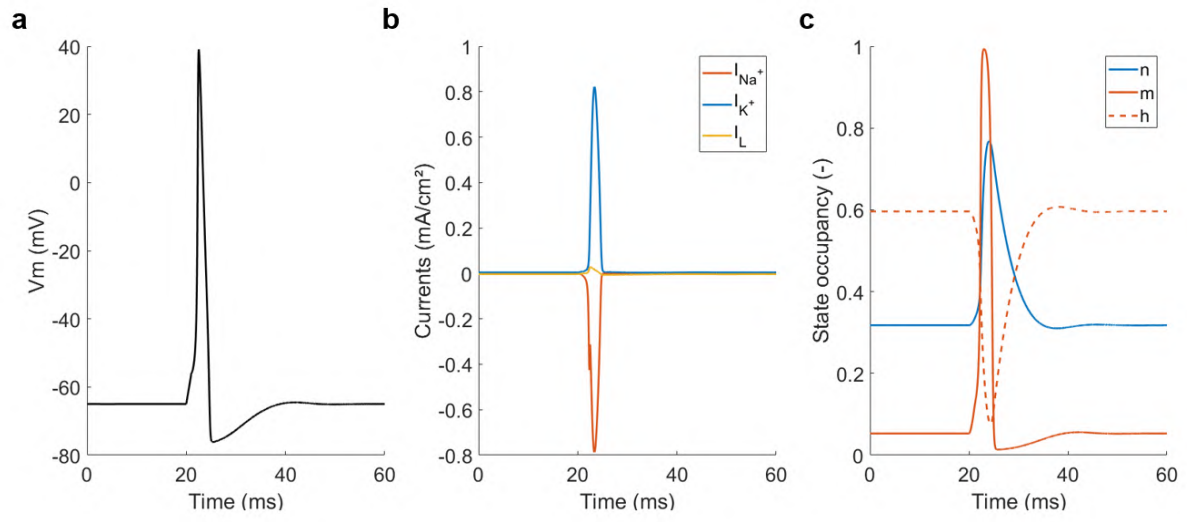

Figure 2.5: Action potential according to Hodgkin and Huxley model of giant squid axon. (a) AP. (b) individual currents. (c) gate probabilities of corresponding currents (color coded and generated with MatlabR2017a)

Both currents are depicted in figure 2.4 (b). When the cell is depolarized, first the activation probability of the sodium channel (m) increases. This is followed by an decrease of h resulting in inactivation. Together with the inactivation of the sodium channel, the activation probability of

potassium increases. The potassium channel remains open, until the cell repolarizes again (see figure 2.4 (c)). Also deinactivation of the sodium current occurs only after the cell is repolarized. This delayed deinactivation gives rise to the refractory period. There are two subdivisions. The absolute refractory period, during which it is not possible to fire another AP and the relative refractory period, where the threshold for AP firing is increased.

In their model for the generation of the action potential, Hodgkin and Huxley included three currents:

$$i_m = c_m \frac{\partial V}{\partial t} + i_{Na^+} + i_{K^+} + i_l \tag{2.18}$$

with i_{Na^+} and i_{K^+} the earlier discussed, fast transient sodium and persistent potassium current, respectively. I_l denotes the leakage current. This represents the time-independent currents. All currents are expressed per unit area. Combining equations 2.7, 2.8, 2.10, 2.15 and 2.18 this gives:

$$i_m = c_m \frac{\partial V}{\partial t} + g_{Na^+,max} m^3 h (V_m - E_{Na^+}) + g_{K^+,max} n^4 (V_m - E_{K^+}) + g_l (V_m - E_l) \tag{2.19}$$

This equation combined with equation 2.11, 2.16 and 2.17 form a set of coupled non-linear differential equations in V, n, m and h called the Hodgkin-Huxley equations. Figure 2.5 depicts the action potential generated with these equations and parameters of (Hodgkin and Huxley, 1990) shifted back with 65 mV. The differential equations were solved with an ode113 solver of MatlabR2017a with a maximum step of 10 μs. The equations were implemented in SI units, except for the membrane voltage, which is in (mV).

Chapter 3

Channelrhodopsin-2 Modeling

There is no doubt that, with its high cell specificity and temporal resolution, optogenetics wields high potential for neuromodulation tools. Nevertheless, there remain still some uncertainties, concerning its interference with the intrinsic network dynamics, effects on action potential waveforms, energetic efficiency, etc. To find an answer to these questions, an accurate quantitative model of ChR2 is required. Subsequently, in silico predictions can be made, investigating the optical response in realistic tissue and/or organ setting, which can be exploited for the development of *in vivo* tools (Grossman et al., 2011, Williams and Entcheva, 2015, Williams et al., 2013).

In this chapter, the dynamics of ChR2 will be unraveled. First, the expected photocycle will be discussed, followed by the proposed photocycle models. Subsequently, the implementation of the top notch four state ChR2(H134R) model, derived by Williams et al. (2013), in MatlabR2017a is described and validated. The chapter is concluded with a discussion of the implementation and flaws of the model.

3.1 The ChR2 photocycle

Under voltage clamp conditions, ChR2 has a very typical photocurrent. First there is an initial peak, which is reached within 1-2 ms. This is followed by a fast decay resulting in a steady-state plateau, which is caused by desensitization of the channel. Post-illumination, there is a bi-exponential decay back to baseline (see figure 3.1 (a)). Furthermore, upon second stimulation after short period of time (< 10 s), the transient response is reduced with a maintained steady-state current (see 3.1 (b)) (Nikolic et al., 2009).

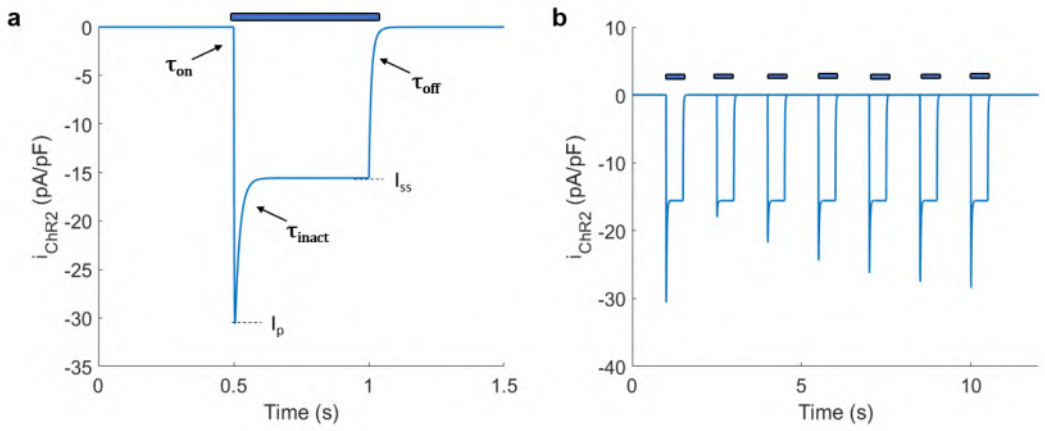

Figure 3.1: The channelrhodopsin-2 photocurrent. (a) The photocurrent for a single 0.5 s light pulse. (b) peak recovery kinetics. Light pulses are indicated with blue bars. Figure generated with MatlabR2017a, with model described in section 3.3

The expected photocycle is given in figure 3.2. A single cycle is based on UV/Vis and difference infrared spectroscopy measurements. The second cycle is to accommodate for the electrophysiological measurements and study results discussed in section 3.2. As already denoted in section 1.1.1, ChR comprises seven transmembrane helices combined with an retinal chromophore, creating a $RSBH^+$. Upon illumination, retinal absorbs photons, rendering it in an excited state. Within 150 fs, retinal deactivates triggering 13 trans-cis isomerization of retinal. After 2.7 ps the first intermediate is reached, i.e. P500 (or K). Next, the $RSBH^+$ is deprotonated, on a nanosecond timescale, giving rise to the blue shifted P390 (or L) state. This state is in equilibrium with the P520 (or M) state, exhibiting a reprotonated RSB. This state is the conducting state. Before returning back to the dark adapted state, D480, the channel converts to a non-conducting state P480. This happens on a millisecond timescale, while complete recovery takes seconds (Hegemann et al., 2005, Schneider et al., 2015, Stehfest and Hegemann, 2010).

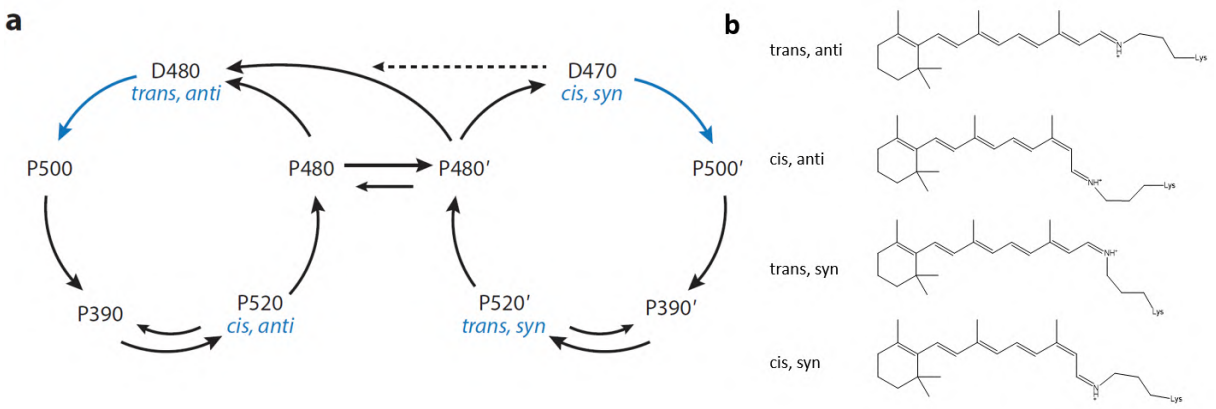

Figure 3.2: ChR2 photocycle. (a) Photocycle model for ChR2 implying photoactivation of two different dark states (D480 and D470) with distinct retinal configurations. The five states per cycle are based on UV/Vis and difference infrared spectroscopy measurements. Incorporation of second cycle is to accommodate for electrical measurements. Transition between the two cycles occurs in the presence of late P480 photointermediates. Light activation is indicated by blue arrows. (b) the retinal isomers. Adapted from (Schneider et al., 2015).

3.2 Photocycle models

Currently, the photocurrent is modeled with one of two major variants, i.e. a three-state and a four-state model. The proposed models are summarized in figure 3.3. Instead of going through different states before opening as in the photocycle, the opening is reduced to a single state transition. This is because the D480 $\rightarrow$ P500 and P500 $\rightarrow$ P390 transitions occur on a much faster timescale. Opening is thus modeled as a transition from the C $\rightarrow$ O state. The most straightforward model is figure 3.3 (a). After opening, it spontaneously turns into a closed, but desensitized state (D). This to model the transient to steady-state behavior. However, to obtain a steady state current the transitions O $\rightarrow$ D and D $\rightarrow$ O should be in the same order of magnitude. An alternative is figure 3.3 (b), where the desensitized state is reflected as a side reaction, like in the cycle for halorhodopsin (Hegemann et al., 2005). However, these models are unable to model accurately both the transition and recovery kinetics. This is due to the discrepancy between the need for fast transient kinetics and thus more or less equal rates for open to desensitized and desensitized to closed state, and slow recovery kinetics in the order of seconds. Even the model in figure 3.3 (c) where an extra transition is included, cannot explain the major properties observed in photocurrents (Hegemann et al., 2005).

Nagel et al. (2003) proposed a second photon absorption to circumvent this limitation. During illumination, there will thus be a slow D $\rightarrow$ C transition, superimposed with a fast, photochemical D $\rightarrow$ C transition as depicted in figure 3.3 (d). A second possibility is where the light induces photoactivation with reduced efficiency, which is shown in figure 3.3 (e) (Schneider et al., 2015, Stehfest and Hegemann, 2010). Both these three state models are able to predict relatively

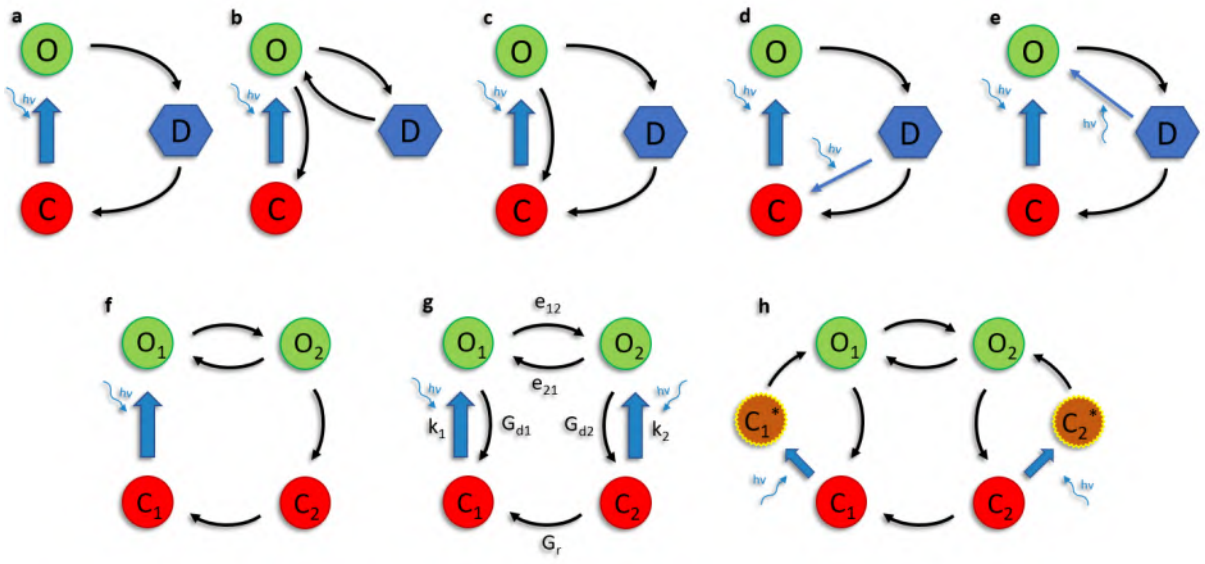

Figure 3.3: Proposed ChR2 photocycle models. (a) a three state cycle. (b) the desensitized state as side reaction. (c) cycle with partial recovery through D. (d,e) three cycle model with second light dependent step. (f) a four state circular model. (g) a four state branching model. (h) a six state model with two extra activation intermediates. (a-c) from Hegemann et al. (2005), (d,e) from Stehfest and Hegemann (2010), (f,g) from Nikolic et al. (2009) and (h) from Grossman et al. (2013)

accurate the transient behavior, the steady-state plateau, the fast decline after illumination and the slow recovery of transient current.

Although still not molecular identified (Stehfest and Hegemann, 2010), there is strong evidence for a two cycle model as depicted in figure 3.2. Bamann et al. (2008) identified four kinetic intermediates (P1, P2, P3 and P4) with a short flash experiment. P1 is only short lived, two of the intermediates are considered to be open states (P2 and P3) and P4 is a long-lived state. Furthermore, the selectivity changes between early and late photocurrents, i.e. a higher proton selectivity for steady-state currents (Schneider et al., 2015, Stehfest and Hegemann, 2010). Also, retinal extraction and Raman measurements indicate a mixture of retinal isoforms occurring in parallel. Four of these are depicted in figure 3.2 (b). Two of these , all-trans,15-anti and 13-cis,15-syn retinal, favor closed channel conformations by stabilizing a salt bridge between the RSB and the counterion complex. All-trans,15-syn and 13-cis,15-anti on the other hand may evoke formation of conducting states (Schneider et al., 2015). Moreover, the three state models are unable to reproduce the bi-exponential, post-illumination current decay. Finally, Bamann et al. (2008) showed that, when green light flashes were applied on top of a blue light stimulation, the current transiently closed, but overall still followed the inactivation. Neither this can be explained with a single photocycle model (Stehfest and Hegemann, 2010).

These finding imply the existence of two open and two closed states. Neglecting the fast inter-

mediate states, the photocycle can be reduced to a four state model. The simplest model is the circular four state model, as depicted in figure 3.3 (f). However, to predict both the fast closure under illumination and slow recovery after illumination, again a second photon absorption is needed just like in the case for the three state models (Nikolic et al., 2009, Schneider et al., 2015). The four state branching model (figure 3.3 (g)), all channel kinetics and dark recovery can be modeled properly. Here, C_1 depicts the fully dark adapted state. Upon illumination, there is a transition, with high quantum efficiency, to the first conducting state (O_1). Within milliseconds, the equilibrium between O_1 and O_2 is established. After the illumination, both conductance states convert to their respective closed state, C_1 and C_2, followed by a slow conversion from C_2 to C_1. The $C_2 \rightarrow O_2$ transition has a lower quantum efficiency than its counterpart. Furthermore, Nikolic et al. (2009) has shown the equilibrium between O_1 and O_2 to be light dependent. The six state model, as depicted in figure 3.3 (h), is an extended version of the four state model in figure 3.3 (g). The additional two intermediates are to correctly account for the activation time after retinal isomerizations and to avoid explicit time dependent rates (Grossman et al., 2013).

It is worth noting that the place of occurrence of the transition between the dark and light adapted cycles, respectively the left and right cycle (or C_1-O_1 and C_2-O_2) in figure 3.2 (a), is still under debate. However, most likely the transition occurs at the nonconducting states P480 and P480' (Nikolic et al., 2009, Schneider et al., 2015, Stehfest and Hegemann, 2010). Otherwise, the green flash experiment couldn't be explained. Second, the recovery is a little more complex as depicted in figure 3.2 (a), with a possible pH dependent equilibrium (not indicated).

3.3 Four state ChR2(H134R) model

3.3.1 The model

The ChR2 model used throughout this thesis, is a ChR2 model of the H134R mutant derived by Williams et al. (2013). Here, ChR2 is modeled with a four state Markov model, as depicted in figure 3.3 (g). Furthermore, it incorporates both the light and voltage dependent kinetics, an accurate inward rectification and is adjusted to physiological temperatures. The rate equations are denoted below:

$$O_1 + O_2 + C_1 + C_2 = 1 \tag{3.1}$$

$$dC_1/dt = G_r\, C_2 + G_{d1}\, O_1 - k_1\, C_1 \tag{3.2}$$

$$dO_1/dt = k_1\, C_1 - (G_{d1} + e_{12})\, O_1 + e_{21}\, O_2 \tag{3.3}$$

$$dO_2/dt = k_2\, C_2 - (G_{d2} + e_{21})\, O_2 + e_{12}\, O_1 \tag{3.4}$$

$$dC_2/dt = G_{d2}\, O_2 - (k_2 + G_r)\, C_2 \tag{3.5}$$

with C_1 the dark adapted closed state, C_2 the light adapted closed state, O_1 and O_2 the strong and weak conducting open states, respectively. The total occupancy of the state is equal to one. The transition rates are determined as follows:

$$k_1 = \phi_1(F,t) = \epsilon_1 F p \tag{3.6}$$

$$k_2 = \phi_2(F,t) = \epsilon_2 F p \tag{3.7}$$

$$F = \sigma_{ret} I \lambda/(w_{loss} \cdot h c) \tag{3.8}$$

$$dp/dt = (S_0(\theta) - p)/\tau_{ChR2} \tag{3.9}$$

$$S_0(\theta) = 0.5\,(1 + \tanh(0.120\,(\theta - 100))) \tag{3.10}$$

$$G_{d1} = 75 + 43\,\tanh((V + 20)/-20) \tag{3.11}$$

$$G_{d2} = 50 \tag{3.12}$$

$$G_r = 4.34 \cdot 10^{-2}\,\exp(-0.0211539274 \cdot V) \tag{3.13}$$

$$e_{12} = 11 + 5\,\ln(1 + I/24) \tag{3.14}$$

$$e_{21} = 8 + 4\,\ln(1 + I/24) \tag{3.15}$$

where k_1 and k_2 are both light sensitive and time dependent rate constants, with high and low quantum efficiency, respectively. F denotes the number of photons absorbed by ChR2 per unit of time, with light intensity I (W/m^2) at wavelength λ (m). p is the activation rate function. S_0 is an irradiance dependent sigmoid function, defining the activation rate in steady-state condition. θ is the optical stimulation protocol, with $\theta = 100\,I$. G_{d1} and G_{d2} denote the voltage dependent $O_1 \rightarrow C_1$ and constant $O_2 \rightarrow C_2$ transition rates, respectively. G_r is the slow voltage dependent recovery rate. Finally, e_{12} and e_{21} represent the intensity dependent transition rates between O_1 and O_2, respectively. All variables and constants are in SI units, except the membrane voltage (V), which is in mV. The remaining parameter values are summarized in table 3.1.

The advantage of this model is that it incorporates both the light and voltage sensitivity of ChR2, while others do only partly or not (Grossman et al., 2013, Nikolic et al., 2009, Talathi et al., 2011). The model is voltage dependent for both its conductance and kinetics. The current-voltage relationship of ChR2 is strongly non-linear as it shows inward rectification (Chater et al., 2010, Gradmann et al., 2011, Nagel et al., 2003). Williams et al. (2013) incorporated this with the empirical equation 3.17. Furthermore, the kinetics show some voltage dependence as well. Both activation and deactivation (τ_{on} and τ_{off}, see figure 3.1 (a)) are weakly voltage dependent. This is incorporated within G_{d1}, see equation 3.11. Also, the recovery rate is voltage dependent, with faster recovery at more negative potentials, reflected in G_r (equation 3.13). Finally, the

Table 3.1: ChR2(H134R) model parameters (Williams et al., 2013).

Definition	parameter	value	units
reversal potential ChR2	E_{ChR2}	0	mV
ratio of conductances of O_2/O_1	γ	0.1	-
max conductance	g_{ChR2}	4	S/m^2
quantum efficiency for photon absorption from C_1	ϵ_1	0.8535	-
quantum efficiency for photon absorption from C_2	ϵ_2	0.14	-
wavelength of maximal absorption for retinal	λ	470e-9	m
absorption cross-section for retinal	σ_{ret}	12e-20	m^2
scaling factor for losses of photons due to scattering or absorption	w_{loss}	1.3	-
time constant of ChR2 activation	τ_{ChR2}	1.3e-3	s
product of Planck's constant and the speed of light	hc	1.986446e-25	$kg\,m^3/s^2$

photocurrent is calculated as follows:

$$i_{ChR2} = g_{ChR2}\, G(V)\, (O_1 + \gamma O_2)\, (V - E_{ChR2}) \tag{3.16}$$

$$G(V) = [(10.6408 - 14.6408\, \exp(-V/42.7671))/V] \tag{3.17}$$

where g_{ChR2} is the maximal conductance, G(V) the rectification function, γ the ratio of conductance and E_{ChR2} the reversal potential.

3.3.2 Implementation in MatlabR2017a

To be able to use this model for further investigative purposes in this thesis, it is implemented in MatlabR2017a. The whole model from Williams et al. (2013) is converted to SI units (as already described above), except the membrane potential. Furthermore, because all the states sum up to one, the photocycle can be characterized with three independent variables (equations 3.1 - 3.4). Hence, the fourth rate equation (3.5) can be omitted. For validation purposes, the rectification function, as in equation 3.17, is used. However, this gives rise to physical impossible conductances around the reversal potential of zero volt. Namely, a conductance of $+\infty$ and $-\infty$ for the left and right limit, respectively. Therefore, after the validation, the rectification function

as described in Grossman et al. (2011) is used (equation 3.18).

$$G(V) = [(15 - 15\ \exp(-V/40))/V] \tag{3.18}$$

The differential equations are solved using a stiff ode15s solver, with relative tolerance and absolute tolerance of 10^{-10} and one twentieth of the pulse duration as max step. A stiff solver is needed as the model contains components that vary on drastically different timescales.

3.3.3 Validation

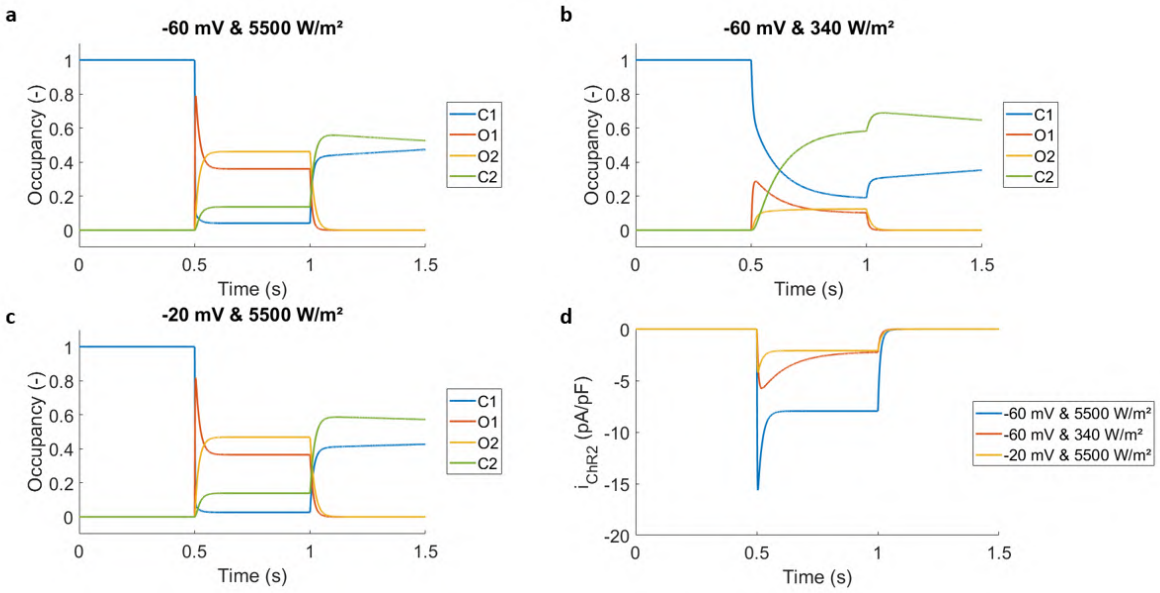

Figure 3.4: Voltage clamp simulations for varying conditions. (a-c) the state variables for indicated simulation conditions. (d) the photocurrents for the respective conditions.

First, a visual validation was performed. Figure 3.4 shows the results for voltage clamp simulations, with a light stimulus from 0.5 s to 1 s. The aforementioned photocurrent looks accurately modeled, with first a transient peak, followed by a steady-state plateau and fast off kinetics. Subfigures (a-c) depict the state occupancy. Before illumination, the channel is fully dark adapted, with C_1 occupancy equal to one. At stimulation onset, a fast $C_1 \rightarrow O_1$ transition is observed, followed by the creation of an equilibrium between the four states. Post illumination, there is a fast decrease of the open states, followed by a slow transition from $C_2 \rightarrow C_1$, which depicts the recovery. Comparison of figures 3.4 (a and b), shows a clear irradiance dependence, with a pronounced effect on the inactivation kinetics and equilibrium. The voltage dependence is less pronounced for the states occupancies, see figures 3.4 (a and c). This is due to the high intensity of the stimulation pulse. As a result the k_1 and k_2 rate constants (equations 3.6 and 3.7) are an order of magnitude higher than G_{d1} and G_{d2} (equations 3.11 and 3.12). This gives

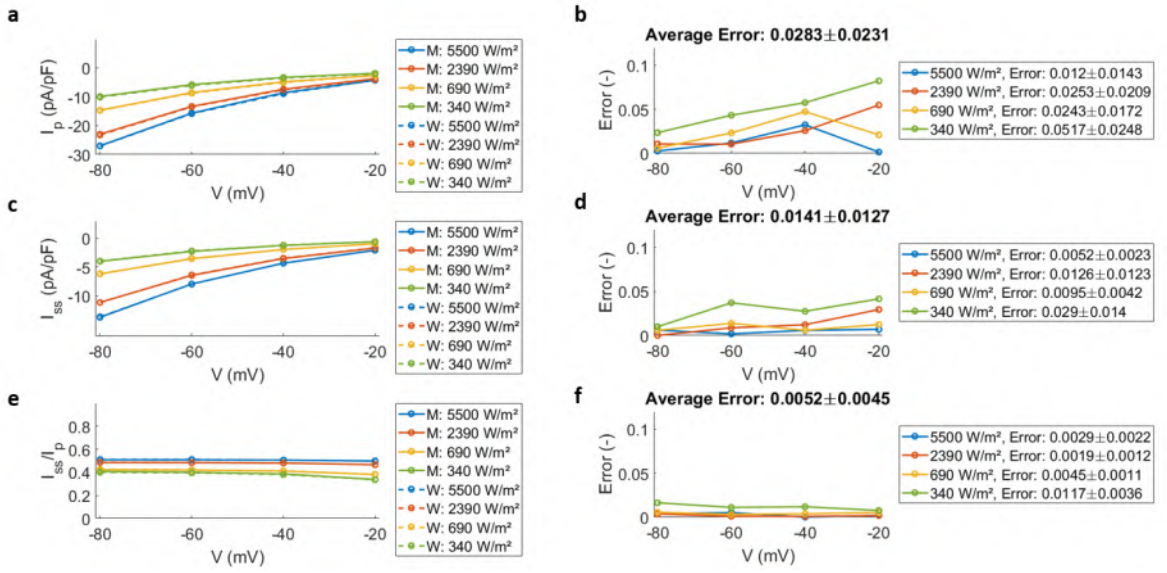

Figure 3.5: Current validation. (a,b) the peak current with respective errors. (c,d) steady-state current with respective errors. (e,f) current ratio with respective errors. Errors on top are averaged errors for all conditions. Errors in legend are averaged across voltage. M and W indicate generated by model and data from paper Williams et al. (2013), respectively

rise to a neglectable influence of the last two. From these results, a correct implementation can be assumed.

To be sure that, the model is implemented correctly, a validation of the currents and kinetics is performed with respect to the data generated by Williams et al. (2013). Their curves were extracted via the "WebPlotDigitizer"[1]. This to be able to calculate the errors as depicted in the figures below. The comparison of the peak and steady-state current is shown in figure 3.5. For a 0.5 s stimulation pulse, the peak current was determined as the maximum current (peak) and the steady-state as the mean between 0.4 s and 0.45 s after pulse onset. The normalized error, i.e $(abs(Data_{Williams,\ et\ al.} - Data_{Simulated})/abs(Data_{Williams,\ et\ al.})$ is depicted on the right. A neglectable error is observed ($< 3\%$), for which the data extraction method can be accounted for.

Next, the kinetics are compared. The results are shown in figure 3.6. To extract the time constants, mono-exponential curves were fit onto three segments of the photocurrent. The segmentation was based on the description by Williams et al. (2013), with a slight adaption as bad results were obtained (not shown here). For τ_{on}, the current section starting at pulse onset and ending at time of peak was used. For τ_{inact}, this was from 10 to 110 ms after time of peak and for τ_{off} between 500 ms and 600 ms after peak. The curve fit was performed with

[1] WebPlotDigitizer: Web based tool to extract data from plots, images and maps. Version 4.1 Released January 8, 2018. Available at: *https://automeris.io/WebPlotDigitizer/*

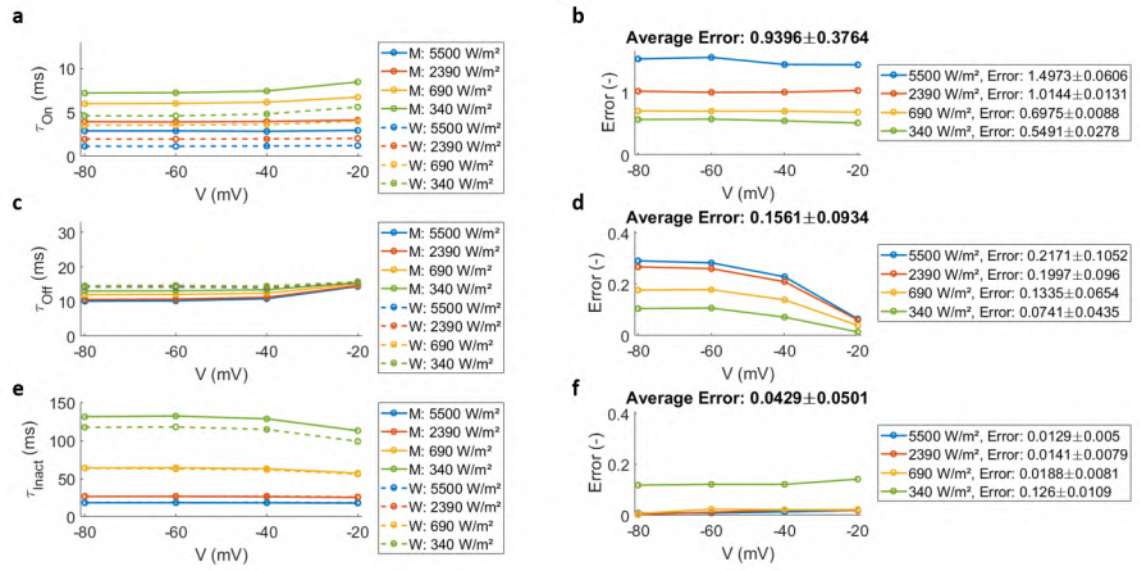

Figure 3.6: Time constants validation with mono-exponential fits. (a,b) the on kinetics with respective errors. (c,d) the off kinetics with respective errors. (e,f) the inactivation kinetics with respective errors. Errors on top are averaged errors for all conditions. Errors in legend are averaged across voltage. M and W indicate generated by model and data from paper Williams et al. (2013), respectively

the Global Solver Toolbox available in MatlabR2017a with multi start of 100 to ensure optimal fit. A "least-square curve" fit with "trust-region" algorithm was used with variable tolerance of 10^{-12}, minimum and maximum step size 10^{-12} and 0.1, respectively, and maximum number of 600000 iterations and function evaluations as criterion for termination.

As depicted in figure 3.6 on the right, the errors are rather high. In case of τ_{on}, there is a vast overestimation for all conditions. For the off kinetics, there is a slight underestimation and for the inactivation kinetics, there is an overall good result except for low irradiances. Although, this is indicative for bad implementation, the difference can also be due to the fitting method. In case of τ_{on} a mono-exponential fit is used. However, the rise of the current has a typical sigmoid shape. Furthermore, also a mono-exponential fit is used for the off kinetics, while research has clearly stated a bi-exponential decay. Therefore, a logistics curve (equation 3.20) is fitted for all time constants and a bi-exponential curve (equation 3.21) for τ_{off} only. Figure 3.7 depicts the fit for each current segment of a -80 mV and 5500 W/m^2 simulation. The R^2 values in figure 3.7 (d) indicate a slight better fit with logistics, mono-exponential and bi-exponential for τ_{on}, τ_{inact} and τ_{off}, respectively.

$$\text{Mono-exponential: } b(1)\ \exp(\frac{-t}{b(2)}) + b(3) \tag{3.19}$$

$$\text{Logistics: } \frac{b(1)}{1 + \exp(\frac{-t}{b(2)})} + b(3) \tag{3.20}$$

$$\text{Bi-exponential: } b(1)\ \exp(\frac{-t}{b(2)}) + b(3)\ \exp(\frac{-t}{b(4)}) + b(5) \tag{3.21}$$

τ_{on} derived from the logistics curve fit, is shown in figure 3.8. The error is extremely reduced with respect to the time constant extracted via the mono-exponential fit, indicative that a logistics fit might be used by Williams et al. (2013), as well. In case of τ_{off}, although unable to compare

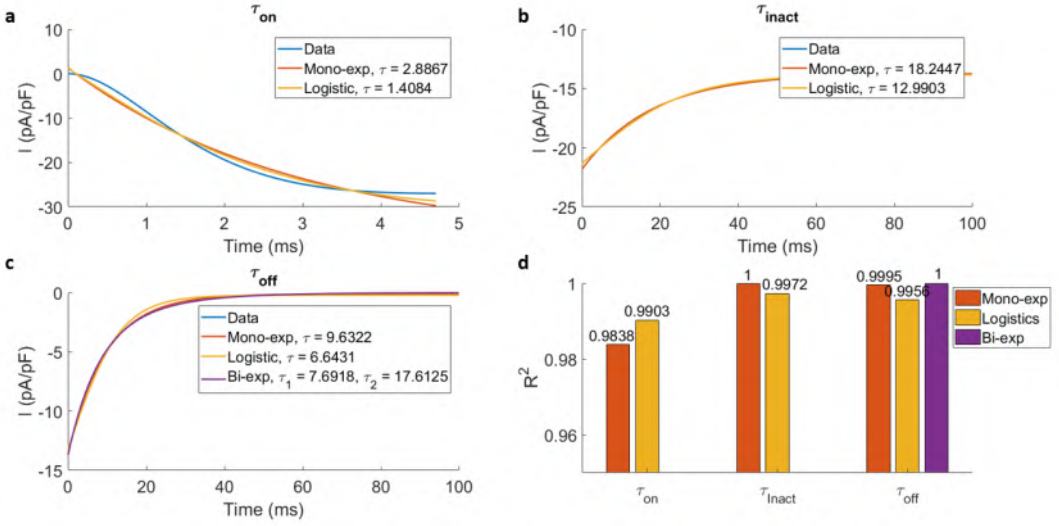

Figure 3.7: Derivation of τ_{on}, τ_{inact} and τ_{off} by fitting of mono-exponential and logistics curves, additional a bi-exponential curve for τ_{off}, on current segments. (a-c) curve segments with fits. (d) bar graph representing the goodness-of-fit with R^2 values. Stimulation conditions are V = −80 mV and I = 5500 W/m^2

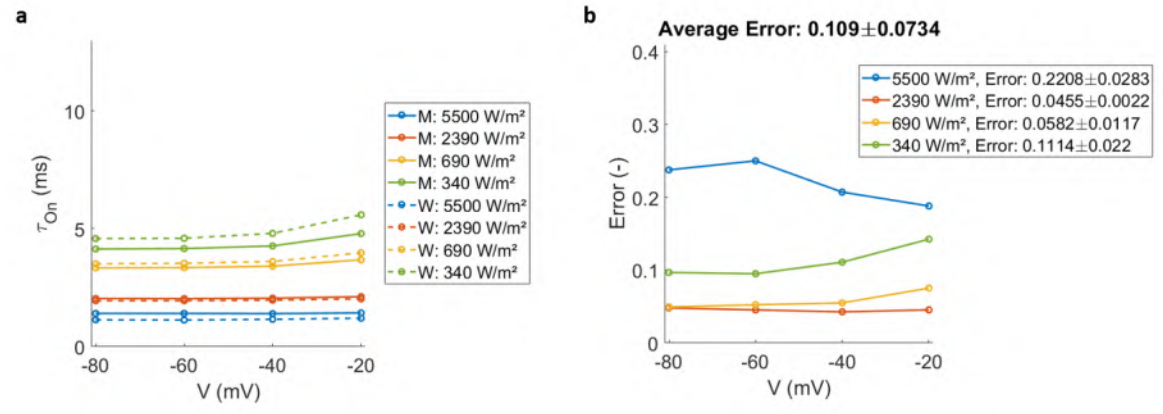

Figure 3.8: Time constants validation with logistics fit. (a) logistics fit on τ_{on}. (b) respective errors. Error on top is the averaged error for all conditions. Errors in legend are averaged across voltage. M and W indicate generated by model and data from paper Williams et al. (2013), respectively

directly, the order of magnitude can be checked with literature. Figure 3.9 denotes clearly, two distinct time constants in case of bi-exponential fit. The total off kinetics is thus a combination

of a fast and slow component. Furthermore, the kinetics are independent of the irradiance, as they are expected to be (Nikolic et al., 2009).

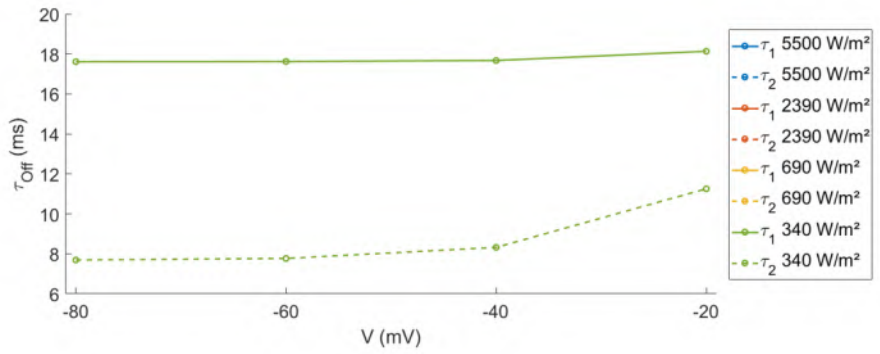

Figure 3.9: Time constants for off kinetics, with bi-exponential fit. The curves coincide for different irradiances

Finally, there rests the validation of the recovery kinetics. Figure 3.10 shows both the peak current ratio with respect to the inter pulse interval and the extracted recovery time constant. Interesting to see is that, while there is a neglectable error for the current ratio, there is a non neglectable error for the time constant.

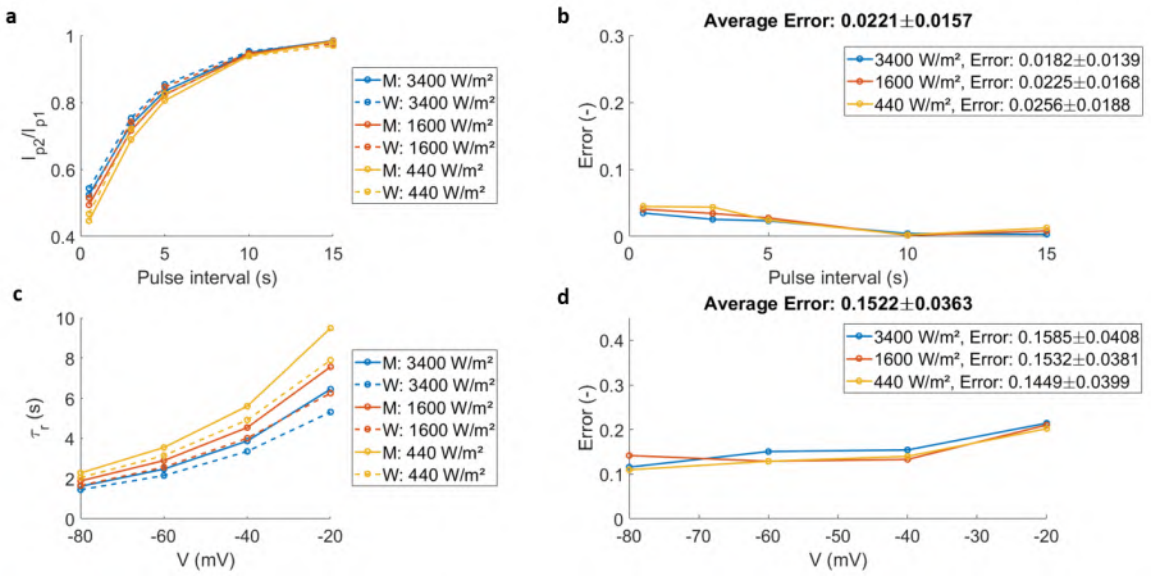

Figure 3.10: Recovery kinetics validation. (a,b) ratio of peak currents (I_{p2}/I_{p1}) with respective error. (c,d) Voltage dependence of τ_r with respective error. Errors on top are averaged errors for all conditions. Errors in legend are averaged across voltage. M and W indicate generated by model and data from paper Williams et al. (2013), respectively

3.3.4 Discussion

The results above bring the implementation in question. However, in case of the recovery kinetics, the time constant is directly extracted from the current ratio (figure 3.10 (a)), but gives a greater error. Therefore, the manner of determination of the time constant is rather questionable than the implementation of the model itself. This can be extended to the other time constants as well. Reasons for this discrepancy could be: the fixed current segments and the unevenly distributed data points, used for the curve fits. Moreover, the error introduced by the extraction method cannot be omitted. Finally, there is a neglectable error of the currents. Hence, although the kinetics do not match perfectly, from the results above there can be concluded that it is rather a problem of extraction of the time constants than the implementation of the model itself.

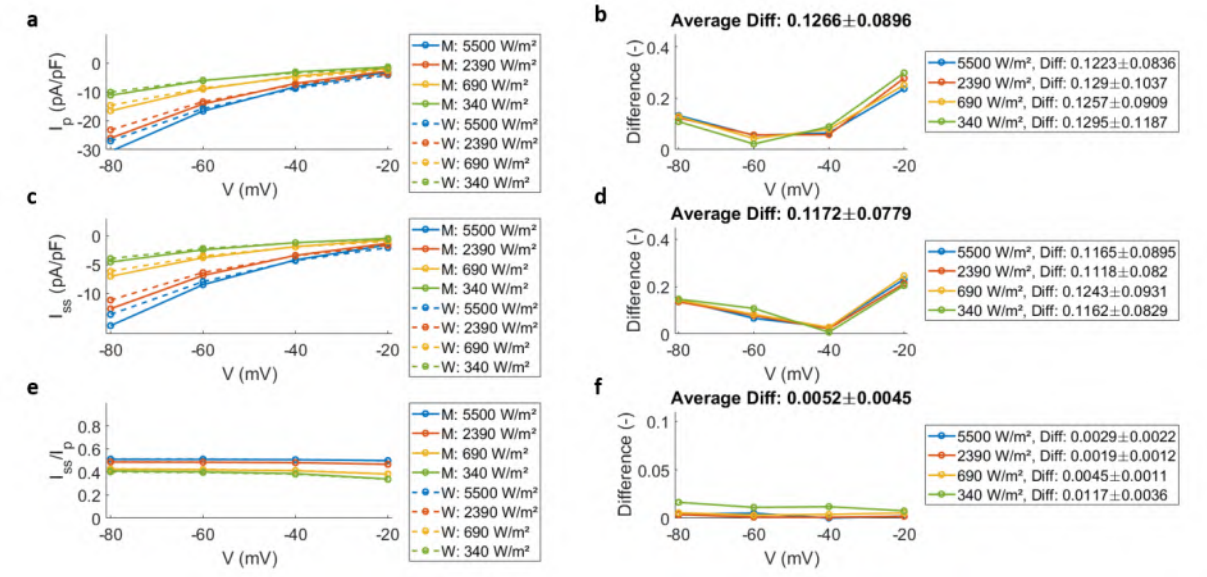

Figure 3.11: Effect of G(V) on current. (a,b) the peak current with respective differences. (c,d) steady-state current with respective differences. (e,f) current ratio with respective differences. Differences on top are averaged differences for all conditions. Differences in legend are differences across voltage. M and W indicate generated by model and data from paper Williams et al. (2013), respectively

As already denoted in section 3.3.2, due to the physically impossible conductance, another rectification function is used during the rest of the thesis, i.e. equation 3.18. The effect of this is shown in figure 3.11. This leads to a difference of around 10%. However, this is still an empirically derived function. There are other possibilities to implement the rectification. Gradmann et al. (2011) discussed several mechanisms. First, there is the familiar GHK model (see equation 2.2). However, this gives a too small curvature. Second, there is the fit with single asymmetric barrier, which gives better rectification but with unrealistic assumptions. Also, a general, fast binding and fast reorientation reaction scheme for enzymatic translocation of ionic

substrates was investigated. These gave better fits than the first two, but at the cost of a vast increase in complexity. For example, the general model gave an excellent fit but consisted of twelve free parameters.

Not included into the model is the pH dependence of the channel. Nagel et al. (2003) detected that the kinetics depended both on intra- and extracellular pH. The recovery rate is affected by the extracellular pH. The more acidic (lower pH), the faster the recovery. On the other hand, the off kinetics depend on the intracellular pH. Here the adverse effect is observed, with lowering of the off kinetics at lower pH. Finally, there is expected to be a complete recovery to the dark adapted state. However, there exist evidence of pH dependent equilibrium between the two closed states (Stehfest and Hegemann, 2010, Williams et al., 2013). To account for this an extra transition can be implemented going from C_1 to C_2 (Williams et al., 2013).

Chapter 4

Electrical versus Optical Stimulation in the Subthalamic Nucleus

The basal ganglia is an anatomical structure, deep within the cerebral hemispheres, consisting of the striatum, globus pallidus, subthalamic nucleus and substantia nigra. That, furthermore, plays an important role in motor control and voluntary movement. A typical disease associated with this region is Parkinson's disease. The underlying pathology is the loss of dopaminergic neurons in the substantia nigra pars compacta, which causes irregular activity of the basal ganglia. To alleviate the symptoms, high frequency deep brain stimulation is applied onto the STN, which is suggested to play a pivotal role in voluntary movement control and acts a driving force of the basal ganglia (Otsuka et al., 2004, Purves et al., 2004).

Due to the presence of some severe limitations acquainted with electrical stimulation in the brain, it is interesting to investigate the effect of optogenetic stimulation on STN neuron regulation, as possible alternative. This chapter focuses on the comparison between these two stimulation sources. Initially, the STN neuron model derived by Otsuka et al. (2004) is implemented into MatlabR2017a. Subsequently, the stimulation protocols are described, followed by a discussion of the results. These results are submitted as conference paper to the EMF-MED 2018 world conference on biomedical applications of electromagnetic fields.

4.1 Subthalamic nucleus model

The model used for the subthalamic nucleus neuron is a conductance-based model derived by Otsuka et al. (2004). Here, the STN is modeled as electrotonically compact with seven transmembrane currents: a sodium current (i_{Na}), a delayed rectifier potassium current (i_K), an A-type potassium current (i_A), a L-type calcium current (i_L), a T-type calcium current (i_T), a calcium dependent potassium current (i_{Ca-K}) and a leakage current (i_l). The membrane potential is thus described as follows:

$$c_m \frac{dV}{dt} = -i_{Na} - i_K - i_A - i_L - i_T - i_{Ca-K} - i_l \tag{4.1}$$

where c_m is the specific membrane capacitance. The currents are of the Hodgkin-Huxley type as described in section 2.3. The equations are depicted below:

$$i_{Na} = g_{Na}\, m^3\, h\, (V - E_{Na}) \tag{4.2}$$

$$i_K = g_K\, n^4\, (V - E_K) \tag{4.3}$$

$$i_A = g_A\, a^2\, b\, (V - E_K) \tag{4.4}$$

$$i_L = g_L\, c^2\, d_1\, d_2\, (V - E_{Ca}) \tag{4.5}$$

$$i_T = g_T\, p^2\, q\, (V - E_{Ca}) \tag{4.6}$$

$$i_{Ca-K} = g_{Ca-K}\, r^2\, (V - E_K) \tag{4.7}$$

$$i_l = g_l\, (V - E_l) \tag{4.8}$$

where the currents are expressed in A/m^2; g_{Na}, g_K, g_A, g_L, g_T, g_{Ca-K} and g_l are the maximal conductances, with their values shown in table 4.2; E_{Na}, E_K, E_{Ca} and E_l are the reversal potentials of the sodium, potassium, calcium and leak current, respectively, with their values summarized in table 4.2 as well; a, b, c, d_1, d_2, h, m, n, p, q and r are the activation and inactivation gating variables, with the gate rate equations expressed like in equation 2.12. For convenience, this equation is repeated here:

$$\frac{dw}{dt} = \frac{w_\infty(V) - w}{\tau_w(V)} \tag{4.9}$$

where w stands for the gating variables: a, b, c, d_1, d_2, h, m, n, p, q or r.

E_{Ca}, however, is not constant. Its value depends on the intracellular calcium concentration, that in turn depends on the total calcium current. The change in intracellular calcium concentration can be calculated as follows:

$$\frac{d[Ca]_i}{dt} = -\frac{i_{Ca}}{z\, F\, d} - \frac{[Ca]_i}{\tau_{Ca}} \tag{4.10}$$

with F the Faraday constant, z the valence of calcium ions, d the specific depth, τ_{Ca} the calcium

decay time constant and i_{Ca} the sum of all calcium currents, i.e. $i_L + i_T$. E_{Ca} is then calculated with the Nernst equation (see equation 2.1), with an extracellular concentration ($[Ca]_o$) equal to 2 mM.

Table 4.1: Rate functions of STN model derived by Otsuka et al. (2004), in SI units (except V, which is in mV)

Gating variable	Steady-state function (w_∞)	Time constant (τ_w)
m	$\frac{1}{1+\exp(-\frac{(V+40)}{8})}$	$10^{-3} \cdot (0.2 + \frac{3}{1+\exp(\frac{V+53}{0.7})})$
h	$\frac{1}{1+\exp(\frac{(V+45.5)}{6.4})}$	$10^{-3} \cdot (\frac{24.5}{\exp(\frac{V+50}{15})+\exp(-\frac{V+50}{16})})$
n	$\frac{1}{1+\exp(-\frac{(V+41)}{14})}$	$10^{-3} \cdot (\frac{11}{\exp(\frac{V+40}{40})+\exp(-\frac{V+40}{50})})$
a	$\frac{1}{1+\exp(-\frac{(V+45)}{14.7})}$	$10^{-3} \cdot (1 + \frac{1}{1+\exp(\frac{V+40}{0.5})})$
b	$\frac{1}{1+\exp(\frac{(V+90)}{7.5})}$	$10^{-3} \cdot (\frac{200}{\exp(\frac{V+60}{30})+\exp(-\frac{V+40}{10})})$
c	$\frac{1}{1+\exp(-\frac{(V+30.6)}{5})}$	$10^{-3} \cdot (45 + \frac{10}{\exp(\frac{V+27}{20})+\exp(-\frac{V+50}{15})})$
d_1	$\frac{1}{1+\exp(\frac{(V+60)}{7.5})}$	$10^{-3} \cdot (400 + \frac{500}{\exp(\frac{V+40}{15})+\exp(-\frac{V+20}{20})})$
d_2	$\frac{1}{1+\exp(\frac{([Ca]^*-0.1)}{0.02})}$	$10^{-3} \cdot 130$
p	$\frac{1}{1+\exp(-\frac{(V+56)}{6.7})}$	$10^{-3} \cdot (5 + \frac{0.33}{\exp(\frac{V+27}{10})+\exp(-\frac{V+102}{15})})$
q	$\frac{1}{1+\exp(\frac{(V+85)}{5.8})}$	$10^{-3} \cdot (\frac{400}{\exp(\frac{V+50}{15})+\exp(-\frac{V+50}{16})})$
r	$\frac{1}{1+\exp(-\frac{([Ca]^*-0.17)}{0.08})}$	$10^{-3} \cdot 2$

$^*Ca^{2+}$ *concentration in* μM

4.2 Simulations

This model is implemented in MatlabR2017a. Next, a distinction is made between electrical and optical stimulation. In case of electrical stimulation, a set of thirteen differential equations (equation 4.1, 4.9 for the eleven gating variables and 4.10) is solved with a non-stiff ode113 solver. A max step of 10 μs is applied with no boundaries for relative and absolute tolerances. However, this max step is changed when small pulses are applied. Then, the max step is set to one twentieth of the pulse duration (Reilly et al., 1985, Tarnaud et al., 2018). As initial conditions, the rate equations are evaluated in steady-state conditions, i.e. $dw/dt = 0$, with V equal to the resting membrane potential (V_{m0}). The value of the resting intracellular calcium

Table 4.2: STN model parameters (Otsuka et al., 2004).

Definition	**parameter**	**value**	**units**
max conductance of Na channel	g_{Na}	490	S/m^2
reversal potential Na current	E_{Na}	60	mV
max conductance of delayed-rectifier K channel	g_K	570	S/m^2
reversal potential K current	E_K	-90	mV
max conductance of leakage channel	g_l	3.5	S/m^2
reversal potential leakage current	E_l	-60	mV
max conductance of T-type Ca channel	g_T	50	S/m^2
max conductance of L-type Ca channel	g_L	150	S/m^2
max conductance of A-type K channel	g_A	50	S/m^2
max conductance of Ca activated K channel	g_{Ca-K}	10	S/m^2
resting membrane potential	V_{m0}	-58	mV
calcium decay time constant	τ_{Ca}	0.5e-3	s
specific membrane capacitance	c_m	0.01	F/m^2
specific depth	d	10236e-9	m
extracellular Ca concentration	$[Ca]_o$	2e3	μM
resting intracellular Ca concentration	$[Ca]_{i,0}$	5e-3	μM

concentration is depicted in table 4.2. In case of optical stimulation, the aforementioned rate equations are joined by three rate equations (equations 3.2 - 3.4) of the ChR2 model, because one can be omitted as denoted in section 3.3.2. Furthermore, the same stiff ode15s solver, described in section 3.3.2, is used with relative and absolute tolerance of 10^{-10}. The max step is equal to the one applied in case of electrical stimulation. Also the same initial conditions, with additional C_1 equal to one and the open states equal to zero, are used.

4.2.1 Methodology

Three topics are studied. First, the effect of a constant pulse on the firing rate is investigated. The protocol that is used, consists of three intervals. Initially, there is a one second, free period. This is followed by the stimulus with predefined pulse duration. The simulation is ended with again a one second stimulation free period. Multiple combinations of pulse duration and amplitude are used. The set of pulse durations is the same for both electrical and optical stimulation, i.e. $[0.01, 0.02, ..., 0.1, 0.2, ..., 1, 2, ...10]$ s. The applied stimulation amplitudes are $[1, 2, ..., 10, 20, ..., 100, 200, ..., 1000, 2000..., 10000]$ W/m^2 and $[0.001, 0.002, ..., 0.01, 0.02, ..., 0.1, 0.2, ..., 1]$ A/m^2, for optical and electrical stimulation, respectively. Because an universal used, single method is absent, the firing rate is determined according to two methods: the mean spike frequency (MSF) and mean instantaneous frequency (FR_{ISI}) (Van Dijck et al., 2013). The MSF is determined as follows:

$$MSF = \frac{\text{number of spikes} - 1}{t_{n+1} - t_1} = \frac{n}{t_{n+1} - t_1} \tag{4.11}$$

where $t_{n+1} - t_1$ is the time difference between the first and last spike, and n is the number of spike intervals, or thus the amount of spikes minus one. The mean instantaneous frequency is simply:

$$FR_{ISI} = \frac{1}{n} \sum_{i=1}^{n} \frac{1}{I_i} \tag{4.12}$$

where I_i is the inter-spike interval (ISI).

Secondly, the strength-duration curves (SD curves) are determined for both stimulation types. The STN is a spontaneous firing neuron. Consequently, the threshold needs to be adjusted from the minimum electrical (A/m^2) and optical (W/m^2) strength, for a given stimulus duration (s), required to evoke an AP to the minimum strength for the generation of an AP within a predefined period. Again, first a big dataset is generated with the following pulse durations, $[5 \cdot logspace(-5, 0, 51)]$ s, and pulse amplitudes, $[logspace(-3, 0, 31)]$ A/m^2 and $[logspace(0, 4, 41)]$ W/m^2 for electrical and optical stimulation, respectively. The initial conditions are set to the output of a 1 s stimulation free simulation. Next, the delay between pulse onset and AP generation is determined, namely, the time when the membrane potential crosses the -20 mV threshold. Then, for each pulse duration, the minimum strength, which results in a delay lower than the predefined threshold and for which subsequent strengths are lower as well,

is determined. This ensures that the lower limit is found, i.e. for any higher pulse amplitude the delay will be lower than the threshold. Finally, both an analytic and iterative method are used, to find the strength that gives the exact, wanted delay. In case of the analytic method, the *fzero* function available in MatlabR2017a is applied on the, with *nakeinterp1* interpolated and shifted with the wanted value, delay dataset. After the SD curves are determined, these are fit with the *Hill-Lapicque* (Williams and Entcheva, 2015) equation:

$$S_{th}(PD) = \frac{S_{rheo}}{1 - \exp(-\frac{PD}{\tau_{chron}/\ln(2)})} \tag{4.13}$$

with PD the pulse duration, S_{th} the threshold strength, S_{rheo} the rheobase and τ_{chron} the chronaxie. The fitting process is again performed with the Global Solver Toolbox and with the exact same parameters as described in section 3.3.3

To facilitate the comparison, it is useful to translate the irradiance of the strength-duration curve into the threshold, average stimulating current. Normally, this is obtained as follows:

$$I_{th,avg}(PD) = \frac{1}{PD} \cdot \int_{P_{onset}}^{T_{end}} I_{th}(t)\, dt \tag{4.14}$$

with PD the pulse duration, P_{onset} the pulse onset, T_{end} the time at which the evoked current has diminished and $I_{th}(t)$ the threshold stimulating current, i.e. the transmembrane ChR2 current evoked by the irradiance of the SD curve (Williams and Entcheva, 2015).

However, due to ChR2's non linear voltage dependence, the integration interval needs to be adapted for long pulses in case of fast firing neurons. Therefore, to ensure that the threshold, average stimulating current is not affected by a second spike, the threshold stimulating current is integrated over 13 ms and divided by the minimum between the PD and 13 ms.

Finally, the effect of the stimulation source on the AP waveform is studied. Here, an AP triggered by electrical and optical stimulation are compared. Based on the defined strength-duration curves for a delay with 10 ms, both a non- and overlapping pulse are applied for both stimulation sources. The initial conditions are again set to the output of a one second stimulation free period. The compared AP morphologies are the ones triggered by a 1 ms pulse, with a 1177 W/m^2 and 0.0402 A/m^2 amplitude, and a 20 ms pulse, with both a 104 W/m^2 and 1177 W/m^2, and 0.0074 A/m^2 and 0.0402 A/m^2, amplitude, for optical and electrical stimulation, respectively. The AP onset is defined as an increase of the membrane potential above -20 mV.

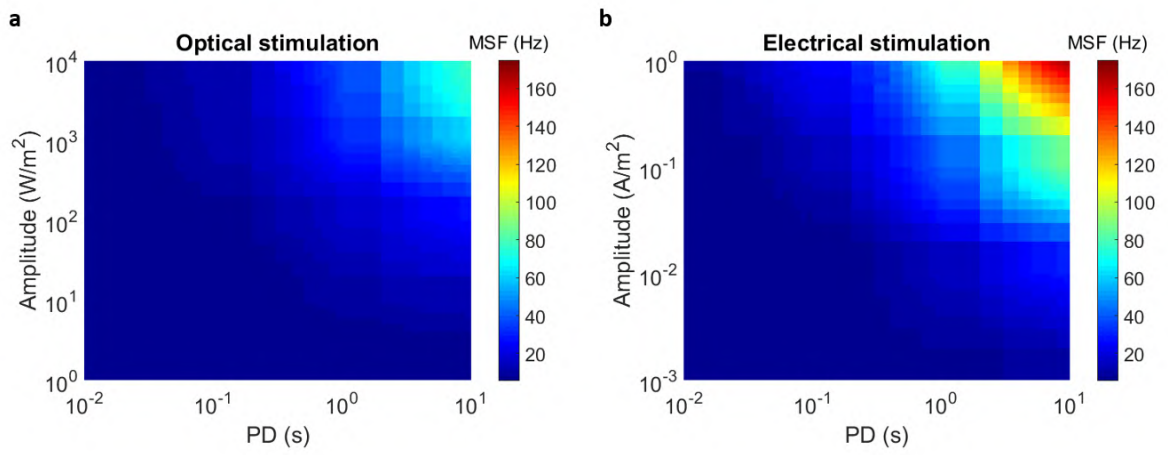

Figure 4.1: Surface plot of the mean spike frequency calculated over the whole simulation as described in section 4.2.1. (a) optical stimulation. (b) electrical stimulation.

4.2.2 Results

Firing rate

For the whole stimulation dataset, as described in section 4.2.1, the mean spike frequency is determined. This is done for two cases: the whole stimulation protocol, i.e. two seconds plus the pulse duration, and only during the pulse itself. The results of the former are visualized in figure 4.1. In stimulation free and resting membrane conditions, the STN is modeled to show rhythmic single-spike activities with a frequency of 4.85 ± 0.18 Hz. With optical stimulation, an increase from 5.13% up to 1523.51% can be obtained. Namely, for a 1 W/m^2, 10 ms pulse, a MSF of 5.10 Hz is obtained, while this is 78.74 Hz for a 10000 W/m^2, 10 s pulse. Furthermore, the maximum MSF evoked by a pulse of 1 ms is 6.74 Hz. The maximum MSF with a pulse amplitude of 1 W/m^2, on the other hand, is 5.47 Hz. In case of electrical stimulation the MSF ranges from 5.48 Hz up to 9.30 Hz and 9.06 Hz up to 175 Hz, for a pulse amplitude of 0.001 A/m^2 and 1 A/m^2, respectively.

More interesting is perhaps the firing rate obtained during the pulse itself. This is because, for small pulses, the MSF determined over the complete stimulation time is dominated by the stimulation free periods. The mean spike frequencies determined during the pulse are depicted in figure 4.2. On average the MSF is much higher. The dark blue area in the lower left corners indicates a MSF of zero. However, this is simply due to the absence of two subsequent spikes during the pulse time. For optical stimulation, a maximum MSF of 95.47 Hz is obtained for a 10000 W/m^2, 0.8 s pulse. On the other hand, a maximum MSF of 230.10 Hz is obtained for a 1 A/m^2, 10 ms electrical pulse.

By comparing optical versus electrical stimulation, it can be denoted that a MSF range match

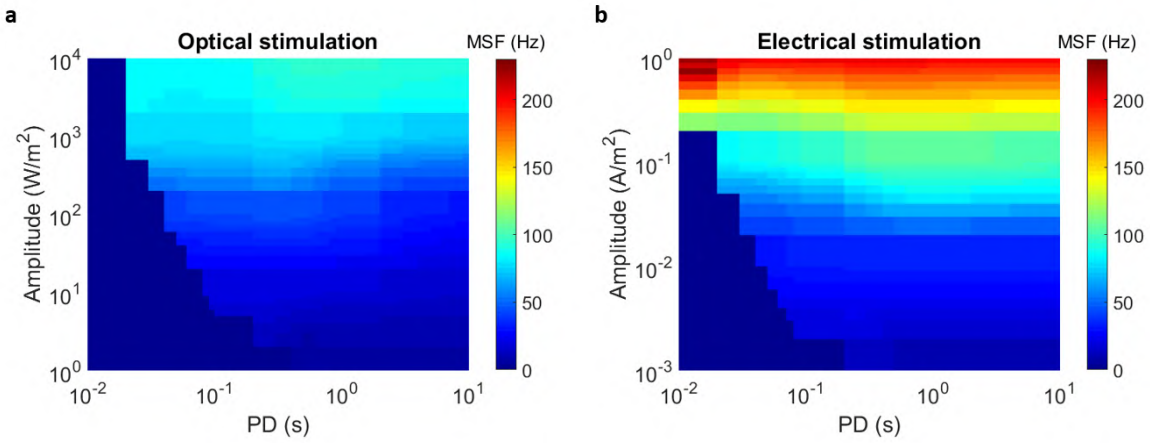

Figure 4.2: Surface plot of the mean spike frequency calculated over the pulse duration as described in section 4.2.1. (a) optical stimulation. (b) electrical stimulation. Dark blue area in the lower left corner indicates the absence of two subsequent APs during the pulse.

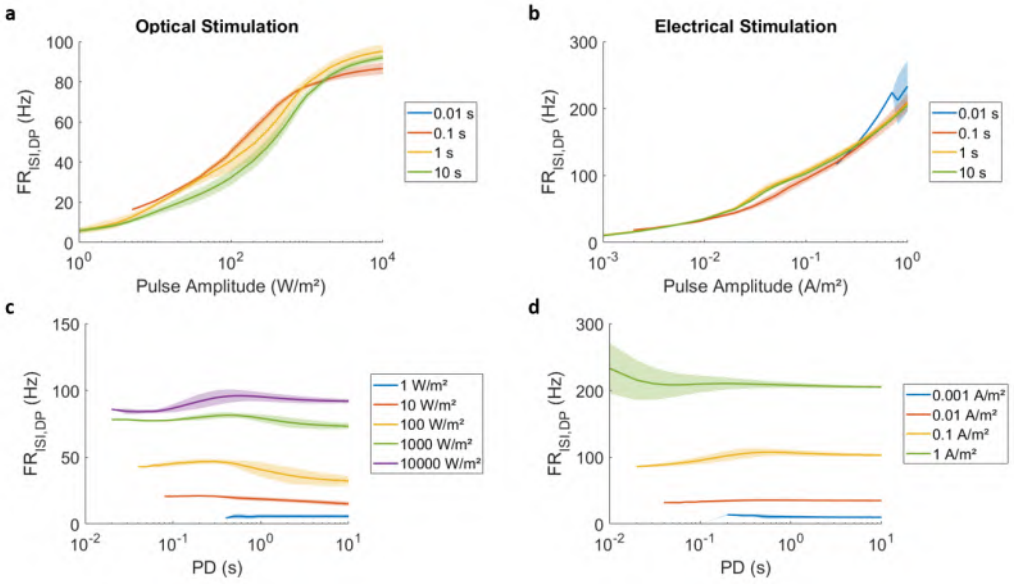

Figure 4.3: AP firing frequency versus pulse amplitude and duration. (a,b) Mean instantaneous frequency ± standard deviation (shaded area) with respect to pulse amplitudes, calculated over pulse duration for optical and electrical stimulation, respectively. (c,d) Mean instantaneous frequency ± standard deviation (shaded area) with respect to pulse duration, calculated over pulse duration for optical and electrical stimulation, respectively.

exists between the complete optical stimulation set and the electrical stimulation for amplitudes up to 0.1 A/m^2. Furthermore, from the comparison of the two figures 4.1 and 4.2, the aforementioned limitation of the mean spike frequency is clearly visible. The firing rate can also be determined by calculating the mean instantaneous frequency (see equation 4.12). In contrast to

the MSF, the estimated firing rate is here dominated by low ISIs. The advantage of the latter is that the standard deviation can be calculated as well, which contains information over possible bursting behavior or spike irregularity.

A comparison of the mean instantaneous frequencies, during pulse ($FR_{ISI,DP}$), for both stimulation sources is depicted in figure 4.3. Subfigures a and b, depict the frequency change in function of the pulse amplitudes. In both cases, the firing rate rises first linearly with pulse amplitude (exponentially on logarithmic scale). However, the firing starts to saturate for optical pulses with amplitudes higher than 1000 W/m^2. This saturation is not observed for electrical stimulation. Furthermore, the absence of a 10 ms graph can be denoted. This is due to the lack of two subsequent spikes during the short pulse.

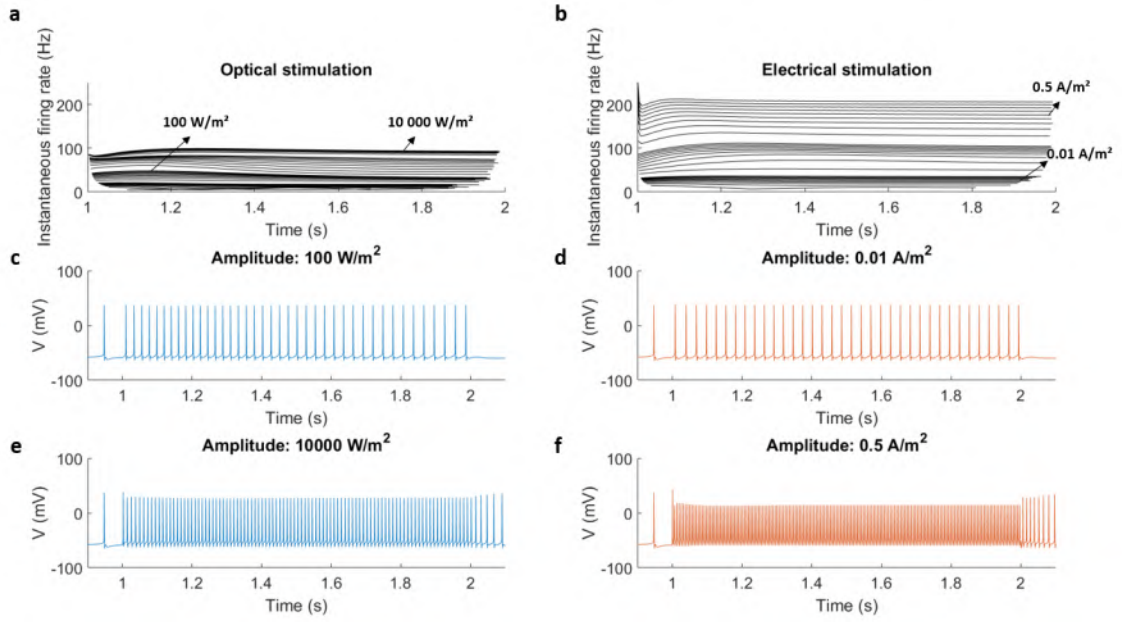

Figure 4.4: The instantaneous firing rate during a 1 s pulse. (a,b) The instantaneous firing rate for the whole amplitude set during a 1 s pulse. (c,e) the membrane potential for optical stimulation with amplitudes 100 W/m^2 and 10000 W/m^2, respectively. (d,f) the membrane potential for electrical stimulation with amplitudes 0.01 A/m^2 and 0.5 A/m^2, respectively.

Except for the saturation, a clear discrepancy concerning the effect of pulse duration can be observed between optical and electrical stimuli. In both cases, first a small increase of the frequency can be denoted between 20 ms and 300 ms pulses. However, this is followed by a constant firing rate in case of electrical stimuli, while there is a drop visible for optical stimulation. Overall, the standard deviation is rather low, indicative for regular spiking behavior. Exceptions are visible at small electrical pulses with high amplitudes. The origin of this variation can be visualized by plotting the instantaneous frequency. This is done for all one second pulses in figure 4.4. Again, the previous denoted observations can be seen, such as the saturation with amplitude

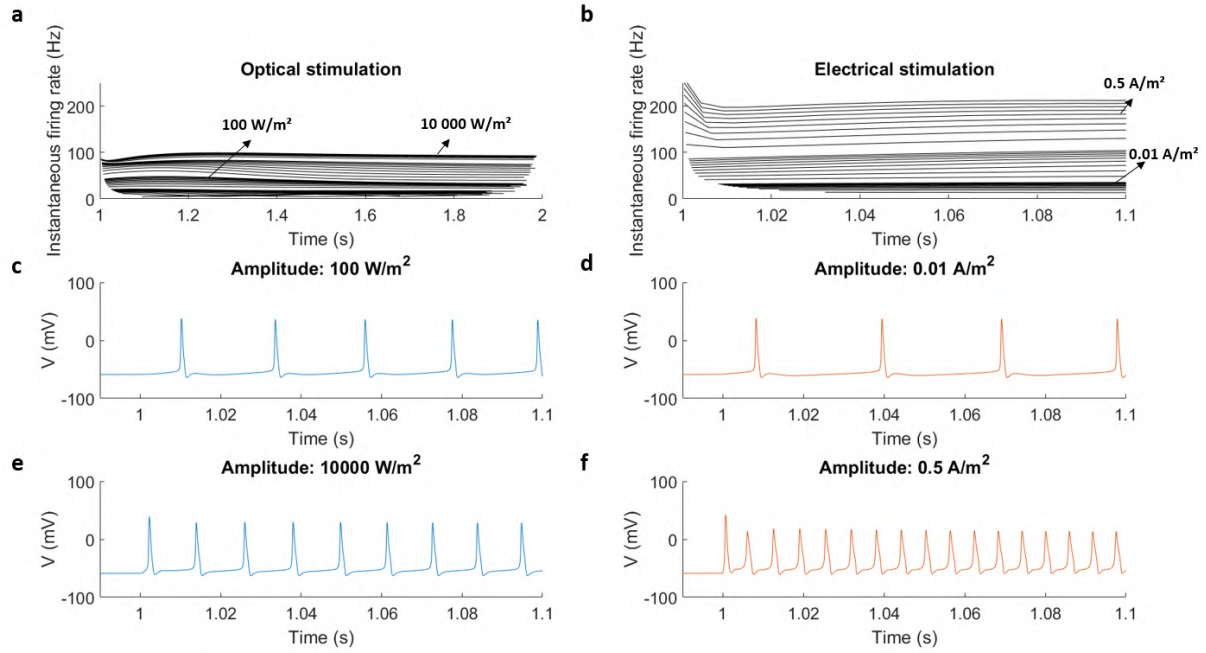

Figure 4.5: The instantaneous firing rate during a 1 s pulse zoomed in on the first 100 ms (a,b) The instantaneous firing rate for the whole amplitude set during a 1 s pulse, for optical and electrical stimulation, respectively. (c,e) the membrane potential for optical stimulation with amplitudes 100 W/m^2 and 10000 W/m^2, respectively. (d,f) the membrane potential for electrical stimulation with amplitudes 0.01 A/m^2 and 0.5 A/m^2, respectively.

and an increase followed by decrease as the time progresses. In case of high electrical pulses, irregularities can be observed at the pulse onset. This is brought into more detail in figure 4.5, which depicts a zoom in on the first 100 ms. In subfigure (f), a discrepancy between the first two and the subsequent APs can be seen. The first AP is directly fired upon pulse onset. Before repolarization is completed, a second AP fires, causing the high initial instantaneous frequency and standard deviation for small pulse durations. Thereafter, the regularity of the system returns. Also notable is the change in AP height. A clear decrease of the height is visible, with increasing pulse amplitude.

Strength-duration curves

An important feature is the delay between pulse onset and AP generation. Figure 4.6 depicts a 3D surface plot of the delay for the dataset described in section 4.2.1. As expected, the delay decreases with increasing pulse amplitude. Furthermore, for a fixed amplitude, the delay-PD curve levels off, when the pulse duration is longer than the latency of the action potential. Hence, no further improvement can be made by prolonging the pulse, as the AP already fired.

By assigning a threshold value, e.g., 10 ms as depicted in figure 4.6, a strength-duration relationship can be determined. The extracted strength-duration curves for a 10 ms threshold

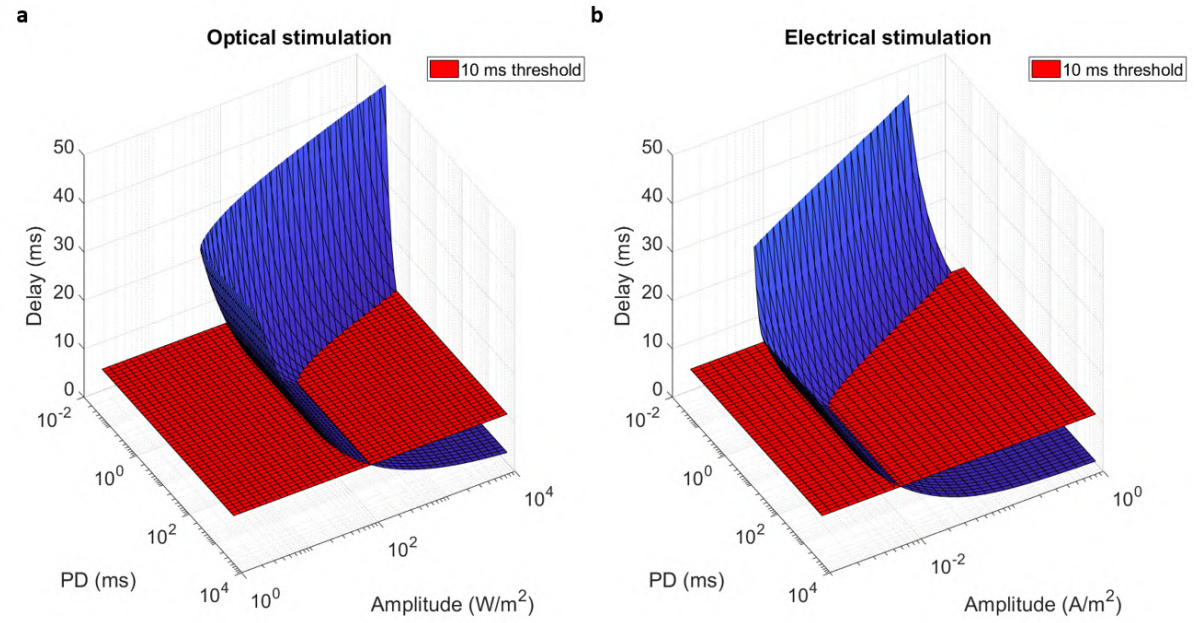

Figure 4.6: 3D surface plot of the AP delay after pulse onset in milliseconds. (a,b) the surface plot for the optical and electrical simulation dataset, respectively, superimposed with the 10 ms threshold

are shown in figure 4.7. As expected, the SD curve extracted from the data itself, is slightly shifted upwards with respect to the optima, determined via analytical and iterative processes. This is due to the selection criterium as described in section 4.2.1. Furthermore, the iterative and analytic determined SD curves coincide. Therefore, for future SD curve determinations, the analytic method will be used, as this is computational less demanding. For both stimulation sources, the rheobase, i.e. the minimum current necessary for excitation with an infinite pulse, can be easily extracted. These are 103.48 W/m^2 and 0.0073 A/m^2 for optical and electrical stimulation, respectively. The chronaxie, i.e. the duration for which the necessary strength is twice the rheobase, could be extracted from the curve as well. However, the extraction of these values are usually done by fitting the Hill-Lapicque equation 4.13. The results of these fits are shown in figure 4.8. An almost perfect fit ($R^2 = 0.9994$) is obtained with the electrical stimulation curve. The rheobase is only slightly lower than aforementioned. The chronaxie is equal to 7.52 ms. For optical stimulation, although the fit of the Hill-Lapicque equation seems good on a linear scale, also with a $R^2 = 0.91$, a poor fit is obtained, which is clearly visible on the logarithmic scale.

The explanation to this can be found in the derivation of the equation. The equation describes the relationship between the duration of a rectangular current pulse and its amplitude (Fozzard and Schoenberg, 1972) for a simple RC membrane model. The irradiance is thus a poor match for the strength. If however, the threshold, averaged stimulation current (see section 4.2.1) is used as strength, an almost perfect fit ($R^2 = 0.9994$) can be obtained as well (see figure 4.9).

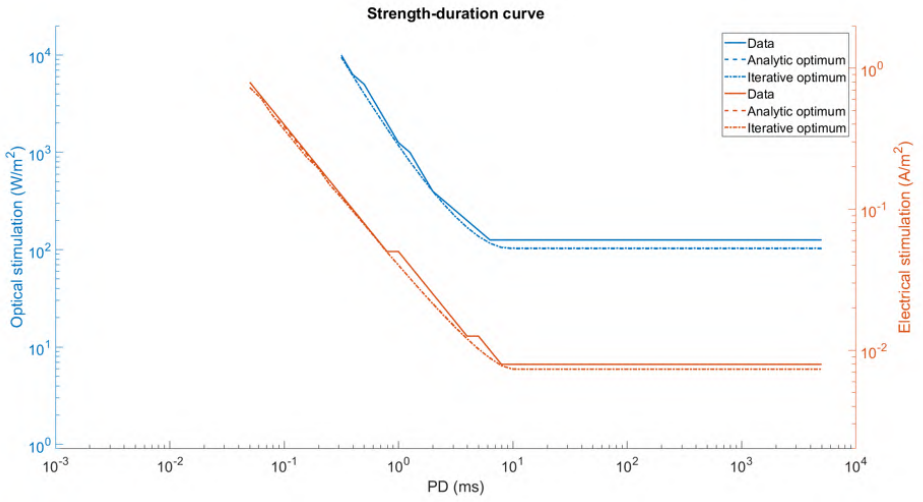

Figure 4.7: The strength-duration curves for a 10 ms delay threshold. The solid lines are the lower limits based on the dataset, described in 4.2.1. The dashed and dashed dotted lines represent the analytic and iterative derived optima, respectively, i.e. the delay is exact 10 ms. The SD curve for optical stimulation is blue and for electrical stimulation orange.

These results reveal a higher rheobase and chronaxie for optical stimulation in comparison with electrical stimulation. Moreover, the optical rheobase, with a value of 0.0124 A/m^2, is almost twice as big (175.21%). However, the difference in chronaxie is only 9.61%. To correlate this back to the applied optical irradiance, a mapping with a three-term power series is performed (Williams and Entcheva, 2015). The result is shown in figure 4.10 (a) with:

$$S_{th}(PD) = b(1) \cdot I_{th,avg}(PD)^{b(2)} - b(3) \tag{4.15}$$

$$= b(1) \cdot \left[\frac{I_{th,avg,rheo}}{1 - \exp(-\frac{PD}{\tau_{chron,I}/\ln(2)})} \right]^{b(2)} - b(3) \tag{4.16}$$

where b represents the power series' coefficients and $I_{th,avg,rheo}$ and $\tau_{chron,I}$, the rheobase and chronaxie, respectively, of the Hill-Lapicque fitted strength-duration curve, with as strength the threshold, average stimulating current. Furthermore, by exploiting this mapping (equation 4.16), an almost excellent fit ($R^2 = 0.9986$) to the original, optical strength-duration curve can be obtained. The rheobase and chronaxie are then derived as follows:

$$S_{th,rheo} = b(1)\,(I_{th,avg,rheo})^{b(2)} - b(3) \tag{4.17}$$

$$\tau_{chron} = -\frac{\tau_{chron,I}}{\ln(2)} \ln\left(1 - \frac{I_{th,avg,rheo}}{[(2\,S_{th,rheo} - b(3))/(b1)]^{1/b(2)}}\right) \tag{4.18}$$

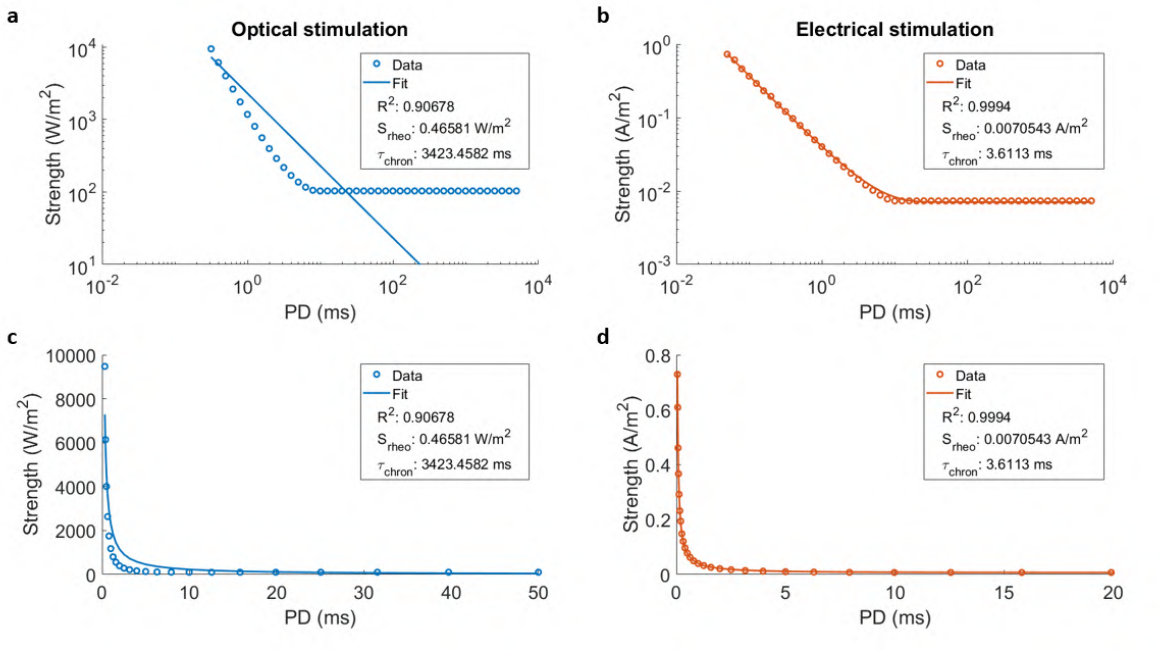

Figure 4.8: The iterative derived strength-duration curves, superimposed with the Hill-Lapicque curve fits. (a,b) logarithmic plots of optical and electrical stimulation, respectively. (c,d) corresponding linear plots

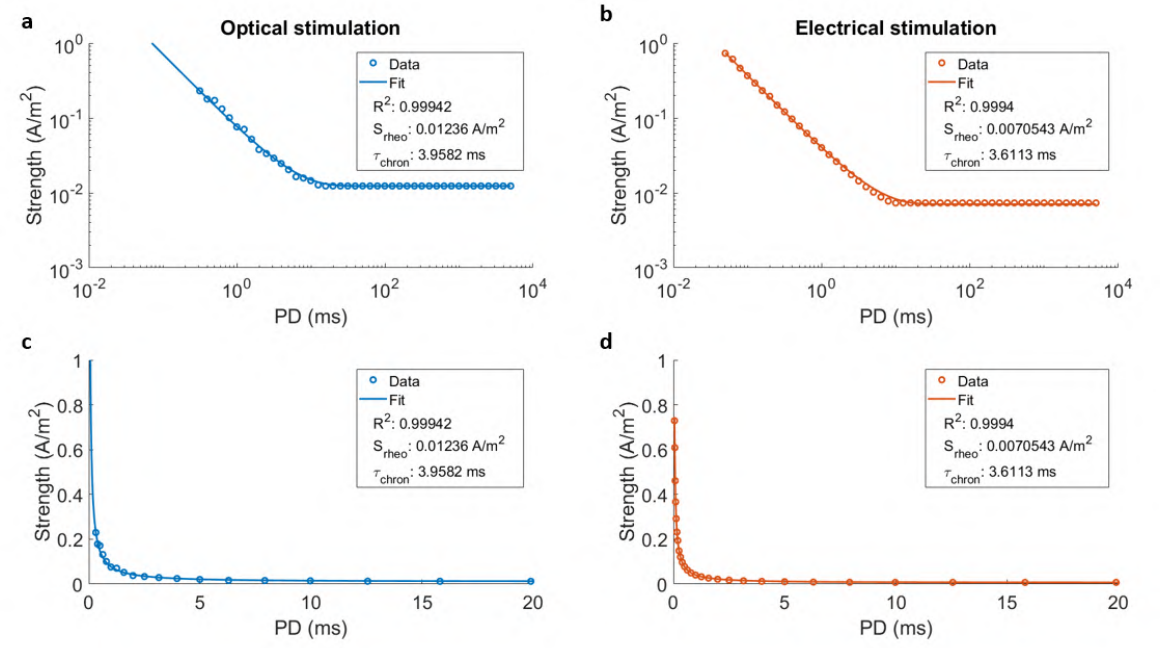

Figure 4.9: The optical and electrical strength-duration curves for a threshold of 10 ms. Instead of the irradiance intensity, the threshold, average stimulating current represents the 'Strength'

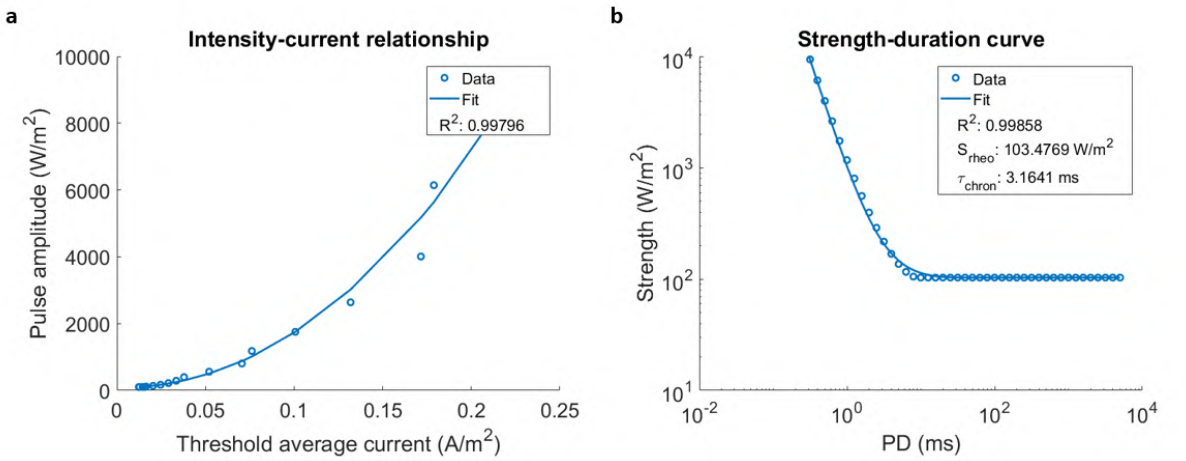

Figure 4.10: Irradiance and threshold, average stimulating current correlation. (a)Empirical mapping of the irradiance to the threshold, average stimulating current. (b) Corrected optical SD curve

Action potential morphology

Figure 4.11 depicts the first action potential generated by three aforementioned (see section 4.2.1) stimulation conditions. Together with the membrane potential, the total transmembrane currents are shown as well. The individual currents are depicted figure A.1. In case of stimulation free conditions, the current responsible for crossing the threshold is the T-type calcium current. After the threshold is reached, the sodium channels are activated. This leads to a depolarizing current one to two orders of magnitude higher than the others. This is followed by the activation of the delay rectifier potassium current. As a result the cell repolarizes, followed by a small hyperpolarization. These two currents are the dominant ones and define the AP waveform. The other currents are smaller and more important for the firing rate than the morphology itself.

The application of an external depolarizing stimulus causes the cell to reach the threshold faster. In case of the 1 ms electrical pulse, a small depolarization is observed. This results in an increase of the depolarizing T-type calcium current and thus faster AP firing. As can be observed in figure 4.11 (g), a 1 ms optical pulse gives rise to a much longer ChR2 current. This is due to the longer deactivation kinetics, as described in section 3.3. However, no clear distinction can be observed between the electrical and optical stimulated AP waveforms. Also for the completely overlapping pulses, no prominent changes are visible.

Figure 4.12 depicts the superimposed AP waveforms of a fixed 20 ms pulse. This, to illustrate the effect of pulse amplitude. The AP peak is slightly increased when higher pulses are applied. Also the hyperpolarization is affected. At the peak the effect of stimulation source is minimal. This is because the differences are compensated by the T-type calcium current. The reason for the more prominent effect on the hyperpolarization part is clearly visible in figure A.1 (o). At

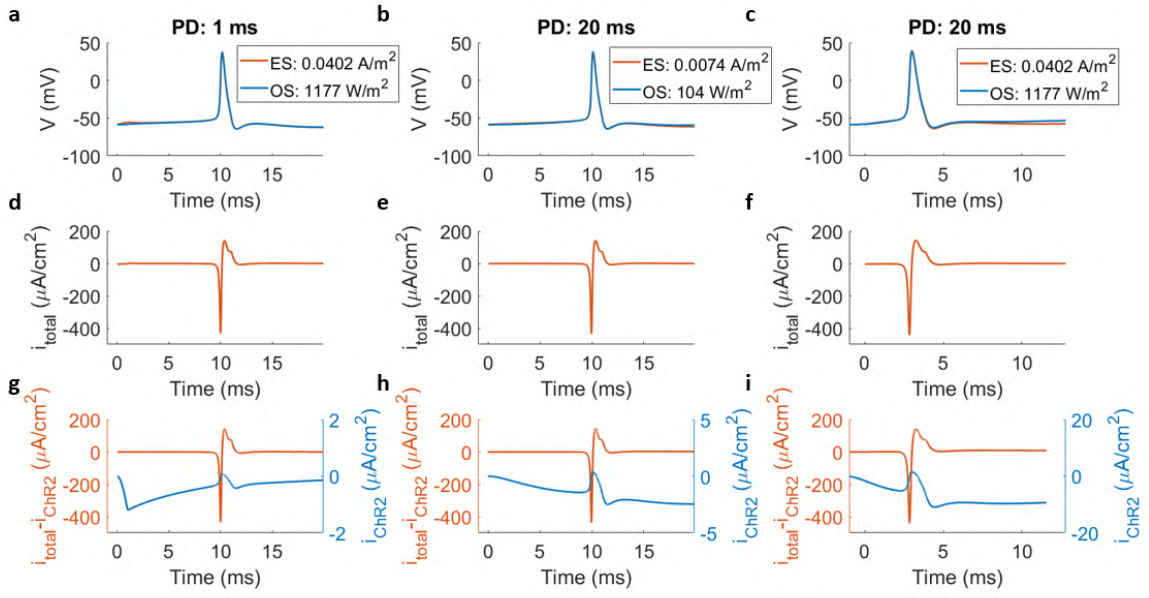

Figure 4.11: Comparison of a single action potential evoked by electrical and optical stimulation with specified conditions. (a-c) a single AP, with the optical AP shifted to match the time at which the -20 mV threshold is passed. (d-f) the total transmembrane current in case of electrical stimulation. (g-i) the total transmembrane current in case of optical stimulation, separated into two parts.

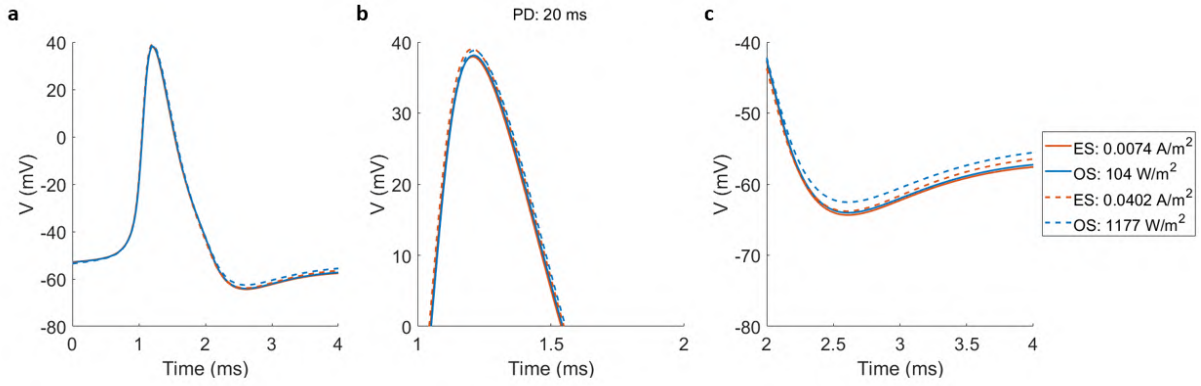

Figure 4.12: The effect of pulse amplitude, by comparing a single action potential evoked by electrical and optical stimulation of 20 ms. (a) a single AP. (b) zoom on the peak of the same AP. (c) zoom of the hyperpolarization. The APs are shifted to match the time at which the -20 mV threshold is passed

these pulse amplitudes, the stimulating current increases an order of magnitude. Therefore, their effects aren't negligible anymore on the AP morphology. Figure 4.13 illustrates the difference between an non- and overlapping pulse. It is clear that small pulses do not affect the morphology. Again for overlapping pulses, the aforementioned effects can be observed.

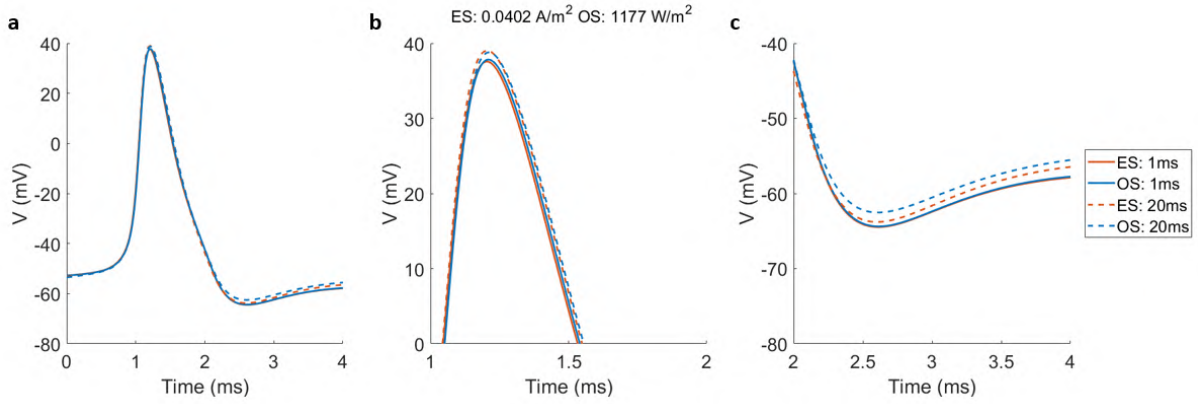

Figure 4.13: The effect of pulse duration, by comparing a single action potential evoked by electrical and optical stimulation of 0.0402 A/m^2 and 1177 W/m^2, respectively. (a) a single AP. (b) zoom on the peak of the same AP. (c) zoom on the hyperpolarization. The APs are shifted to match the time at which the -20 mV threshold is passed

4.2.3 Discussion

Not being limited by electrochemical reactions, optogenetics is an ideal source for constant and prolonged stimulation. For comparative reasons, the effect of continuous electrical pulses were investigated as well, even though electrical stimulation is usually in brief pulses. The results above show a lot of similarities between electrical and optical stimulation, such as the linear dependence for low amplitudes and pulse durations up to 300 ms. Furthermore, figure 4.2 depicts that the same frequency range can be obtained with optical stimulation as with electrical up to 0.1 A/m^2. Moreover, the spiking behavior is highly regular, with only small fluctuations with stimulus onset.

Figures 4.4 and 4.5 display an increase of the instantaneous frequencies followed by steady pacing. However, in case of optical stimulation this is followed by a small decrease in firing rate. The initial increase can be devoted to the neuron physiology itself. This can be concluded by comparing figures A.2 and A.3. Here, a stimulation source independent adaption of the transmembrane currents is observed. The increase in firing rate is caused by the strong increase of the depolarizing L-type calcium current. Nevertheless, there exist a discrepancy between the two stimulation sources. Namely, in case of optical stimulation, the frequency decreases. This is due to the inactivation of the ChR2 channels, as can be seen in figure 4.14. Upon optical stimulation, the ChR2 channels open, rendering them in the highly conductive O_1 state.

Inherent to the channels, they then partly inactivate (see section 3.3), resulting in a decrease of the depolarizing current. However, this inactivation is dependent on the intensity of the used stimulus, which is clearly visible in figures 4.14 (a-d). This explains why the decrease in frequency is more prominent for pulse amplitudes between 100 W/m^2 and 1000 W/m^2.

In section 3.3, the voltage dependence of ChR2 was described. This is clearly visible in figure 4.14, as the current varies with the AP. Also, the rectification can be observed, with extremely lower positive than negative currents. Moreover, although the state occupation is voltage dependent as well, the high voltage change due to the action potential seems not to affect the ChR2 photocycle. Finally, the linear frequency increase followed by saturation, are caused by the ChR2 currents too, which can be seen in figure 4.14. Therefore, there can be concluded that this combination, gives rise to a ChR2 limited firing rate. This is supported by the fact that higher frequencies can be obtained with electrical stimulation. However, electrical pulses with amplitudes between 0.1 A/m^2 and 1 A/m^2, give also rise to increased irregularity and even small bursting. Furthermore, it must be kept in mind that electrical stimulation is modeled as a rectangular pulse, with an infinite rising rate, which is an idealization of the reality.

Similar effects, concerning the strength-duration curves, are observed for both optical and electrical stimulation. Both pulse duration and amplitude cause the delay to decrease, with the former up to the pulse length of the delay itself. Extraction of the strength-duration curves, gave therefore rise to similar trends. However, a poor fit was obtained with the Hill-Lapicque equation on the, by irradiance defined, strength-duration curve. The reason for this, is the assumptions made upon derivation of the equation. By replacing the irradiance by the threshold average stimulating current, an almost perfect fit was obtained just like in case of electrical stimulation. This enables the direct comparison of the charge needed to excite. The rheobase of optical stimulation is almost twice (175.21%) the electrical rheobase (0.01236 A/m^2 vs. 0.0070543 A/m^2). Moreover, the chronaxie is higher as well (9.61%). Therefore, there exists no pulse duration for which both stimulation sources are equally efficient. Hence, electrical stimulation is more efficient for all pulses. The underlying reason, is the dynamic i_{ChR2} waveform. Whereas, the electrical rectangular pulse has an infinite rising rate, the light-triggered activation of ChR2 is a kinetic process with a time constant $>$ 1 ms (in case of the H134R mutant) (Williams and Entcheva, 2015). Consequently a greater optical pulse amplitude compared to electrical stimulation is required.

Concerning the action potential morphology, no major differences between the two stimulation sources could be observed, except for the hyperpolarization with high amplitude overlapping pulses. Also the underlying currents were unaffected, except for a slight change in T-type calcium current. Due to the slow off kinetics ($\sim$20 ms) of the ChR2 channels, the indistinguishable difference between small optical and electrical pulses is rather unexpected. However, this is due to the neglectable current in comparison with the dominating sodium and delayed rectifier potassium currents. Nevertheless, if longer pulses with higher amplitudes are used, the expected

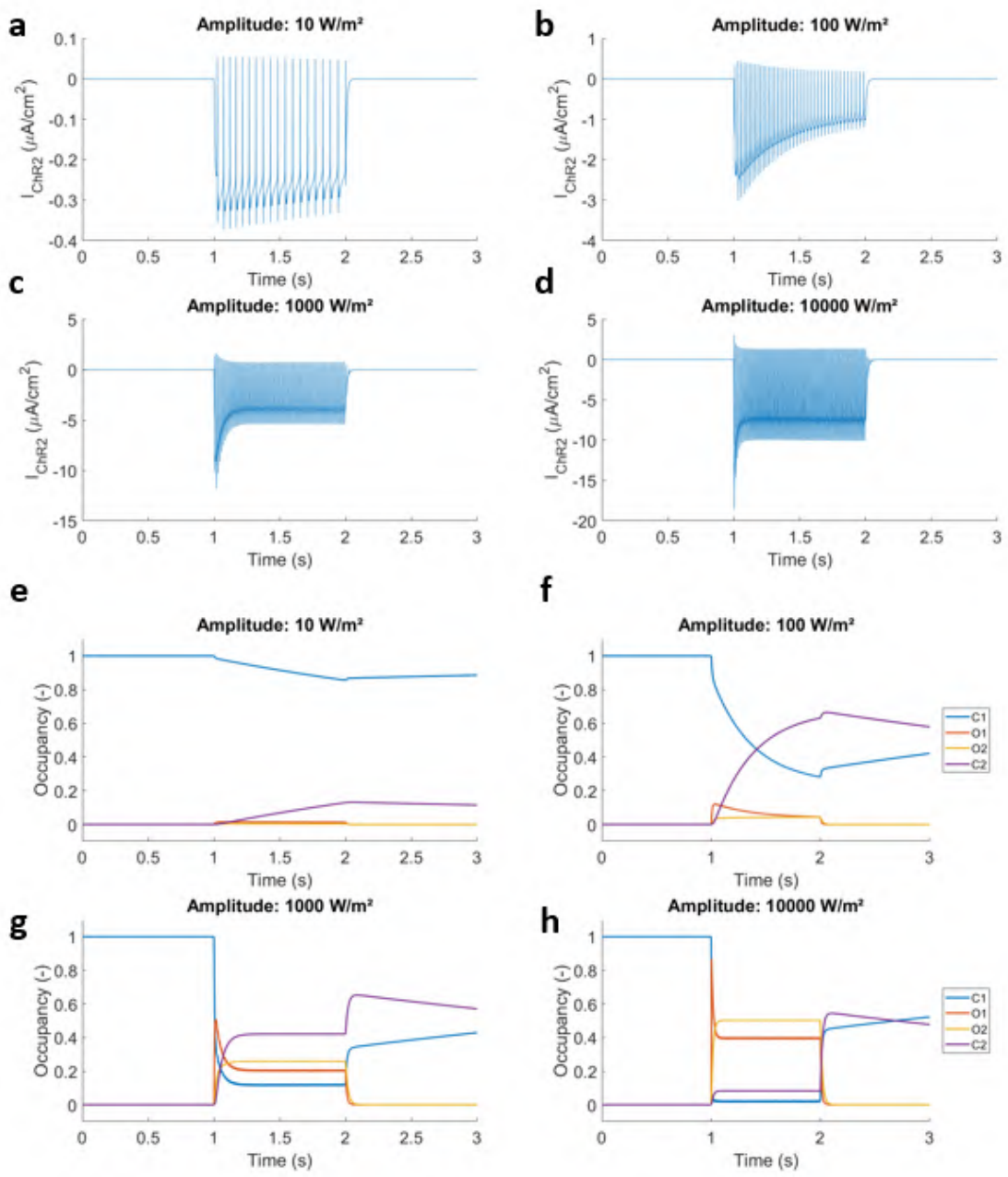

Figure 4.14: The ChR2 current and states for a one second pulse with specified amplitude. (a-d) the ChR2 currents. (e-h) the corresponding state occupancies.

difference can be observed, as the ChR2 current renders no longer negligible. In comparison with APs in heart cells, the effect however is rather small (Williams and Entcheva, 2015), but this can be devoted to the difference in duration of the action potential.

From these results, electrical stimulation seems to be the superior stimulation source. However, the model compares only the effect on the cellular level. For instance, to conduct a complete

efficiency study, the attenuation of the stimulation sources through the tissue needs to be accounted for. Therefore, a model at the organ-level is needed (Abilez et al., 2011, Boyle et al., 2013, Williams and Entcheva, 2015). This will in turn, affect the electrical pulse, which is idealized here as a rectangular pulse. Consequently, no absolute conclusions can be drawn jet. Interesting to see, however, is that more or less the same behavior can be reached with constant optical stimulation in terms of frequency. This is clearly an advantage, as electrical stimulation is limited by electrochemical reactions. Finally, the H134R mutant is a highly sensitive but slow variant. Its slow on and off kinetics are rather negative factors concerning charge efficiency. Better variants are ChETAs, Chronos and ChIEF, which contain faster kinetics. However, this is from the point of view for one AP. If the firing rate needs to be modulated for longer terms, a slower kinetic opsin, such as the H134R, L132C-T159C, or even SFOs (C128S) could be a better choice (see section 1.1.1)(Schneider et al., 2015).

Chapter 5

Locus Coeruleus

The locus coeruleus (LC), located in the pons, is one of the most dominant noradrenergic systems in the brain, that supplies the central nervous system with norepinephrine through widespread efferent projections. Consequently, it plays an important role in sleep to wake transition, attention and feeding behavior (Berridge and Waterhouse, 2003, Purves et al., 2004). Furthermore, studies have shown that the locus coeruleus is correlated to the anticonvulsive action of vagus nerve stimulation (VNS) (Raedt et al., 2011). The underlying mechanisms of VNS and the LC are, however, not fully understood yet. Therefore, it would be interesting to develop an accurate model, such that *in silico* investigations can be performed.

In this final chapter, a network independent LC neuron model is derived from the work of Carter et al. (2012) and fitted with experimental data. First, the basis model is described together with the implementation in MatlabR2017a and applied modifications. Subsequently, the tonic firing rate, pinch response and optogenetic responses are extracted from recordings in rats performed by the Laboratory for Clinical and Experimental Neurophysiology at the university of Ghent. This data is then used to fit and validate the model.

5.1 Locus coeruleus model

For investigation of the sleep-to-wake transition, Carter et al. (2012) derived a conductance-based model of the locus coeruleus and hypocretin (Hcrt) neurons. The neurons are modeled according to the Rall-model (Feng, 2004), consisting of two electrotonically compact compartments. The LC neuron model, used in this dissertation, is adapted from their work. The membrane potential, differential equation for both compartments, the axon and soma, is depicted below.

$$c_A \frac{dV_A}{dt} = -i_{l,A} - i_{Na} - i_K - i_{Ca-K} - i_{AS} \tag{5.1}$$

$$c_S \frac{dV_S}{dt} = -i_{l,S} - i_T - i_h - i_A - i_{Ca} - i_{ChR2} - i_{SA} + i_{inter,neuron} \tag{5.2}$$

The included transmembrane currents are: a sodium current (i_{Na}), a delayed rectifier potassium current (i_K), a calcium dependent potassium current (i_{Ca-K}), a T-type calcium current (i_T), Goldman-Hodgkin-Katz calcium current (i_{Ca}), a low-threshold potassium current (i_h), an A-type potassium current (i_A), a leakage current for both compartments ($i_{l,A}$ and $i_{l,S}$), two compartment connecting currents (i_{AS} and i_{SA}) and a set of inter neuron currents ($i_{inter,neuron}$). Most of the currents are of the Hodgkin Huxley type as described in section 2.3, except the calcium currents (i_{Ca} and i_T), which are according to the Goldman-Hodgkin-Katz formula.

$$i_{Na} = g_{Na}\, m_{Na}^2\, n_{Na}\, (V_A - E_{Na}) \tag{5.3}$$

$$i_K = g_K\, h_K\, (V_A - E_K) \tag{5.4}$$

$$i_{Ca-K} = g_{Ca-K}\, h_{Ca-K}\, (V_A - E_K) \tag{5.5}$$

$$i_T = g_T\, I_t\, n_t\, \frac{V_S}{1 - \exp(2\, V_S/24.42)} \tag{5.6}$$

$$i_{Ca} = g_{Ca}\, I_{Ca}^3\, \frac{V_S}{1 - \exp(2\, V_S/24.42)} \tag{5.7}$$

$$i_h = g_h\, n_h\, (V_S - E_K) \tag{5.8}$$

$$i_A = g_A\, h_A\, (V_S - E_K) \tag{5.9}$$

$$i_{l,A} = g_{l,A}\, (V_A - E_l) \tag{5.10}$$

$$i_{l,S} = g_{l,S}\, (V_S - E_l) \tag{5.11}$$

$$i_{AS} = g_{AS}\, (V_A - V_S) \tag{5.12}$$

$$i_{SA} = g_{SA}\, (V_S - V_A) \tag{5.13}$$

To gain insight on the effects of Hcrt stimulation on the LC circuitry, Carter et al. (2012) built a network of multiple interconnected Hcrt and LC neurons. The accounted inter neuron

currents to the LC are AMPA synaptic currents from Hcrt and LC neurons ($i^{AMPA,LC}$) and Hcrt neurotransmitter based currents, itself ($i^{HCRT,LC}$).

$$i_{inter,neuron} = i^{AMPA,LC} + i^{HCRT,LC} \tag{5.14}$$

with

$$\begin{aligned} i_j^{AMPA,LC} = &\sum_{i=1}^{N_{HCRT}} \left(g_{j,i}^{AMPA,HCRT}\, r_i^{HCRT}\, (V_{S,j} - 0\,mV)\right) \\ &+ \sum_{i=1}^{N_{LC}} \left(g_{j,i}^{AMPA,LC}\, r_i^{LC}\, (V_{S,j} - 0\,mV)\right) \end{aligned} \tag{5.15}$$

$$i_j^{HCRT,LC} = \sum_{i=1}^{N_{HCRT}} \left(g_{j,i}^{HCRT,LC}\, s_i^{HCRT}\right) \tag{5.16}$$

where N_{HCRT} is the number of Hcrt neurons; $g_{j,i}^{AMPA,HCRT}$ and $g_{j,i}^{AMPA,LC}$ are the maximal AMPA conductance from Hcrt and LC neuron i, to LC neuron j; r_i^{HCRT} and r_i^{LC} are the neuron transmitter release from Hcrt and LC neuron i, respectively; N_{LC} is the number of LC neurons; $g_{j,i}^{HCRT,LC}$ and s_i^{HCRT} are the maximal Hcrt neurotransmitter based conductance and neurotransmitter release, respectively. However, in this master dissertation, only the effect of optogenetic stimulation is of importance. Hence, no network is implemented and the inter neuron currents are modeled by a simple continuous depolarizing current.

In their model, Carter et al. (2012) also implemented a ChR2 current. As they used a SFO (ChR2(C128S)) in their experiments and were only interested in the slow dynamics, they adopted a simple two state model with voltage and irradiance independent kinetics (equation 5.17).

$$i_{ChR2,SFO} = g_{ChR2,SFO}\, h_{ChR2,SFO}\, (V_S - E_{ChR2}) \tag{5.17}$$

The gate rate equations are either expressed with opening (α_w) and closing rate (β_w) (equation 5.18) or with a steady-state function (w_∞) and time constant (τ_w) (equation 5.19, see also section 2.3)

$$\frac{dw}{dt} = \alpha_w(V)\,(1 - w) - \beta_w(V)\, w \tag{5.18}$$

or

$$\frac{dw}{dt} = \frac{w_\infty(V) - w}{\tau_w(V)} \tag{5.19}$$

were w stands for the gating variables, with m_{Na}, n_{Na}, h_K, h_{Ca-K} and $h_{ChR2,SFO}$ according to equation 5.18, and I_t, n_t, I_{Ca}, n_h and h_A according to equation 5.19. The individual gate rate functions are summarized in table 5.1, where they are depicted in SI units.

Due to the calcium currents, the intracellular calcium concentration can again not be modeled

as constant. Carter et al. (2012) models the calcium dynamics as follows:

$$\frac{d[Ca]_i}{dt} = -0.35 \cdot i_{[Ca]} - \mu^2([Ca]_i - [Ca]_{i,0}) \tag{5.20}$$

wit $i_{[Ca]}$ the sum of all calcium currents, i.e. i_{Ca} and i_T; μ^2 the inverse calcium decay time constant and $[Ca]_{i,0}$ the intracellular calcium concentration at rest.

Table 5.1: Rate functions of LC-model derived by Carter et al. (2012), in SI units (except V, which is in mV)

Gating variable	**Opening rate (α_w) / Steady-state function (w_∞)**	**Closing rate (β_w) / Time constant (τ_w)**
m_{Na}	$-320 \cdot \frac{V_A - V_t - 18}{\exp(\frac{V_A - V_t - 18}{-4}) - 1}$	$280 \cdot \frac{V_A - V_t - 40}{\exp(\frac{V_A - V_t - 40}{5}) - 1}$
n_{Na}	$128 \cdot \exp(\frac{V_A - V_t - 17}{-18})$	$\frac{4000}{1 + \exp(\frac{V_A - V_t - 40}{-5})}$
h_K	$-16 \cdot \frac{V_A - V_t - 35}{\exp(\frac{V_A - V_t - 35}{-5}) - 1}$	$250 \cdot \exp(\frac{V_A - V_t - 20}{-40})$
h_{Ca-K}	$\frac{40}{1 + \exp(\frac{0.08 - [Ca]^*}{0.014})}$	-20
I_t	$\frac{1}{1 + \exp(V_S + 80)}$	0.1
n_t	$\frac{1}{1 + \exp(-(V_S + 60))}$	0.015
I_{Ca}	$\frac{1}{1 + \exp(\frac{V_S + 38}{-0.5})}$	0.0025
n_h	$\frac{1}{1 + \exp(\frac{V_S + 80}{10})}$	$10^{-3} \cdot (2 - \frac{1.999}{\exp(-(V_S + 60))})$
h_A	$\frac{1}{1 + \exp(-(V_S + 41))}$	$10^{-3} \cdot (350 - \frac{349}{1 + \exp(\frac{V_S + 47}{4})})$
$h_{ChR2,SFO}$	$400 \cdot I(t)^{**}$	0.01

$^*Ca^{2+}$ *concentration in* μM

$^{**}I(t)$ *equal to 0 or 1, if light off or on, respectively*

5.2 Implementation in MatlabR2017a

A few modifications are made concerning the model reported by Carter et al. (2012). First, as already denoted, no network is implemented. Therefore the inter neuron currents will be modeled as a constant depolarizing transmembrane current. Secondly, the parameters are transferred into specific units. By doing this, the same tolerances and boundaries for the ode solvers can be used as in the previously discussed model. This translation is obtained by setting the specific

Table 5.2: LC-model parameters (Carter et al., 2012).

Definition	**parameter**	**value***	**units***	**value****	**units****
max conductance of Na channel	g_{Na}	260	nS	650	S/m^2
reversal potential Na current	E_{Na}	50	mV	50	mV
max conductance of delayed-rectifier K channel	g_K	80	nS	200	S/m^2
reversal potential K current	E_K	-60	mV	-60	mV
max conductance of Ca activated K channel	g_{Ca-K}	40	nS	100	S/m^2
conductance from soma to axon	g_{AS}	40	nS	100	S/m^2
conductance leakage channels axon	$g_{l,A}$	0.45	nS	1.125	S/m^2
conductance leakage channels soma	$g_{l,S}$	0.9	nS	1.125	S/m^2
reversal potential leakage current	E_l	-60	mV	-60	mV
max conductance of h-type K channel	g_h	1.2	nS	1.5	S/m^2
max conductance of T-type Ca channel	g_T	1.8	nS	2.25	S/m^2
max conductance of GHK Ca channel	g_{Ca}	1.2	nS	2.2	S/m^2
max conductance of A-type K channel	g_A	40	nS	50	S/m^2
max conductance of SFO	g_{SFO}	4	nS	5	S/m^2
reversal potential ChR2 current	E_{ChR2}	0	mV	0	mV
conductance from axon to soma	g_{SA}	40	nS	50	S/m^2
resting membrane potential	V_{m0}	-60	mV	-60	mV
inverse calcium decay time constant	μ^2	0.9^2	1/s	0.9^2	1/s
axon membrane capacitance	c_A	4	pF	0.01	F/m^2
soma membrane capacitance	c_S	8	pF	0.01	F/m^2
specific depth	d	-	-	18507e-9	m
resting intracellular Ca concentration	$[Ca]_{i,0}$	0.04	μM	0.04	μM
threshold potential	V_T	-57	mV	-57	mV

* *Values by* Carter et al. (2012)

** *implemented Values*

capacitances (c_A and c_S) equal to 0.01 F/m^2. Hence, an estimated surface value can be obtained for both compartments, i.e. $4e{-}10$ m^2 and $8e{-}10$ m^2 for the axon and soma compartment, respectively. Consequently, the specific values can be calculated by dividing the parameters, reported by Carter et al. (2012), by their compartment estimated surface value. Both values, denoted by Carter et al. (2012) and translated, are depicted in table 5.2.

The specific depth was derived from equation 5.20. The 0.35 term is the conversion factor from pA to μM/s. Hence, this term should be equal to:

$$\frac{1}{z\,F\,d\,A} \tag{5.21}$$

with F the Faraday constant, z the valence of calcium ions, d the specific depth and A the surface area. By solving this equation to d and using the derived surface area of the soma (8e-10 m^2), a value of 18.5 μm is obtained, which represents the combined effects of intracellular calcium buffering mechanisms and cellular geometry (Hahn and McIntyre, 2010).

Due to the inability of producing sufficient high frequency spiking, the model was further simplified into one compartment model. This was obtained by setting V_A and V_S in equations 5.1 and 5.2 equal to the same value V followed by summation of the two compartments. The resulting differential equation of the one compartment is thus:

$$c_m \frac{dV}{dt} = 0.5 \cdot (-2 \cdot i_l - i_{Na} - i_K - i_{Ca-K} - i_T - i_h - i_A - i_{Ca} - i_{ChR2}) \tag{5.22}$$

with c_m the specific membrane capacitance equal to 0.01 F/m^2.

5.3 Experimental data

To validate the optorespons of the LC model, the simulations are compared with experimental data extracted from rat brains by the Laboratory for Clinical and Experimental Neurophysiology (LCEN3) at the university of Ghent. This data is used for two purposes, the aforementioned, but also fitting of the simplified inter neuron stimulus. In this thesis, the data of only one rat model is used.

5.3.1 Methods and materials

The genetic material of a ChR2(L132C-T159C) mutant, was expressed by injecting a viral vector, of which the plasmid map is depicted in figure 5.1. A plasmid AAV delivery system is used, containing a PRS2x8 promotor, a SV40 misc intron, the opsin gene and a mCherry reporter. PRS2x8 is a noradrenergic neuron-specific promotor and consists of an eight tandem repeat of transcription factors Phox 2a/2b followed by a human dopamine β-hydroxylase promotor (Wang et al., 2006).

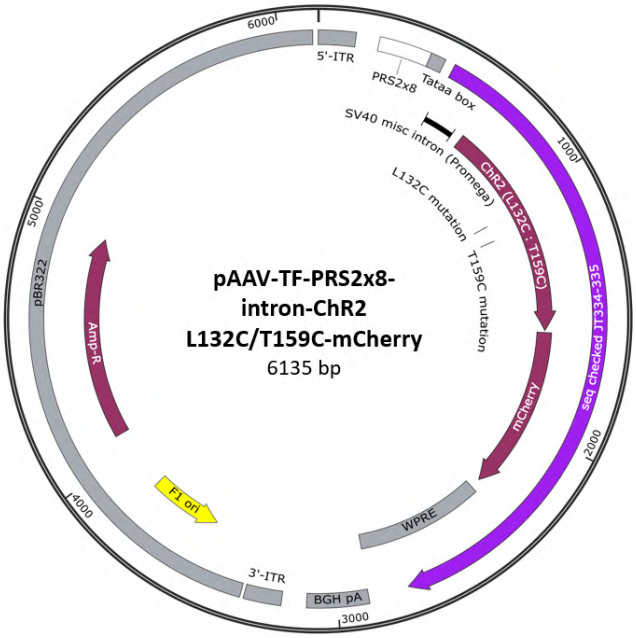

Figure 5.1: Plasmid map of used vector for optogenetic transgene delivery

For both the vector injection and extracellular recordings, the animal was anesthetized and fixated into a stereotactic frame with the head slightly tilted, bregma 2 mm below lambda.

5.3.2 LC localization

The localization of the LC is based on three criteria: its expected location, the waveform with correlated sound and response to contralateral paw pinch. The LC neurons are usually found around 3.9 mm posterior to bregma, 1.15 mm lateral to the midline and 5.2-5.8 mm ventral to the surface of the brain (Bouret et al., 2003). During the dive, the LC can be identified by the typical sound correlated to the frequency and waveform of the action potential. The duration of the action potential is $\geq$ 1 ms and the spontaneous firing rate is between 0.5 Hz and 7 Hz (Hickey et al., 2014). Another specific, although not necessary, characteristic is the biphasic pinch response, with first an increase in frequency followed by a refractory period (Hickey et al., 2014).

5.3.3 Single unit extraction

After the data is recorded, the single units need to be extracted. This is done by using the Spike2 software (Cambridge Electronic Design). Based on multiple spike features, the software is able to classify the data into multiple waveforms. After some modification, three separate waveforms remain, indicative for three different neurons. Classification was already performed online by LCEN3. The three waveforms are depicted in figure 5.2.

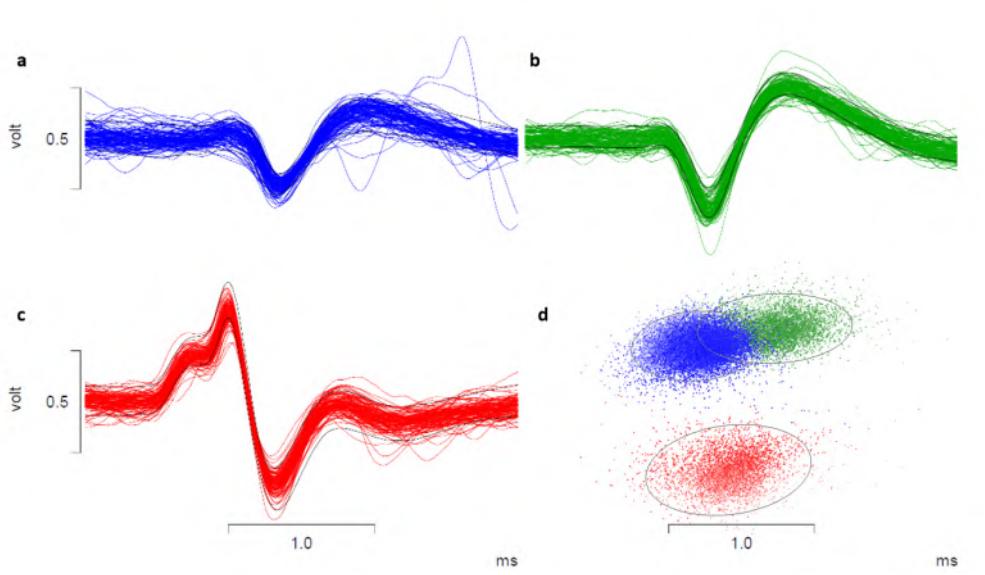

Figure 5.2: Waveform of recorded neurons. (a-c) individual waveforms. (d) principal component analysis

To ensure that the waveform corresponds to a single unit, a principal component analysis can be performed. This is a linear projection of the feature space onto the orthonormal vectors, where the first principal components correspond to the (hyper-)directions along which the data has the highest variance. This is useful to identify separate clusters, as can be seen in figure 5.2 (d). The red waveform is well separated from the other data points, indicative to be originated from a single neuron.

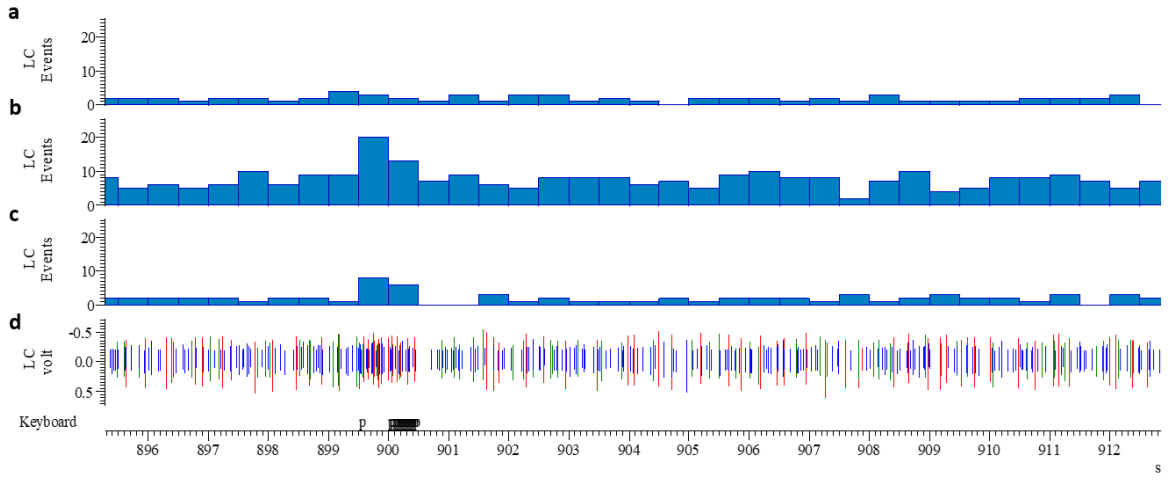

Figure 5.3: Rate of individual neurons with 0.5 s bin width. (a) rate of green neuron. (b) rate of blue neuron. (c) rate of red neuron. (d) all waveforms. Color code is based on figure 5.2

Finally, the pinch response of each neuron is investigated. The firing rate, collected into 0.5 s

bins, of each neuron is depicted in figure 5.3. On the bottom of the figure, the applied stimuli are displayed, where p indicates the pinch. Subfigure (a), corresponding to the green neuron (see figure 5.2), indicates no pinch responsiveness. Subfigures (b) and (c), both indicate pinch responsiveness. Hence, corresponding neurons could represent both an LC neuron. However, the blue neuron has a high baseline firing rate. Therefore, only the data of the red neuron will be further used.

5.4 Results

From the extracted data, a spontaneous firing rate of 3.35±0.49 Hz is determined. This is done by calculating the MSF over regions where no stimulus was present twenty seconds before or ten seconds after, the first or last event, respectively. Based on this value, the required constant depolarizing current is determined for both aforementioned models.

5.4.1 Comparison models

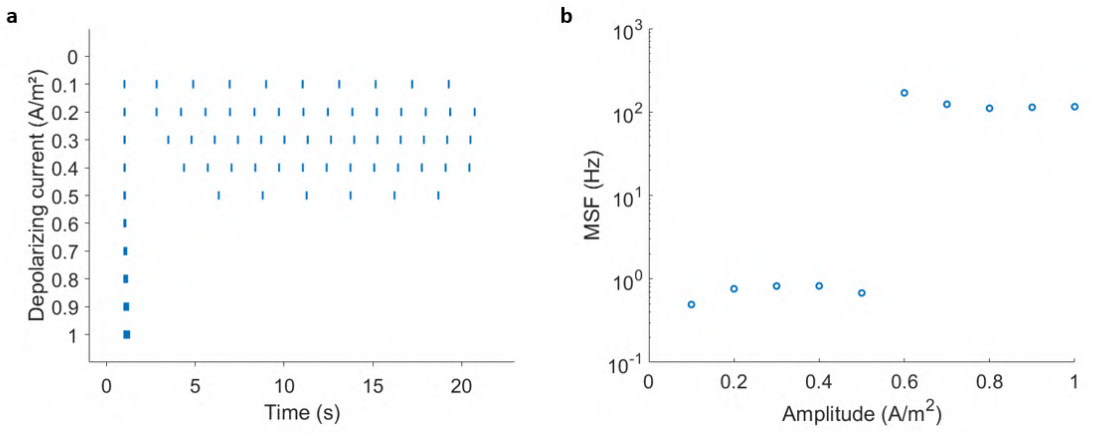

Figure 5.4: Spiking of two compartment model. (a) spike raster plot for varying linear depolarization currents. (b) MSF with respect to amplitude varying linear depolarization currents.

As can be denoted in figure 5.4, it was not possible to reach the required frequency. Subfigure (b), depicts the evolution of the mean spike frequency in function of the amplitude of the depolarization current. At 0.6 A/m^2 a sudden jump in MSF is observed. This is due to the lack of tonic firing after the initial burst with pulse onset. The maximum tonic firing rate achievable with the two compartment model is 0.75 Hz for a current amplitude of 0.4 A/m^2.

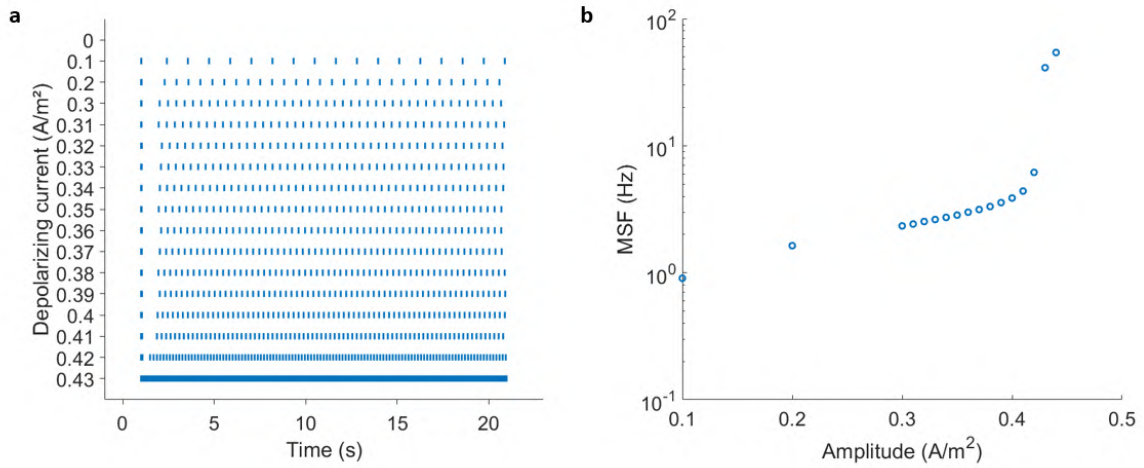

Figure 5.5: Spiking of single compartment model. (a) spike raster plot for varying linear depolarization currents. (b) MSF with respect to amplitude varying linear depolarization currents.

However, with the single compartment model reaching of the required 3.35 Hz tonic firing rate is possible. Again, with current onset, a small burst is observed for each amplitude. However, in contrast with the two compartment model, the tonic firing rate keeps increasing with increasing amplitude without the generation of infinite refractory period. Based on these results, a current amplitude is chosen such that the tonic firing rate matches the measured frequency. Consequently, the constant depolarization current is set to 0.39 A/m^2, which generates a tonic firing rate of 3.34 Hz. Concerning the further obtained results, the initial conditions are set to the output of a 10 s simulation at this constant depolarizing current, without any extra pulse. This to reduce computational time and to ensure that the model has reached an equilibrium, not affected by current onset.

A pressing question is, why is the two compartment model not able to generate the required firing rate. Figure 5.6 depicts the comparison of the action potentials generated by the two models. Several interesting features are visible. There is a more or less constant difference between the soma and axon compartments, until the AP threshold is reached in the axon compartment. Furthermore, although the currents are halved, the APs generated in the single compartment model, contain a higher peak value. Also, after an AP, the membrane potential in the single compartment model matches the potential in the soma, while upon firing it matches to the axon compartment. Consequently, the increased firing rate of the single compartment model is due to the increased repolarization after the AP hyperpolarization phase and not due to lowering of the threshold.

While all state occupancies are in the same order of magnitude for both models, the h_A state occupancy is an order of magnitude higher in case of the two compartment model (see figure 5.7).

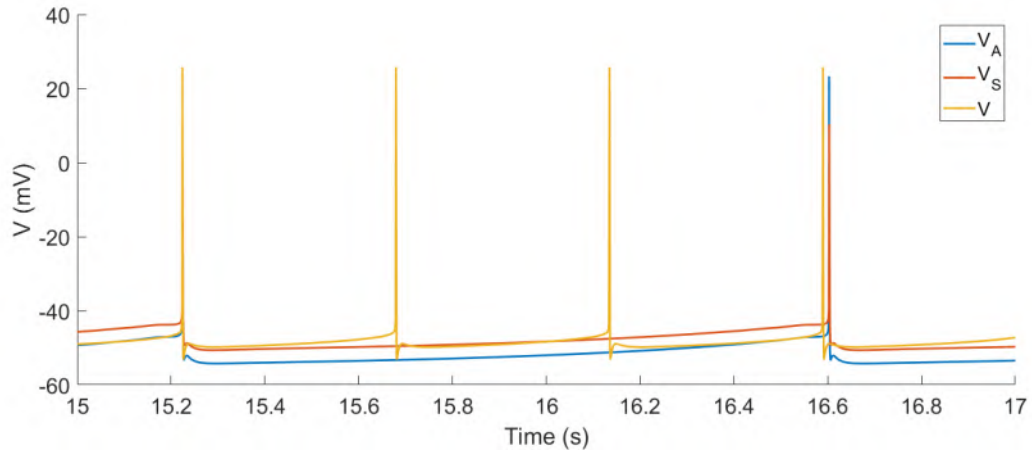

Figure 5.6: Comparison of membrane potentials, with V_A, V_S and V the membrane potentials of the two compartment, axon and soma, and one compartment model, respectively, for a fixed depolarizing current of 0.3 A/m^2. APs of the one compartment model are shifted to match the first AP generated by the two compartment model after 15 s. Zoom in of figure B.1

This gives rise to a high hyperpolarizing current. However, the A-type potassium current is a typical AP shape modifier. This can also be seen in figure 5.7, where the state occupancy, and thus the current (see figures B.2 and B.3), is only increased during the AP. The reason for this increased occupancy is due to the decreased hyperpolarization in the soma compartment. Furthermore there are no notable differences that could cause the different behavior. Therefore, the low firing rate of the two compartment model is solely due to the spatial filtering. In case of the single compartment model, the constant current depolarizes the whole cell, with only small hyperpolarizing currents present. On the other hand, in the two compartment model and after an AP, the membrane potential in the soma is constantly higher than in the axon. Consequently, the constant current depolarizes the soma more slowly, as there is a constant leakage to the axon (see figure 5.6). Furthermore, an AP is only fired when the threshold is reached in the axon, where the fast transient sodium currents are located. However, this is equivalent to a higher threshold in the soma. Hence, the slower depolarization and higher threshold are the causes for the low firing rate in the two compartment model.

5.4.2 Pinch and optical response

Now the model[1] is fitted, the pinch and optical responses can be investigated. During the recordings, three pinch responses were measured, of which the firing events are visualized in figure 5.8. On average, the pinch response resulted in a MSF of 13.64 ± 2.74 Hz and a refractory period of 1.186 ± 0.234 s. This behavior was modeled with the application of an electrical pulse. The result of different pulse amplitudes is shown if figure 5.8 (b). With a pulse of 0.90 s, which is equal to the average pinch during the measurements, at 0.0314 A/m^2, an equivalent MSF and

[1] from now on 'model' refers to the single compartment model, with a constant depolarizing current of 0.39A/m^2

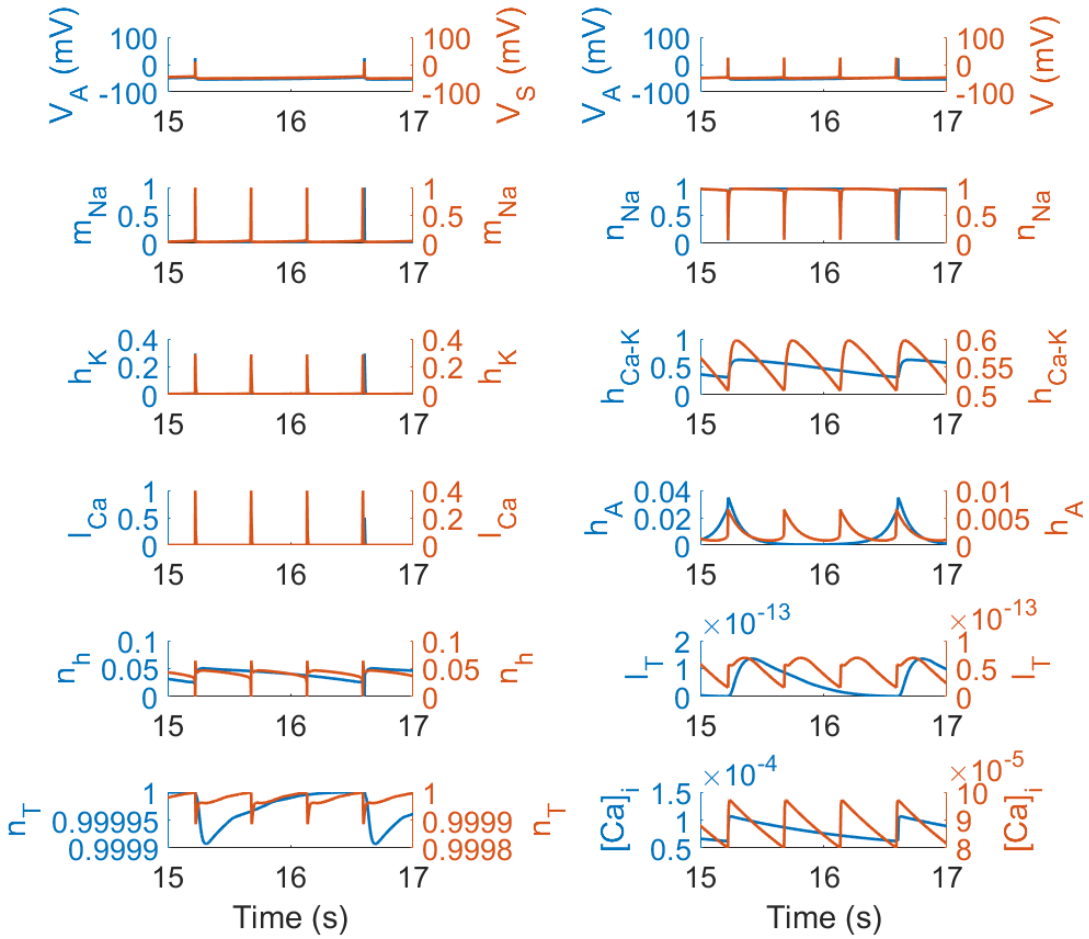

Figure 5.7: Comparison of the state occupancies of single (orange) and two (blue) compartment model for a fixed depolarizing current of 0.3 A/m^2. Same region of interest as in figure 5.6

refractory period of, respectively, 13.68 Hz and 1.09 s, was obtained. A t-test showed for both values a non significant difference with the measured data ($p = 0.98$ and $p = 0.54$, respectively).

In order to compare the optical response, the kinetics of the ChR2 channel needs to be adjusted to the mutant used during the measurements. The used opsin is a ChR2(L132C-T195C) mutant (see section 5.3). This specific mutation increases the sensitivity but decreases its dynamics as well. According to Pan et al. (2014), time constants, τ_{on} and τ_{off} are 127 ± 11 ms and 199 ± 17 ms, respectively. By adjusting the opening and closing rate of the simple two state ChR2(SFO) model (see 5.17 and table 5.1), to $2.87 \cdot I(t)$ and 5, respectively, this behavior is obtained.

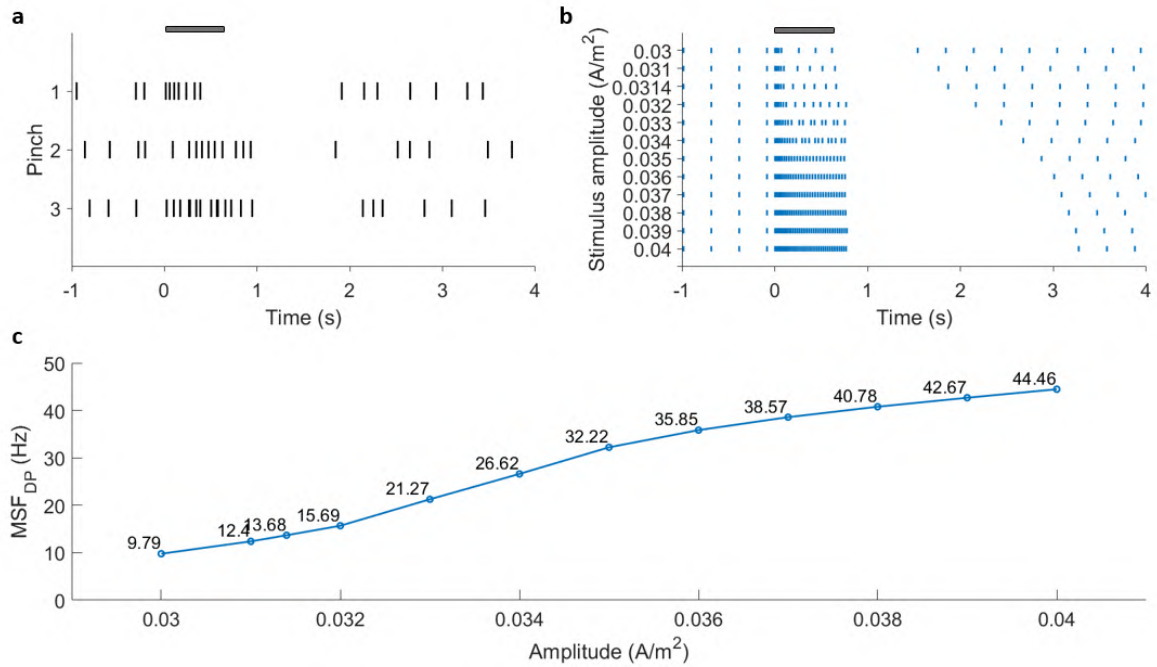

Figure 5.8: Measured and simulated pinch response. (a) measured pinch response for three separate pinches. (b) simulated pinch response for different amplitudes and pulse duration equal to the average of the three measured pinches (0.90 s and indicated with gray bar). (c) the mean spike frequency w.r.t. pulse amplitude.

Next, the maximum ChR2 conductance needs to be fitted. This is based on the measured optical response to 1.49 s laser pulses. To ensure that the behavior was not affected by any previous stimulations, only those with no other stimulus 5 s before or after, are included. This led to a set of thirteen separate responses (see figure 5.9). The average MSF was determined over the pulse duration plus 0.5 s. The resulting value is 5.11 ± 0.35 Hz, which is significantly higher than the tonic firing rate ($p = 4.43e{-}10$). By changing the maximal ChR2 conductance ($g_{ChR2,SFO}$) to 3 S/m^2, a firing rate with MSF of 5.12 Hz can be modeled (see figure 5.9).

To validate the model, simulations of 0.5 s and 0.98 s were compared with measured data. Again, only stimuli with no other stimulus in a 5 s range were included. The extracted AP sets are depicted in figure 5.10. Both stimulation protocols, led to a significant increase ($p = 0.022$ and $p = 8.70e{-}5$) of the firing rate with respect to the tonic frequency. The MSFs are 3.96 ± 0.64 Hz and 4.64 ± 0.74 Hz, for the 0.5 s and 0.98 s pulse, respectively. On the other hand, the model generated a not significantly different MSF ($p = 0.08$) of 3.53 Hz and significantly different MSF ($p = 0.004$) of 3.84 Hz, for the 0.5 s and 0.98 s pulses, respectively.

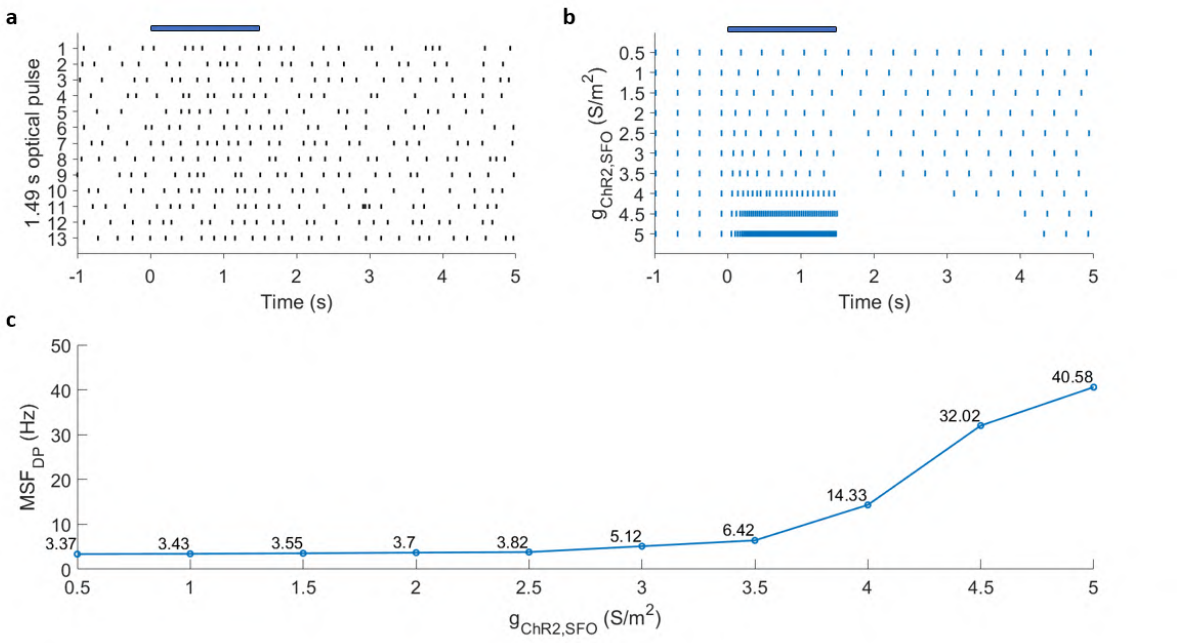

Figure 5.9: Measured and simulated optical response, for an optical pulse of 1.49 s. (a) measured optical response for separate stimulations. (b) simulated optical response for different maximal conductances. (c) the mean spike frequency w.r.t. the maximal conductance of ChR2 ($g_{ChR2,SFO}$). Applied pulse indicated with blue bar

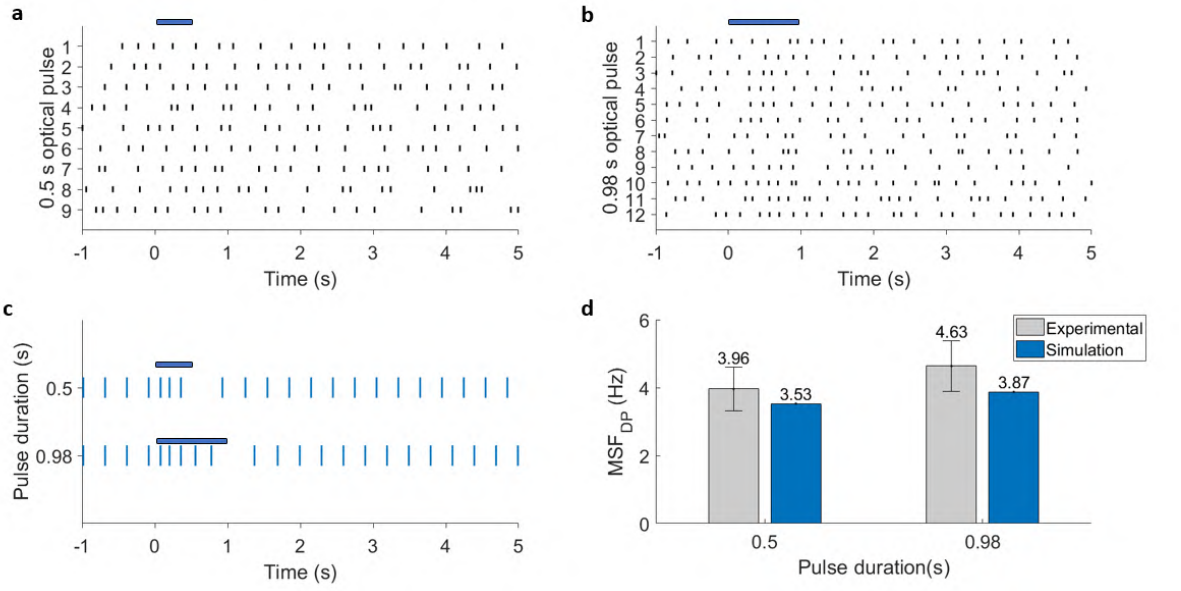

Figure 5.10: Measured and simulated optical response, for a pulse duration of both 0.5 s and 0.98 s. (a) measured optical response to 0.5 s pulse. (b) measured optical response to 0.98 s pulse. (c) simulated optical response for the two pulse durations. (d) bar graph representing the MSFs

5.5 Discussion

The goal was to create a model of the locus coeruleus that correctly represented the optogenetic responses. As starting point, the LC model derived by Carter et al. (2012) was used. However, their model was part of a network, where inter neuron currents were modeled with neurotransmitter dependent rates. These currents were simplified and replaced by a constant depolarizing current. This to asses the possibility of modeling the LC neuron with an independent (without a network) cell model, like the STN model in section 4.1. The amplitude of the depolarizing current was fitted, such that the same tonic firing measured in rat models was reached. As it turned out, it was impossible to model this behavior with the two compartment model. This due to the slower depolarization and increased threshold (see section 5.4.1). On the other hand, modeling of the correct behavior was possible with a single compartment model.

Modeling of the inter neuron currents with a constant depolarization, is an extreme simplification. AMPA responses are typically brief (~ 1 ms, (Petersen and Foustoukos, 2016)) and do not contain a rectangular shape, like the applied depolarizing current. Furthermore, the total current delivered by AMPA currents is variable as well. A possibility to improve the modeling of these, is to apply short depolarizing pulses. However, this quickly results in preset firing. To alter this, the pulse rate and amplitudes should be dependent on the membrane potential. Another possibility is to maintain the inter neuron currents as described in Carter et al. (2012) and couple them back from the axon to the soma compartment. Though, this should be accompanied with a certain delay, depending on firing rate and membrane potentials. Both alternatives, could resolve the issue of the two compartment model. Another possibility, is to alter the kinetics of the transmembrane current, such that it exhibits tonic firing without an external pulse. However, all these solutions are accompanied with an increase in complexity of the fitting paradigm increasing the risk of overfitting.

In this thesis, the fitting of the model was based on the data recorded in a single rat. Where the ability of generating an accurate pinch response served, as a small validation. Nevertheless, to address the generality of the model, it should be compared with unseen test data. First of all, the model should be fit to the measurements of multiple rats and not just one. Furthermore, the optical response should not be fit to a single pulse set, but to a mixed combination of pulses. Here, the overfitting is clearly visible. The model describes good the behavior of a 1.49 s pulse, on which it is fitted, however, fails to generate the correct behavior of the 0.98 s pulse. By including more measured data or better fitting algorithms, the risk of overfitting will be reduced and an increased generalization will be obtained. Moreover, it will be possible to fit the model with one of the aforementioned solutions.

Finally, only the simplified SFO model is used. Hence, no voltage or irradiance dependence is implemented. For low irradiances, this model could suffice, as Pan et al. (2014) denoted no biphasic current course for irradiances below 50 W/m^2. To take these dependences into account,

the advanced ChR2 model, described in section 3.3 could be used. However, its kinetics and irradiance dependence needs to be adjusted to match the slower dynamics but higher sensitivity of the ChR2(L132C-T159C) mutant. Consequently, the need for an advanced ChR2 model could be investigated.

5.6 Future work

In a future work, the issues mentioned in the discussion could be addressed. Currently, only a proof of concept is shown. However, an extensive validation is still required. Furthermore, the model needs to be fitted with more than data required from just one rat, to increase its generality. Also, the advanced ChR2 model kinetics need to be fitted to the dynamics of the correct mutant. Ideally, this is done with data of patch clamp recordings. Finally, the model could be compared with a network, that accurately models the inter neuron currents, with as goal the assessment of the usability and limitations of the generated model.

Conclusion

Under continuous light stimulation, channelrhodopsin-2 exhibits a biphasic current course, consisting of a transient peak followed by steady-state current. To model this behavior, at least a three transition state model is required. Several models have been proposed, which are summarized in figure 3.3. However, to account for both the fast off kinetics and multiple orders of magnitude higher recovery kinetics, a second light dependent step or a four state model, with two open and closed states, is needed. Ultimately, the four state model turned out to be superior, as it reproduces the bi-exponential, post-illumination current decay and agrees with the latest evidence for the existence of a second photocycle (see section 3.2). Consequently, the ChR2 model used throughout this thesis was a four state model derived by Williams et al. (2013), that incorporates both voltage and irradiance dependence. Although being very advanced, it does not cover all of ChR2's characteristics. Missing, is the pH dependence of the channel, which exhibits faster recovery and decreasing off kinetics, for a lower extracellular and intracellular pH, respectively. Furthermore, an empirically fitted rectification function is used, which results in physiological impossible conductances around the reversal potential. In this thesis, this is circumvented by using the rectification function derived by Grossman et al. (2011). Another possibility is to use extra transition states. However, this will result in a drastic increase of the models complexity.

With the use of the subthalamic nucleus model, derived by Otsuka et al. (2004), a comparative analysis between electrical and optical stimulation was performed. The investigated topics were the following: the effect of a continuous pulse on the firing rate, the strength-duration relationship for the generation of an action potential within ten milliseconds and the effect on the action potential morphology. Concerning the firing rate, a lot of similarities could be observed. Both stimulation sources caused a linear increase for low amplitudes and pulse durations up to 300 ms, and highly regular spiking behavior, with only small fluctuations at stimulus onset. Moreover, the same frequency range can be obtained with optical stimulations as with electrical up to 0.1 A/m^2. Nevertheless, for higher pulse durations, the firing rate decreases again with optical stimulation, while it remains constant for the electrical stimulus. Furthermore, with increasing irradiance, the frequency saturates, which is not observed with an electrical source. Also for the strength-duration relationship optical stimulation performed less. In order to fit the Hill-

Lapicque equation to the optical SD curve, the irradiance was replaced by the threshold average stimulating current. This enabled the direct comparison of the charge needed to excite. The rheobase of optical stimulation turned out to be almost twice (175.21%) the electrical rheobase (0.0124 A/m^2 vs. 0.0071 A/m^2). Moreover, the chronaxie is higher as well (9.61%). Therefore, there exists no pulse duration for which both stimulation sources are equally efficient. Concerning the effect on AP morphology, no major differences between the two stimulation sources could be observed, except at the hyperpolarization for high irradiances. From these results, electrical stimulation seems to be the superior stimulation source. However, to draw absolute conclusions, a model at the organ-level is required, that will alter the idealized, rectangular, electrical pulse. Furthermore, it must be kept in mind that the optical performance is opsin dependent.

Starting from the locus coeruleus model, derived by Carter et al. (2012), a network independent model was created, that correctly represents the optogenetic responses measured *in vivo* in rats. The short transient inter neuron currents where simplified with a continuous depolarizing current. The amplitude of this current was fitted, such that the same tonic firing measured in rat models was reached. As it turned out, it was impossible to model this behavior with the two compartment model as described in Carter et al. (2012). On the other hand, modeling of the correct behavior was possible with a single compartment model and a current amplitude of 0.39 A/m^2. As opsin model, the simple SFO model was adapted to the dynamics of a ChR2(L132C-T159C) mutant and its maximal conductance was fitted to measured 1.49 s optical pulse data. Good fits where obtained and even the pinch response could be accurately modeled. However, validation of the optical pulse against other pulse durations resulted in significantly different firing rates. Consequently, the model exhibits overfitting. This is not surprising. The model is only fitted against the data measured in one rat and to a single optical pulse. To improve its generalization, the training set should comprise multiple recordings. In future work, it will thus be necessary to improve the training set, conduct an extensive validation against unseen data and implement a version of the advanced ChR2 model, modified to match the dynamics of the mutant used in experimental testing.

Appendix A

Supplementary figures Chapter 4

Below, some supplementary figures of chapter 4 are depicted. These are used to facilitate the interpretation of the results and discussion, described in the aforementioned chapter. Included figures are: transmembrane currents of a single action potential under different stimulation conditions, transmembrane currents during a one second, 0.01 A/m^2 electrical pulse and transmembrane currents during one a second, 1000 W/m^2 optical pulse.

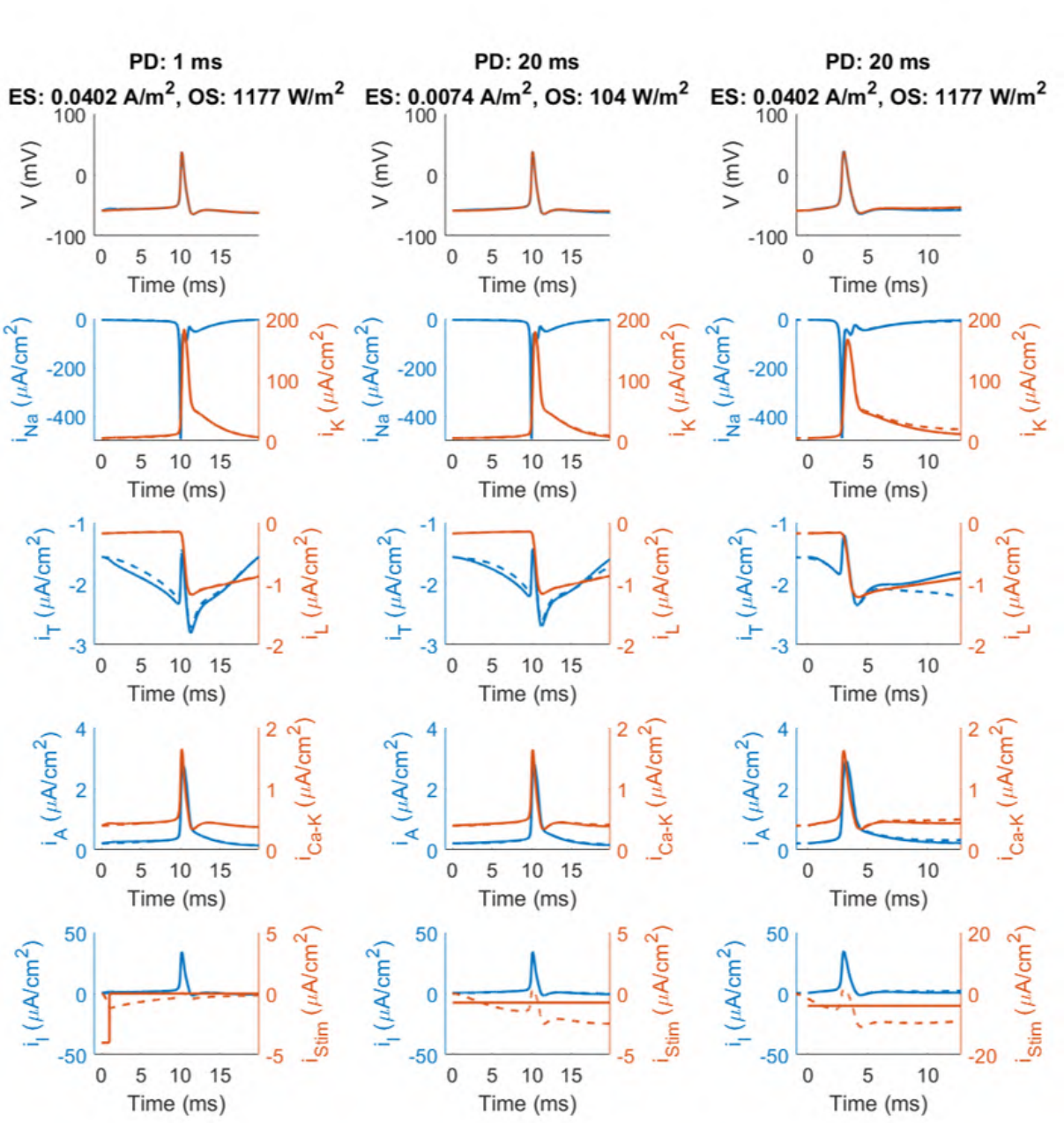

Figure A.1: Transmembrane currents of a single action potential under different stimulation conditions

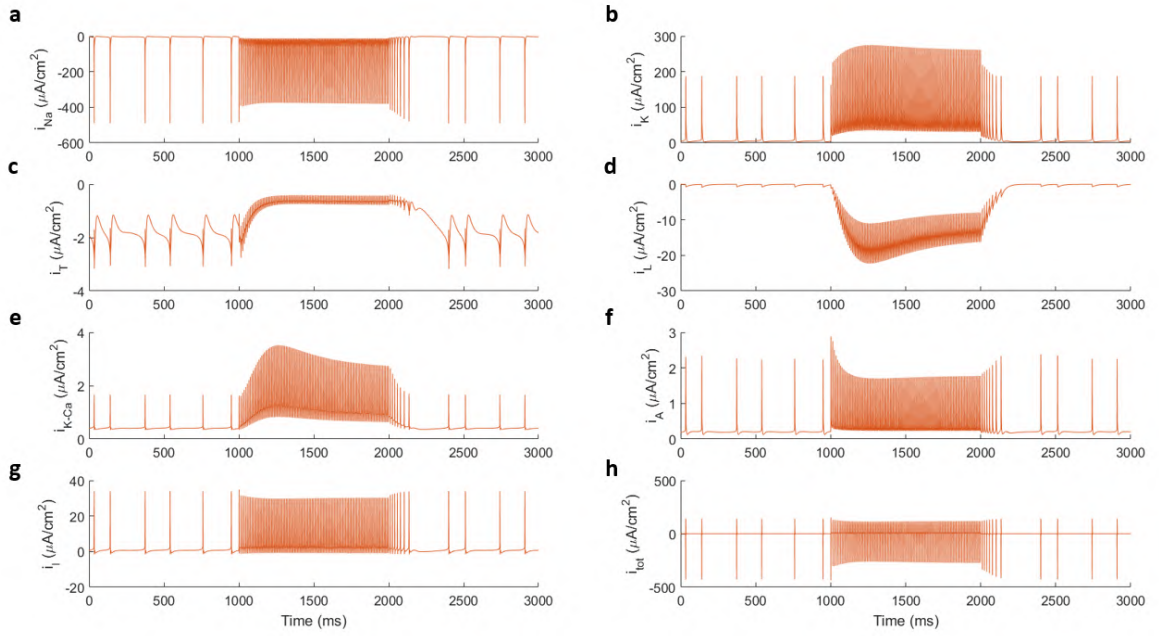

Figure A.2: Transmembrane currents during a one second, 0.01 A/m^2 electrical pulse

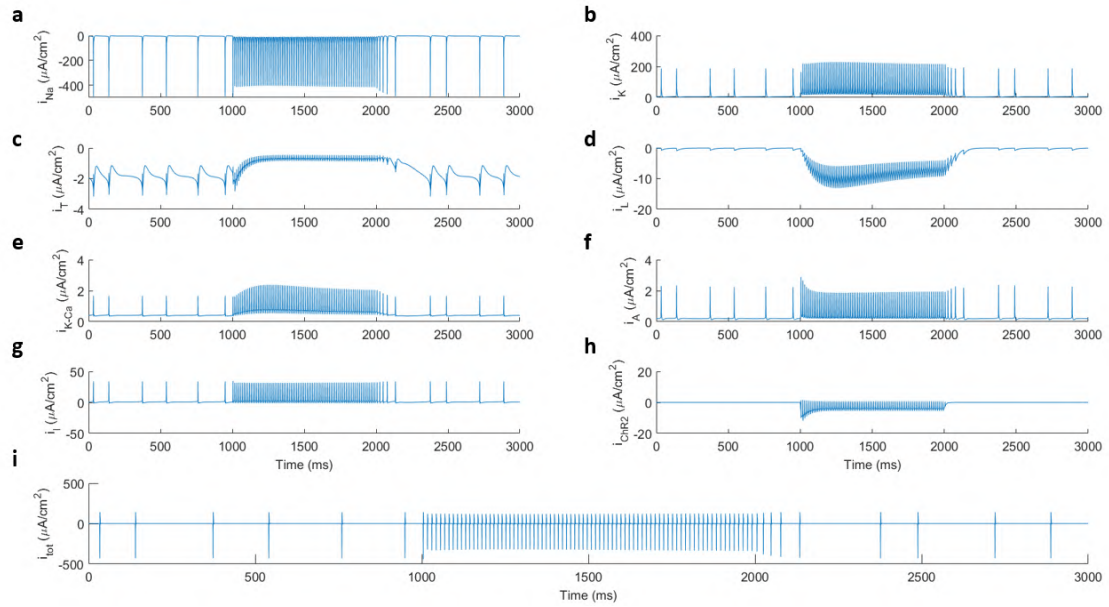

Figure A.3: Transmembrane currents during one a second, 1000 W/m^2 optical pulse

Appendix B

Supplementary figures Chapter 5

Below, some supplementary figures of chapter 5 are depicted. These are used to facilitate the interpretation of the results and discussion, described in the aforementioned chapter. Included figures are: comparison of the state occupancies of single and two compartment model for a fixed depolarizing current of 0.3 A/m^2, transmembrane currents evoked by a constant depolarizing current of 0.3 A/m^2 in the single compartment LC model and transmembrane currents evoked by a constant depolarizing current of 0.3 A/m^2 in the two compartment LC model

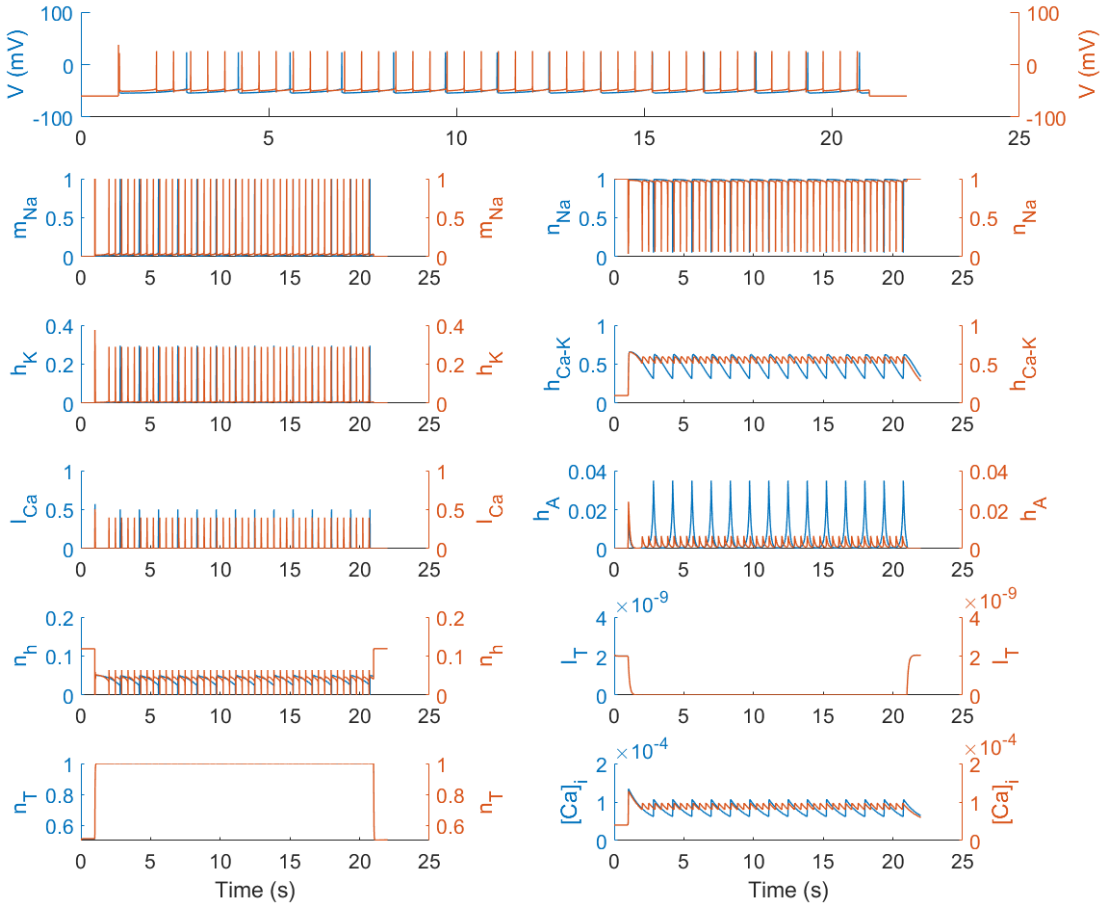

Figure B.1: Comparison of the state occupancies of single (orange) and two (blue) compartment model for a fixed depolarizing current of 0.3 A/m^2

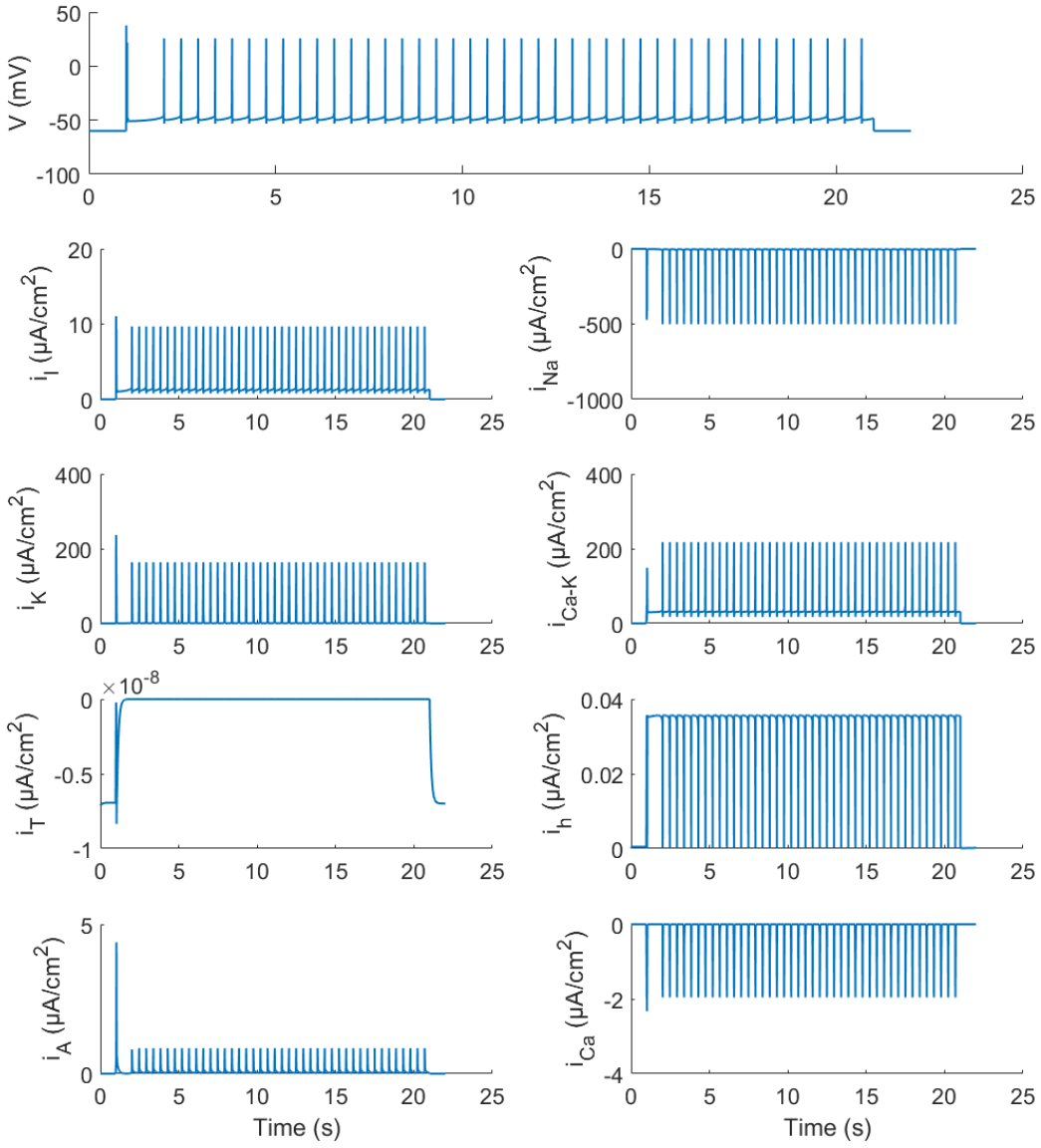

Figure B.2: Transmembrane currents evoked by a constant depolarizing current of 0.3 A/m^2 in the single compartment LC model

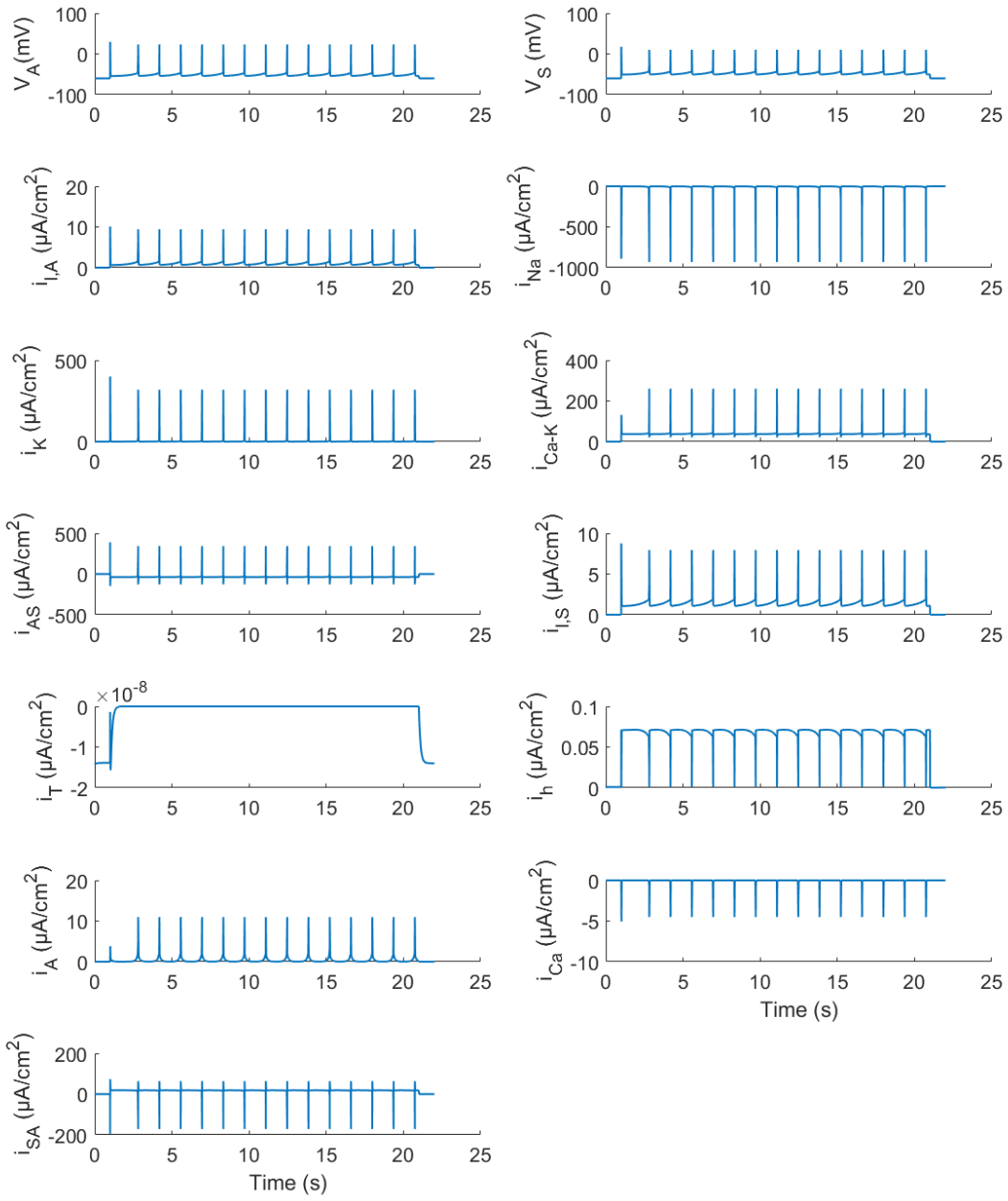

Figure B.3: Transmembrane currents evoked by a constant depolarizing current of 0.3 A/m^2 in the two compartment LC model

Bibliography

Abbott, L. F. and Dayan (2000). Model Neurons I: Neuroelectronics. In *Theoretical Neuroscience Computational and Mathematical Modeling of Neural Systems*, chapter 5, pages 156–198.

Abilez, O. J., Wong, J., Prakash, R., Deisseroth, K., Zarins, C. K., and Kuhl, E. (2011). Multiscale computational models for optogenetic control of cardiac function. *Biophysical Journal*, 101(6):1326–1334.

Alilain, W. J., Li, X., Horn, K. P., Dhingra, R., Dick, T. E., Herlitze, S., and Silver, J. (2008). Light-induced rescue of breathing after spinal cord injury. *The Journal of neuroscience : the official journal of the Society for Neuroscience*, 28(46):11862–70.

Aravanis, A. M., Wang, L. P., Zhang, F., Meltzer, L. A., Mogri, M. Z., Schneider, M. B., and Deisseroth, K. (2007). An optical neural interface: in vivo control of rodent motor cortex with integrated fiberoptic and optogenetic technology. *Journal of neural engineering*, 4(3).

Ardevol, A. and Hummer, G. (2018). Retinal isomerization and water-pore formation in channelrhodopsin-2. *Proceedings of the National Academy of Sciences*, 115(14):201700091.

Azimihashemi, N., Erbguth, K., Vogt, A., Riemensperger, T., Rauch, E., Woodmansee, D., Nagpal, J., Brauner, M., Sheves, M., Fiala, A., Kattner, L., Trauner, D., Hegemann, P., Gottschalk, A., and Liewald, J. F. (2014). Synthetic retinal analogues modify the spectral and kinetic characteristics of microbial rhodopsin optogenetic tools. *Nature Communications*, 5:1–12.

Bamann, C., Kirsch, T., Nagel, G., and Bamberg, E. (2008). Spectral Characteristics of the Photocycle of Channelrhodopsin-2 and Its Implication for Channel Function. *Journal of Molecular Biology*, 375(3):686–694.

Berridge, C. W. and Waterhouse, B. D. (2003). The locus coeruleus-noradrenergic system: modulation of behavioral state and state-dependent cognitive processes. *Brain research. Brain research reviews*, 42(1):33–84.

Boinagrov, D., Loudin, J., and Palanker, D. (2010). Strength-Duration Relationship for Extracellular Neural Stimulation: Numerical and Analytical Models. pages 2236–2248.

Bouret, S., Duvel, A., Onat, S., and Sara, S. J. (2003). Phasic activation of locus ceruleus neurons by the central nucleus of the amygdala. *The Journal of neuroscience : the official journal of the Society for Neuroscience*, 23(8):3491–7.

Boyle, P. M., Karathanos, T. V., and Trayanova, N. A. (2015). "Beauty is a light in the heart": The transformative potential of optogenetics for clinical applications in cardiovascular medicine. *Trends in Cardiovascular Medicine*, 25(2):73–81.

Boyle, P. M., Williams, J. C., Ambrosi, C. M., Entcheva, E., and Trayanova, N. A. (2013). A comprehensive multiscale framework for simulating optogenetics in the heart. *Nature Communications*, 4:1–9.

Bruegmann, T., Malan, D., Hesse, M., Beiert, T., Fuegemann, C. J., Fleischmann, B. K., and Sasse, P. (2010). Optogenetic control of heart muscle in vitro and in vivo. *Nature Methods*, 7(11):897–900.

Carter, M. E., Brill, J., Bonnavion, P., Huguenard, J. R., Huerta, R., and de Lecea, L. (2012). Mechanism for Hypocretin-mediated sleep-to-wake transitions. *Proceedings of the National Academy of Sciences*, 109(39):E2635–E2644.

Cavanaugh, J., Monoscor, I., and al, E. (2012). Optogenetic Inactivation Modifies Monkey Visuomotor Behavior. *Neuron*.

Chater, T. E., Henley, J. M., Brown, J. T., and Randall, A. D. (2010). Voltage- and temperature-dependent gating of heterologously expressed channelrhodopsin-2. *Journal of Neuroscience Methods*, 193(1):7–13.

Chen, Y., Xiong, M., and Zhang, S. C. (2015). Illuminating Parkinson's therapy with optogenetics. *Nature Biotechnology*, 33(2):149–150.

Claudia Pama, E. A., Colzato, L. S., and Hommel, B. (2013). Optogenetics as a neuromodulation tool in cognitive neuroscience. *Frontiers in Psychology*, 4(SEP):1–4.

Diester, I., Kaufmann, M. T., Mogri, M., and al, E. (2011). An optogenetic toolbox designed for primates. *Nature*, page 22.

Entcheva, E. and Williams, J. C. (2014). Channelrhodopsin2 Current During the Action Potential: "Optical AP Clamp" and Approximation. *Scientific Reports*, 4.

Feng, J. (2004). *Computational neuroscience : comprehensive approach*. Chapman & Hall/CRC.

Fozzard, H. A. and Schoenberg, M. (1972). Strength-duration curves in cardiac Purkinje fibres: effects of liminal length and charge distribution. *The Journal of physiology*, 226(3):593–618.

Gerits, A. and Vanduffel, W. (2013). Optogenetics in primates: A shining future? *Trends in Genetics*, 29(7):403–411.

Govorunova, E. G., Sineshchekov, O. A., Janz, R., Liu, X., and Spudich, J. L. (2015). Natural light-gated anion channels: A family of microbial rhodopsins for advanced optogenetics. 349(6248):647–651.

Gradmann, D., Berndt, A., Schneider, F., and Hegemann, P. (2011). Rectification of the channelrhodopsin early conductance. *Biophysical Journal*, 101(5):1057–1068.

Grossman, N., Nikolic, K., Toumazou, C., and Degenaar, P. (2011). Modeling study of the light stimulation of a neuron cell with channelrhodopsin-2 mutants. *IEEE Transactions on Biomedical Engineering*, 58(6):1742–1751.

Grossman, N., Simiaki, V., Martinet, C., Toumazou, C., Schultz, S. R., and Nikolic, K. (2013). The spatial pattern of light determines the kinetics and modulates backpropagation of optogenetic action potentials. *Journal of Computational Neuroscience*, 34(3):477–488.

Guru, A., Post, R. J., Ho, Y. Y., and Warden, M. R. (2015). Making sense of optogenetics. *International Journal of Neuropsychopharmacology*, 18(11):1–8.

Hahn, P. J. and McIntyre, C. C. (2010). Modeling shifts in the rate and pattern of subthalamopallidal network activity during deep brain stimulation. *Journal of computational neuroscience*, 28(3):425–41.

Häusser, M. (2014). Optogenetics: The age of light. *Nature Methods*, 11(10):1012–1014.

Hegemann, P., Ehlenbeck, S., and Gradmann, D. (2005). Multiple photocycles of channelrhodopsin. *Biophysical Journal*, 89(6):3911–3918.

Hegemann, P., Gärtner, W., and Uhl, R. (1991). All-trans retinal constitutes the functional chromophore in Chlamydomonas rhodopsin. *Biophysical Journal*, 60(6):1477–1489.

Hickey, L., Li, Y., Fyson, S. J., Watson, T. C., Perrins, R., Hewinson, J., Teschemacher, A. G., Furue, H., Lumb, B. M., and Pickering, A. E. (2014). Optoactivation of locus ceruleus neurons evokes bidirectional changes in thermal nociception in rats. *The Journal of neuroscience : the official journal of the Society for Neuroscience*, 34(12):4148–60.

Hodgkin, A. L. and Huxley, A. F. (1990). A quantitative description of membrane current and its application to conduction and excitation in nerve. *Bulletin of Mathematical Biology*, 52(1-2):25–71.

Izhikevitch, E. (2007). Dynamical Systems in Neuroscience. In *MIT Press*, chapter 2, pages 39–66.

Jazayeri, M., Lindbloom-Brown, Z., and Horwitz, G. D. (2012). Saccadic eye movements evoked by optogenetic activation of primate V1. page 10.

Kato, H. E., Zhang, F., Yizhar, O., Ramakrishnan, C., Nishizawa, T., Hirata, K., Ito, J., Aita, Y., Tsukazaki, T., Hayashi, S., Hegemann, P., Maturana, A. D., Ishitani, R., Deisseroth, K., and Nureki, O. (2012). Crystal structure of the channelrhodopsin light-gated cation channel. *Nature*, 482(7385):369–374.

Klapoetke, N. C., Murata, Y., Kim, S. S., Pulver, S. R., Birdsey-Benson, A., Cho, Y. K., Morimoto, T. K., Chuong, A. S., Carpenter, E. J., Tian, Z., Wang, J., Xie, Y., Yan, Z., Zhang, Y., Chow, B. Y., Surek, B., Melkonian, M., Jayaraman, V., Constantine-Paton, M., Wong, G. K. S., and Boyden, E. S. (2014). Independent optical excitation of distinct neural populations. *Nature Methods*, 11(3):338–346.

Kokaia, M., Andersson, M., and Ledri, M. (2013). An optogenetic approach in epilepsy. *Neuropharmacology*, 69:89–95.

Kravitz, A. V., Freeze, B. S., Parker, P. R. L., Kay, K., Myo, T., Deisseroth, K., and Kreitzer, A. C. (2010). Regulation of parkinsonian motor behaviors by optogenetic control of basal ganglia circuity. *Nature*, 466(7306):622–626.

Krook-Magnuson, E., Armstrong, C., Oijala, M., and Soltesz, I. (2013). On-demand optogenetic control of spontaneous seizures in temporal lobe epilepsy. *Nature communications*, 4:1376.

Lin, J. Y., Lin, M. Z., Steinbach, P., and Tsien, R. Y. (2009). Characterization of engineered channelrhodopsin variants with improved properties and kinetics. *Biophysical Journal*, 96(5):1803–1814.

Llewellyn, M. E., Thompson, K. R., Deisseroth, K., and Delp, S. L. (2010). Orderly recruitment of motor units under optical control in vivo. *Nature medicine*, 16(10):1161–5.

Marieb, E. N. and Hoenn, K. (2015). Fundamentals of the nervous system and nervous tissue. In *Human anatomy & Physiology*, chapter 11, pages 408–449. Pearson Education.

Matsuno-Yagi, A. and Mukohata, Y. (1977). Two possible roles of bacteriorhodopsin; a comparative study of strains of Halobacterium halobium differing in pigmentation. *Biochemical and biophysical research communications*, 78(1):237–43.

Mohanty, S. K., Group, P., Lakshminarayananan, V., Science, V., and Arbor, A. (2015). Optical Techniques in Optogenetics. 62(12):949–970.

Montgomery, K. L., Iyer, S. M., Christensen, A. J., Deisseroth, K., and Delp, S. L. (2016). Beyond the brain: Optogenetic control in the spinal cord and peripheral nervous system. *Science Translational Medicine*, 8(337).

Nagel, G., Ollig, D., Fuhrmann, M., Kateriya, S., Musti, A. M., Bamberg, E., and Hegemann, P. (2002). Channelrhodopsin-1: A light-gated proton channel in green algae. *Science*, 296(June):2395–2398.

Nagel, G., Szellas, T., Huhn, W., Kateriya, S., Adeishvili, N., Berthold, P., Ollig, D., Hegemann, P., and Bamberg, E. (2003). Channelrhodopsin-2, a directly light-gated cation-selective membrane channel. *Proceedings of the National Academy of Sciences*, 100(24):13940–13945.

Nikolic, K., Grossman, N., Grubb, M. S., Burrone, J., Toumazou, C., and Degenaar, P. (2009). Photocycles of channelrhodopsin-2. *Photochemistry and Photobiology*, 85(1):400–411.

Oesterhelt, D. and Stoeckenius, W. (1971). Rhodopsin-like protein from the purple membrane of Halobacterium halobium. *Nature: New biology*, 233(39):149–52.

Otsuka, T., Abe, T., Tsukagawa, T., and Song, W.-J. (2004). Conductance-based model of the voltage-dependent generation of a plateau potential in subthalamic neurons. *Journal of neurophysiology*, 92(1):255–264.

Packer, A. M., Roska, B., and Häuser, M. (2013). Targeting neurons and photons for optogenetics. *Nature Neuroscience*, 16(7):805–815.

Pan, Z. H., Ganjawala, T. H., Lu, Q., Ivanova, E., and Zhang, Z. (2014). ChR2 mutants at L132 and T159 with improved operational light sensitivity for vision restoration. *PLoS ONE*, 9(6).

Paz, J. T., Davidson, T. J., Frechette, E. S., Delord, B., Parada, I., Peng, K., Deisseroth, K., and Huguenard, J. R. (2013). Closed-loop optogenetic control of thalamus as a new tool to interrupt seizures after cortical injury Jeanne. *Nature neuroscience*, 16(1):64–70.

Petersen, C. and Foustoukos, G. (2016). *Cellular mechanisms of brain function*. EPFL press, 2017.

Pickard, W. F. (1976). Generalizations of the Goldman-Hodgkin-Katz equation. *Mathematical Biosciences*, 30(1-2):99–111.

Prigge, M., Schneider, F., Tsunoda, S. P., Shilyansky, C., Wietek, J., Deisseroth, K., and Hegemann, P. (2012). Color-tuned channelrhodopsins for multiwavelength optogenetics. *Journal of Biological Chemistry*, 287(38):31804–31812.

Purves, D., Augustine, G. J., Fitzpatrick, D., Hall, W. C., Lamantia, A.-S., Mcnamara, J. O., and Willians, S. M. (2004). *Neuroscience*, volume 3.

Raedt, R., Clinckers, R., Mollet, L., Vonck, K., El Tahry, R., Wyckhuys, T., De Herdt, V., Carrette, E., Wadman, W., Michotte, Y., Smolders, I., Boon, P., and Meurs, A. (2011). Increased hippocampal noradrenaline is a biomarker for efficacy of vagus nerve stimulation in a limbic seizure model. *Journal of Neurochemistry*, 117(3):461–469.

Reilly, J. P., Freeman, V. T., and Larkin, W. D. (1985). Sensory Effects of Transient Electrical Stimulation - Evaluation with a Neuroelectric Model. *IEEE Transactions on Biomedical Engineering*, BME-32(12):1001–1011.

Schneider, F., Grimm, C., and Hegemann, P. (2015). Biophysics of Channelrhodopsin. *Annual Review of Biophysics*, 44(1):167–186.

Stehfest, K. and Hegemann, P. (2010). Evolution of the channelrhodopsin photocycle model. *ChemPhysChem*, 11(6):1120–1126.

Talathi, S. S., Carney, P. R., and Khargonekar, P. P. (2011). Control of neural synchrony using channelrhodopsin-2: A computational study. *Journal of Computational Neuroscience*, 31(1):87–103.

Tao, Y., Huang, A. J. Y., Hashimotodani, Y., Kano, M., All, A. H., Tsutsui-kimura, I., Tanaka, K. F., Liu, X., and Mchugh, T. J. (2018). Near-infrared deep brain stimulation via upconversion nanoparticle mediated optogenetics. *Science*, 684(February):679–684.

Tarnaud, T., Joseph, W., Martens, L., and Tanghe, E. (2018). Dependence of excitability indices on membrane channel dynamics, myelin impedance, electrode location and stimulus waveforms in myelinated and unmyelinated fibre models. *Medical & biological engineering & computing*.

Tønnesen, J. and Kokaia, M. (2017). Epilepsy and optogenetics: can seizures be controlled by light? *Clinical Science*, 131(14):1605–1616.

Tønnesen, J., Sørensen, A. T., Deisseroth, K., Lundberg, C., and Kokaia, M. (2009). Optogenetic control of epileptiform activity. *Proceedings of the National Academy of Sciences of the United States of America*, 106(29):12162–7.

Van Dijck, G., Van Hulle, M. M., Heiney, S. A., Blazquez, P. M., Meng, H., Angelaki, D. E., Arenz, A., Margrie, T. W., Mostofi, A., Edgley, S., Bengtsson, F., Ekerot, C.-F., Jörntell, H., Dalley, J. W., and Holtzman, T. (2013). Probabilistic Identification of Cerebellar Cortical Neurones across Species. *PLoS ONE*, 8(3):e57669.

Wang, L., Li, D., Plested, C., Dawson, T., Teschemacher, A., and Paterson, D. (2006). Noradrenergic neuron-specific overexpression of nNOS in cardiac sympathetic nerves decreases neurotransmission. *Journal of Molecular and Cellular Cardiology*, 41(2):364–370.

Williams, J. C. and Denison, T. (2013). From optogenetic technologies to neuromodulation therapies. *Science Translational Medicine*, 5(177):1–5.

Williams, J. C. and Entcheva, E. (2015). Optogenetic versus electrical stimulation of human cardiomyocytes: Modeling insights. *Biophysical Journal*, 108(8):1934–1945.

Williams, J. C., Xu, J., Lu, Z., Klimas, A., Chen, X., Ambrosi, C. M., Cohen, I. S., and Entcheva, E. (2013). Computational Optogenetics: Empirically-Derived Voltage- and Light-Sensitive Channelrhodopsin-2 Model. *PLoS Computational Biology*, 9(9):17–19.

Wong, J., Abilez, O. J., and Kuhl, E. (2012). Computational optogenetics: A novel continuum framework for the photoelectrochemistry of living systems. *Journal of the Mechanics and Physics of Solids*, 60(6):1158–1178.

Wykes, R. C., Kullmann, D. M., Pavlov, I., and Magloire, V. (2016). Optogenetic approaches to treat epilepsy. *Journal of Neuroscience Methods*, 260:215–220.

Yizhar, O., Fenno, L. E., Davidson, T. J., Mogri, M., and Deisseroth, K. (2011). Optogenetics in Neural Systems. *Neuron*, 71(1):9–34.

Yoon, H. H., Min, J., Hwang, E., Lee, C. J., Suh, J. K. F., Hwang, O., and Jeon, S. R. (2016). Optogenetic Inhibition of the Subthalamic Nucleus Reduces Levodopa-Induced Dyskinesias in a Rat Model of Parkinson's Disease. *Stereotactic and Functional Neurosurgery*, 94(1):41–53.

Yoon, H. H., Park, J. H., Kim, Y. H., Min, J., Hwang, E., Lee, C. J., Francis Suh, J.-K., Hwang, O., and Jeon, S. R. (2014). Optogenetic Inactivation of the Subthalamic Nucleus Improves Forelimb Akinesia in a Rat Model of Parkinson Disease. *Neurosurgery*, 74(5):533–541.

Zhao, M., Alleva, R., Ma, H., Daniel, A. G., and Schwartz, T. H. (2015). Optogenetic tools for modulating and probing the epileptic network. *Epilepsy Research*, 116:15–26.

Computational models of optogenetic neurostimulation

Ruben Schoeters

Supervisors: Prof. dr. ir. Emmeric Tanghe, Prof. dr. Robrecht Raedt
Counsellor: Thomas Tarnaud

Master's dissertation submitted in order to obtain the academic degree of
Master of Science in Biomedical Engineering

Department of Information Technology
Chair: Prof. dr. ir. Bart Dhoedt

Animalarium,Vakgroep Inwendige ziekten
Chair: Prof. dr. Guy Joos

Faculty of Engineering and Architecture
Academic year 2017-2018

GHENT
UNIVERSITY